FT-IR and Quantum Cascade Laser Spectroscopy Towards a Hand-Held Trace Gas Sensor for Benzene, Toluene, and Xylenes (BTX)

A Thesis

Presented to

The Academic Faculty

by

Christina Young

In Partial Fulfillment

of the Requirements for the Degree

Doctor of Philosophy in Chemistry

Georgia Institute of Technology

December, 2009

FT-IR and Quantum Cascade Laser Spectroscopy Towards a

Hand-Held Trace Gas Sensor for Benzene, Toluene, and Xylenes (BTX)

Approved by:

Dr. Boris Mizaikoff, Advisor
School of Chemistry and Biochemistry
Georgia Institute of Technology

Dr. Jiri Janata
School of Chemistry and Biochemistry
Georgia Institute of Technology

Dr. Oliver Brand
School of Electrical and Computer Engineering
Georgia Institute of Technology

Dr. Thomas Orlando
School of Chemistry and Biochemistry
Georgia Institute of Technology

Dr. Facundo Fernandez
School of Chemistry and Biochemistry
Georgia Institute of Technology

Dr. Mark Disko
Corporate Strategic Research
ExxonMobil Research and Engineering Company

Date Approved: October 27, 2009

This thesis is dedicated to my parents who taught me the value of an education

ACKNOWLEDGEMENTS

First, I would like to thank my research advisor, Dr. Boris Mizaikoff for his optimism and the endless opportunities he has provided. I have had the opportunity to work with many people in graduate school, from a national laboratory to industries to universities because of your collaborative efforts. Thank you!

I am grateful for the critical feedback and input provided by my thesis committee.

The research within this thesis would not have been possible without assistance from our collaborators: Daylight Solutions for providing an external cavity tunable QCL, Adtech Optics, particularly Dr. Xiaojun Wang and Dr. Jenyu Fan, for providing BHa507 for cavity length experiments. Prof. Dr. Claire Gmachl, a terrific inspiration and advisor, who encouraged and supported my education and development as a scientist. I thank her for providing the opportunity to study and work with her group as the experience has greatly enriched my journey. I am also very grateful to the members Prof. Gmachl's group who provided very fruitful discussions and feedback including (in no particular order): Richard Cendejas, Dr. Scott S. Howard, Wendy Sanchez-Vaynshteyn, Dr. Anthony J. Hoffman, Dr. Kale J. Franz, Yu Yao, Dr. Fatima Toor, Matthew Escarra, Ekua Bentil, Qiang Liu and Dr. Afusat Dirisu.

A special thanks is also extended to Dr. Claire Gmachl, Dr. Kale Franz, and Dr. Seong-Soo Kim for their critical contribution to my understanding of quantum mechanics. Their teaching and patience means a lot to me.

ExxonMobil Research and Engineering Company (EMRE) and ExxonMobil Biomedical Sciences, Inc. are acknowledged for funding and support. Special thanks are extended to Dr. Andrew Riley, Dr. Mark. M. Disko, Cornelius Brons, Dr. John Fried, Dr. James Brown, Dr. John Szobota, and Curtis Byler from ExxonMobil Research and Engineering Company. I would also like to thank Dr. John Martin (ExxonMobil Industrial Hygiene), Paul Russo, Eileen Pearlman, Justin Davenport, Eduardo Shaw, Rob Tutt, Jeffery Butler, Michael Verra, Larry Daniel, Tammy Leach, and Steve McGovern who were instrumental in preparing for and executing the field measurement campaign.

Prof. Dr. Karl Booksh and Bryon Herbert from the University of Delaware are also thanked for their assistance with the chemometrics and multivariate data analysis presented in Chapter 2.

I'm also very appreciative to my friends and colleagues in the field of analytical chemistry their influence and camaraderie including: Dr. Jonathan Scaffidi, Dr. Marion Lawrence Snyder, Dr. Christina Hampton, Yuliya Luzinova, Dr. Justyna Wiedemair, Rongwei Zhang, Dr. Nicola Menegazzo, Dr. Christy Charlton, Dr. Seong-Soo Kim, and Arti Navare.

I am often asked why I decided to study chemistry. My high school chemistry teacher, Mrs. Rosalyn Barton, was my inspiration. Beyond providing an incredibly strong foundation in chemistry, she had faith in me, taught me how to solve problems and overcome challenges, and went above and beyond the call of duty for any public school teacher.

It is with deep gratitude that I thank my chemistry professor mentors at the University of South Carolina (USC) - I could not have asked for a better springboard for my future. I would like to thank Dr. Scott Goode, my academic advisor, for years of direction and guidance; Dr. S. Michael Angel, my undergraduate research advisor for the first introduction to scientific research and for being an outstanding mentor and advisor; Dr. Stephen Morgan for teaching my first analytical chemistry classes and for his support and encouragement over the years. I am proud to be an alumnus of USC and for the opportunity to learn and grow with the help of such phenomenal faculty.

This work would not have been possible without the love and support from the many friends and family members who have been there for me. Thank you to Mom and Dad Palmer for always showing interest in my studies and always supporting me. To my best friend Lynn, I can't thank you enough for always standing by me, your support, and your love. To my parents, who have always supported and loved me unconditionally, encouraged me and always wanted the best for me.

Lastly to Doug. It is with deep gratitude that I thank you for always standing by me, for your patience and understanding of the late nights at school and months of working and studying across the country, and your unconditional love and support. Thank you and I love you.

TABLE OF CONTENTS

LIST OF TABLES

LIST OF FIGURES

LIST OF ABBREVIATIONS

BTXs	Benzene, Toluene, Xylene(s)
BTEX	Benzene, Toluene, Ethylbenzene, Xylene
CRD	Cavity Ring-down
CW	Continuous Wave
DFB	Distributed Feedback
DFG	Difference Frequency Generation
EC	External Cavity
EPA	Environmental Protection Agency
FID	Flame Ionization Detector
FoM	Figure of Merit
FP	Fabry-Perot
FT-IR	Fourier Transform Infrared
GC	Gas Chromatography
HWG	Hollow Waveguide
ICOS	Integrated Cavity Output Spectroscopy
LIDAR	Light Detection and Ranging
LOD	Limit of Detection
MS	Mass Spectroscopy
MBE	Molecular Beam Epitaxy
MCT	Mercury-Cadmium-Telluride
MIR	Mid-Infrared
NIOSHA	National Institute for Occupational Health and Safety Administration

OAPM	Off-Axis Parabolic Mirror
OPO	Optical Parametric Oscillator
OSHA	Occupational Health and Safety Administration
PAS	Photoacoustic Spectroscopy
PBG	Photonic Bandgap
PDMS	Polydimethylsiloxane
PID	Photoionization Detector
PLS	Partial Least Squares
ppb	Parts-Per-Billion
ppm	Parts-Per-Million
ppt	Part-Per-Trillion
QCL	Quantum Cascade Laser
QEPAS	Quartz Enhanced Photoacoustic Spectroscopy
SPME	Solid Phase Microextraction
TIR	Total Internal Reflection
TD	Thermal Desorption
UV	Ultraviolet
Vis	Visible
VOC	Volatile Organic Compound

SUMMARY

The work described in this thesis focuses on FT-IR and quantum cascade laser (QCL) based studies towards the development of compact and portable trace gas sensor for benzene, toluene, and xylenes (BTX).

In the first part of this thesis, FT-IR broadband radiation was used to probe the mid-infrared fingerprint region for quantitatively detecting trace gas levels of BTX. Using direct absorption through a hollow waveguide, parts-per-million (ppm) detection limits for BTX with a response time of 39 seconds was demonstrated. Univariate calibration provided limits of detection (3σ) for benzene, toluene, and meta-xylene at 5, 17, and 11 ppm, respectively. Multivariate calibration using partial least squares regression algorithms were used to simulate real-world conditions with multiple analytes present within a complex sample. A calibration model was built with 110 training set standards enabled by using a customized gas mixing system.

To lower detection limits toward environmentally more relevant concentrations, a preconcentration/thermal desorption (TD) step was added to the FT-IR HWG trace gas sensor enabling parts-per-billion detection of BTX. A univariate calibration was established in the laboratory with certified gas standards over a dynamic range of 1000 – 100 ppb for benzene, toluene, and the xylenes. The sensor was then taken to an industrial site during a field measurement campaign for the quantitative determination of BTX in field air samples. The laboratory calibration was used to predict unknown concentrations

which were in close agreement with industrial hygiene standard techniques, and industrial prototype analyzers, that were simultaneously operated in the field environment. Independent validation of the obtained results was performed via GC-FID analysis. Further optimization of the experimental parameters finally resulted in the reproducible detection of 5 ppb benzene with the developed TD-FT-IR-HWG sensing device.

The second part of this thesis was focused on quantum cascade lasers and their role in trace gas sensors in an effort to miniaturize future IR gas sensing platforms. Particlar efforts were dedicated on a novel principle for consistent and deliberate QCL emission wavelength selection by varying the QCL cavity length. These studies experimentally confirmed that using this straight-forward post-processing technique, emission wavelength tuning across a range of one hundred wavenumbers range may be achieved. This tuning range was experimentally demonstrated for a QCL emitting across an entire absorption feature of carbon dioxide by tailoring the length of the cavity. Additionally, using an external cavity (EC) – QCL combined with a HWG gas sensor module for the first time enabled the quantitative and simultaneous determination of ethyl chloride, trichloromethane, and dichloromethane within exponential dilution experiments at ppb limits of detection. Multianalyte detection was demonstrated utilizing partial least squares regression for quantitative discrimination of individual constituents within a mixture, yet applying a single broadly tunable QCL light source.

Finally, an outlook is provided for continuing research in this field toward further miniaturization of the sensing platform established within this thesis e.g. by evaluating

the feasibility of coiling HWGs. Furthermore, current limitations for obtaining QCLs lasing at longer wavelengths – as required for BTX analysis - are discussed, as well as the potential future of QCL based trace gas sensors for BTX.

CHAPTER 1

INTRODUCTION

1.1 Thesis Objective

The objective of this thesis revolves around one central goal – to engineer compact gas sensors for benzene, toluene, and xylenes (BTX) at trace level sensitivity (parts-per-billion (ppb) or below), with short response times (preferably real-time or on the order of a few seconds), and molecular selectivity (discrimination against other hydrocarbons commonly found in environmental air). This objective was pursued based on four distinct approaches:

(i) direct parts-per-million (ppm) sensing of BTX using Fourier-Transform infrared (FT-IR) hollow waveguide (HWG) gas sensors, (ii) ppb sensing of BTX using FT-IR HWG gas sensors using preconcentration as a sample pre-treatment step, (iii) a novel method to tune the quantum cascade laser (QCL) emission wavelength via cavity length modification for precise overlap with analyte absorptions, and (iv) external cavity coupled quantum cascade laser (EC-QCL) gas sensors for multianalyte trace gas sensing; all of which will be summarized as original contributions below.

1.2 Original Contributions and Thesis Overview

The first original contribution to this thesis focuses on the simultaneous detection of BTX at ppm levels using FT-IR HWG trace gas sensors (Chapter 2). This project demonstrates the first application of a FT-IR HWG gas sensing system coupled with a custom gas mixer for establishing both univariate and multivariate calibration models enabling direct quantification of gas phase BTX. Critical figures of merit achieved during this study are direct sensing of BTX with a 39 second response time, limited only by intrinsic FT-IR spectra acquisition parameters such as spectral averaging and resolution.

To lower detection limits toward environmentally relevant concentrations, i.e. ppb, a preconcentration step followed by thermal desorption) was added to the FT-IR HWG device resulting in a dynamic range of 1000 to 100 ppb BTX in the gas phase. After a laboratory calibration was established using known gas standards, this sensor was taken to an industrial location for field testing (collaboration with ExxonMobil Research and Engineering Company, Annandale, NJ) for the first time demonstrating ppb detection of BTX in real-world air samples with a FT-IR HWG gas sensor. It is important to note that the results of these field measurements were comparable with off-the-shelf BTX gas sensors presently used in industrial hygiene applications, as well as industrial prototypes and the validation method. Validation experiments were performed with gas chromatography and flame ionization detection (GC-FID), which were independently measured and verified by ExxonMobil Biomedical Sciences Inc., Annandale, NJ. Also of

importance is that despite rapid response time from the FT-IR (39 seconds), the sample preconcentration step becomes the limiting factor in overall response time, especially as very low (5 ppb benzene) detection limits are pursued.

Within the thesis objectives was the development of fundamentals for creating *hand-held* BTX trace gas sensors. While FT-IR HWG gas sensors are portable and capable of being transported into the field, the platform itself remains at a bench-top sized footprint due to the dimensions of the FT-IR spectrometer. The advent of quantum cascade lasers in 1994 by Faist, et. al.[1] opened up a whole new world in mid-infrared spectroscopy by offering a light source with a miniaturized footprint with the intrinsic benefit of enhanced spectral density, which – if efficiently overlapped with analyte absorption peak(s) - provides both improved sensitivity and selectivity. Thus, it is evident that the next-generation of mid-infrared based trace gas sensor technology would entail QCL technology.

Consequently, the third original contribution within this thesis focuses on improved selectivity with QCL based chemical sensors developing a novel method to tune the emission wavelength of the QCL to the desired frequency by cavity length modification. This contribution is particularly important because, as – in contrast to FT-IR based sensors with the intrinsic benefit of broadband radiation enabling multi-constituent analysis - QCLs must be tuned to overlap the desired absorption feature(s) for selective detection. Since current methods predominantly rely on temperature or current tuning by only a few wavenumbers, or the combination of the laser with external cavities, an intrinsic technology for reliably and deliberately tailoring the QCL emission is extremely

useful for effective usage of QCLs in chemical sensors. This work presents a straight-forward post-processing method to tune the QCL emission wavelength by changing the cavity length resulting in a 118 cm^{-1} tuning range, which is broad enough for tuning across an entire absorption feature of carbon dioxide, which was the exemplary analyte for this study. It is anticipated that this method could be applied to tune across the fingerprint region of the mid-infrared spectrum for BTX analysis as well, once QCLs with appropriate emission wavelengths become available.

The final original contribution to this thesis discusses the first combination and characterization of an EC-QCL with a HWG gas sensing module to measure multiple analytes with one broadly tunable laser light source. This work demonstrates (i) ppb level detection of individual analytes by using exponential dilution, and (ii) the first EC-QCL spectrum of three analytes simultaneously determined in mixture utilizing a partial-least squares regression model for quantitatively discriminating each component despite considerable peak overlap.

As previously mentioned, theoretically it has been shown that QCLs can emit anywhere within the mid-infrared spectral regime, however, due to factors discussed later in this thesis, emission at longer wavelengths (i.e. the fingerprint region relevant to BTX sensing) has not yet been experimentally demonstrated. Nonetheless, the present thesis lays the foundation for the evolution toward hand-held QCL-based trace gas sensors for BTX in the near future pending the availability of the appropriate emission wavelength.

1.3 Thesis Motivation

1.3.1 Is There a Need for Trace Gas Sensors for BTX?

Benzene, toluene, and ortho,meta,para-xylenes are monocyclic aromatic hydrocarbons with molecular structures illustrated in Figure 1-1:

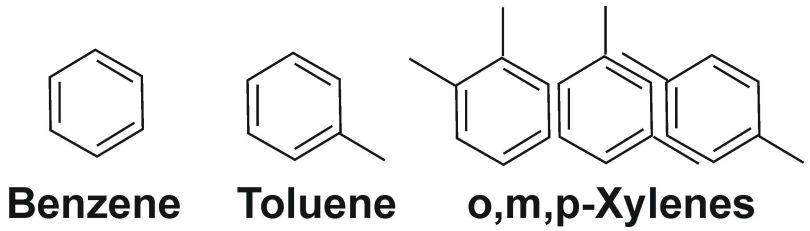

Figure 1-1: Molecular structures of benzene, toluene, and ortho,meta,para-xylenes, respectively.

These organic compounds are important to be accurately detect in the environment in the context of applications such as process monitoring[2], environmental/workplace detection[3-6], quality assurance/control in commercial processes[7], and bioremediation efficiency[8]. Currently, there is no low-cost trace gas sensor commercially available that is capable of real-time, sensitive (on the order of ppb to ppt concentration levels), and selective detection/discrimination of these organic compounds with a miniaturized platform, i.e. a hand-held or wearable device.

Additionally, from an industrial hygiene perspective the Occupational Safety and Health (OSHA) administration (standard 29 CFR 1910.1000) sets the permissible exposure limits (8 hour time weighted average) of benzene, toluene, and xylenes at 1, 200, and 100 ppm, respectively for occupational workers. Furthermore, OSHA sets a short term

exposure limit (15 minutes) for benzene at 5 ppm, and the National Institute for Occupational Safety and Health at 0.1 ppm (100 ppb). Thus, there is a significant need to quantify gas phase BTX in real-time and dynamically rather than via a (cumulative) dosimetry approach with discrimination against other structurally and chemically similar constituents (selectivity) to avoid false positives, as well as the demanded sensitivity to comply with government regulations. Hence, it is apparent that the ideal instrument would measure all relevant BTX components at < 10 ppb (well below exposure limits) in real-time, or at least within a period of less than a minute. Furthermore, the ideal trace gas sensor should be capable of not only spot checking, i.e. BTX detection in grab samples, but also over 8 hours or longer time periods (e.g. a shift) where a worker could be exposed to a concentration spike not necessarily measurable by cumulative exposure analysis.

1.3.2 Current Technologies for BTX Trace Gas Sensing

The state-of-the-art for gas phase detection of BTX typically utilizes GC as the separation/selectivity step combined with a detector such as e.g. photoionization (GC-PID)[9], flame ionization (GC-FID)[10-14], or mass spectroscopy (GC-MS)[12, 15-19], usually in combination with some type of preconcentration (typically adsorbing over PDMS and/or Carboxen). GC-PID is advantageous for simultaneous measurement of BTX; however, the selectivity may suffer from alkane interference[20], frequently resulting in an overestimation of the true BTX concentration measured in environmental air samples. GC-FID may provide volatile organic compounds (VOC) analysis with a large linear dynamic range and cost efficiency, but without compound confirmation. To partly

overcome this drawback, separation may be performed simultaneously on two columns with different polarities. On the other hand, GC-MS provides high sensitivity, selectivity, and accuracy with the potential toward portable device footprints (roving or man)[21], as demonstrated by one study which measured low ppb BTX in urban outdoor environments over space and time gradients[22]. However, GC-MS cannot provide real-time measurements, is not cost-effective, and does not yet exhibit potential for a hand-held device footprint. Furthermore, to date all three methods (GC-PID, GC-FID, and GC-MS) have difficulties differentiating between and quantifying meta- and para-xylenes.

In addition to these current state-of-the-art methods, other more experimental methods have been developed to measure ppb levels of BTX. One study developed a miniaturized GC system in combination with a solid-state metal oxide semiconductor (MOX) detector to measure a few ppb up to several tens of ppb BTX in indoor air [23, 24]. Another work differentiated 20 ppb benzene in a BTX gas mixture via GC-ion mobility spectroscopy (IMS)[25]. However, these techniques still rely on GC which is limited by relatively long response times. Microfluidic devices, using mesoporous silicate designed for gas phase BTX sensing[26, 27], have also been used to measure 100 ppb benzene discriminated in a mixture with toluene[27]; however it has not yet been shown that low ppb of benzene, toluene, and xylenes can be measured simultaneously and within mixtures of all three constituents. Moreover, a method known as membrane introduction mass spectroscopy (MIMS) was utilized to measure benzene and toluene at LODs of 600 and 200 ppt, respectively without relying on GC[28]. However, this particular method suffers from

overlapping peaks and the inability to quantitatively discriminate individual xylene isomer.

1.3.3 Current Technologies for BTX Trace Gas Sensing: Optical Spectroscopy

Optical spectroscopy methods have also gained momentum for the detection of gas phase BTX. Kim and coworkers used a UV differential optical absorption spectroscopy (DOAS)[29] method to measure low ppb BTX in environmental air simultaneously comparing with an online GC system[30, 31]. Furthermore, DOAS was combined with FT-IR spectroscopy using a 500 m open path to measure detection limits of 0.9 ppb for benzene, toluene and xylene (BTX) with an accuracy of approximately 30%[32]. Although DOAS systems are capable of continuous and sensitive BTX detection, the sensitivity may suffer at low-visibility conditions, and the selectivity may suffer from interference effects due to the presence of oxygen, ozone, and several hydrocarbons with similar spectra[33]. Direct spectrophotometry demonstrated ppb level detection of BTX using PDMS as a sorbent[34].

1.3.4 Why Mid-Infrared Spectroscopy for BTX Trace Gas Sensing?

As an alternative to the aforementioned analytical techniques, mid-infrared spectroscopy has gained momentum in BTX trace gas sensing research, as direct probing of the analyte is offered allowing near real-time response times (on the order of a few seconds), limited only by parameters such as the spectral resolution and averaging of sufficient spectra for the required signal-to-noise ratio. In particular, FT-IR spectroscopy has been demonstrated as a practicable method for the simultaneous detection of aromatic

hydrocarbons in the gas phase [35, 36]. The attractiveness of FT-IR-based devices for BTX detection include the inherent selectivity provided by the fingerprint region of the mid-infrared spectrum at approx. 1200 - 400 cm^{-1} [37].

1.4 Mid-IR Spectroscopy Fundamentals

This section presents fundamentals on mid-infrared (MIR) spectroscopy as the background required to understand the research presented in the following chapters.

1.4.1 Absorption Spectroscopy

From a chemical sensing perspective, BTX selectively absorbs IR radiation at specific wavelengths resulting in a loss of transmission through a gas cell or an open path, as illustrated in Figure 1-2.

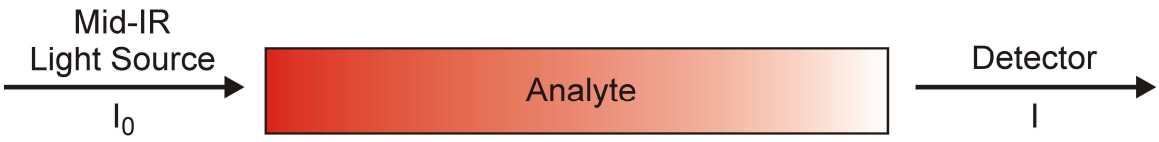

Figure 1-2: Schematic of analyte absorption either in open path or within a gas cell.

This loss is compared to a reference spectrum, thereby yielding qualitative and quantitative information on specific analytes in the gas phase at trace levels, if a sufficiently long absorption path length is provided. In brief, in order for absorption in the IR to occur, the analyte must provide vibrational or rotational energy levels resonant with the incident photon energy, and must exhibit a permanent change of the dipole moment. The mathematical expression for absorption is given in Equation 1-1:

$$A = -\log(T) = \log_{10}\left(\frac{I_0}{I}\right) \qquad \text{(Eqn. 1-1)}$$

where T is the transmission, I_0 is the intensity of the incident radiation, and I is the intensity of radiation after interaction with the analyte.

Concentration as a function of loss in light intensity is described by the Beer-Lambert law, as given by Equation 1-2:

$$A = \varepsilon l c \qquad \text{(Eqn. 1-2)}$$

where A is the absorbance, ε is the molar absorptivity (a constant inherent to the analyte), l is pathlength (assumed to be a constant describing an invariable absorption path length e.g. within a HWG), and c is the concentration. Thus, this law implies that there is a linear relationship between absorbance and concentration, which provides the basis for calibrations that can be used to predict unknown analyte concentrations in real-world air matrices. Non-linear deviations from this law are typically resulting from e.g. analyte interactions or reactions, detector saturation, etc.

1.4.2 Hollow Waveguides

From Equation 1-2 it is apparent that analyte absorption is also directly proportional to the absorption pathlength, e.g. the actual distance from the light source to the detector in an open path scenario. The absorption path length may be enhance using e.g. a reflectively coated gas cell featuring multiple internal reflections (e.g. hollow waveguides) or a gas cell folding the optical path (e.g. multipass gas cells), which may

significantly enhance the achievable sensitivity. A comprehensive review of gas cells used in trace gas sensors is provided in Chapter 4 of this thesis.

The gas cells utilized in the research presented here are based on hollow waveguide structures[38]. Hollow waveguides efficiently propagate infrared radiation within their hollow core, while simultaneously serving as a small volume gas cell. This concept is especially useful for mid-infrared absorption spectroscopy, where hollow waveguides facilitate intimate contact of photons with analyte molecules within the compact hollow core. Conventional hollow waveguides are internally coated with a silver (Ag) layer, and a thin protective layer of silver iodide (AgI) to propagate radiation via metallic reflection inside the hollow core from the light source to a detector[39]. Hence, these multiple reflections increase the effective optical pathlength, thereby improving the signal-to-noise ratio within a sample volume on the order of only a few milliliters.

1.4.3 MIR Fingerprint Region

In brief, absorption occurs if mid-infrared radiation interacts with analytes at the condition of resonance and if a permanent change of the dipole moment is occurring, thus resulting in a loss of transmitted radiation through the hollow waveguide. In the MIR, analytes absorb radiation at molecularly specific frequencies within the mid-infrared spectral regime, which is considered from 4000 to 400 cm^{-1}. Probing of molecule-specific fundamental rotational and vibrational transitions provides strong absorption features conducive to sensitive and selective sensing e.g. in the gas phase. The “fingerprint region” (1200 - 400 cm^{-1}) of the IR spectrum comprises absorption features of particular

molecular selectivity, due to a mix of fundamental and combination modes creating highly specific absorption patterns. Specific to the studies in this thesis, benzene, toluene and o,m,p-xylenes (BTX) provide unique absorption patterns with the most prominent absorptions located at 673, 727, 740, 767, and 795 cm^{-1}, respectively. The BTX-relevant spectral regime within the electromagnetic spectrum is described in Figure 1-3.

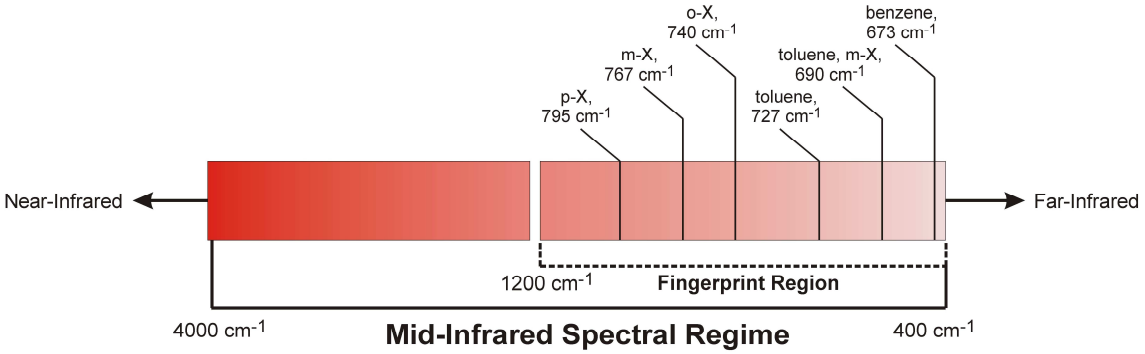

Figure 1-3: Mid-infrared spectral regime featuring the fingerprint region (1200 – 400 cm^{-1}) with relevant BTX absorption signatures ranging from 795 cm^{-1} to 673 cm^{-1}. o-x, m-x, and p-x denote ortho, meta, and para-xylenes, respectively.

The BTX spectral features within the fingerprint region exhibit sharper and more selective peaks than those found in the C=C stretching region from 1650 cm^{-1} to 1450 cm^{-1}, and the -C-H and =C-H stretch region from 3130 cm^{-1} to 2840 cm^{-1}, as well as the aromatic ring vibrations at > 3200 cm^{-1}. The signatures found in the 795 cm^{-1} to 673 cm^{-1} range are predominantly resulting from aryl C-H out-of-plane bending vibrations[40].

1.5 Summary

In short, this thesis focuses on four specific aims combining towards a common goal: to develop and characterize possibly compact – ideally hand-held - gas sensor for benzene, toluene, and xylenes detection and discrimination at trace levels with possibly short response times. Mid-infrared spectroscopy is as applied as the analytical technique using FT-IR and QCL light sources. FT-IR is used to verify that BTX can be discriminated and simultaneously quantified at ppm to ppb levels in the gas phase by analyzing spectral features within the fingerprint region with and without preconcentration. Research on QCLs demonstrates enhanced spectral density, and the potential for wide tuning capability for precisely overlapping the emission frequency with relevant analyte absorptions, and pave the way toward miniaturized devices.

References

[1]J. Faist, F. Capasso, D.L. Sivco, C. Sirtori, A.L. Hitchinson, and A.Y. Cho, Quantum Cascade Laser. Science 264 (1994) 553-556.

[2]H.J. Heger, R. Zimmermann, R. Dorfner, M. Beckmann, H. Griebel, A. Kettrup, and U. Boesl, Online Emission Analysis of Polycyclic Aromatic Hydrocarbons down to pptv Concentration Levels in the Flue Gas of an Incineration Pilot Plant with a Mobile Resonance-Enhanced Multiphoton Ionization Time-of-Flight Mass Spectrometer. Analytical Chemistry 71 (1999) 46-57.

[3]C.-W. Lin, Hazardous Air Pollutant Source Emissions for a Chemical Fiber Manufacturing Facility in Taiwan. Water, Air, and Soil Pollution 128 (2001) 321-337.

[4]P. Iovino, R. Polverino, S. Salvestrini, and S. Capasso, Temporal and spatial distribution of BTEX pollutants in the atmosphere of metropolitan areas and neighbouring towns. Environmental Monitoring and Assessment 150 (2009) 437-444.

[5]C. Gariazzo, A. Pelliccioni, P. Di Filippo, F. Sallusti, and A. Cecinato, Monitoring and Analysis of Volatile Organic Compounds Around an Oil Refinery. Water, Air, and Soil Pollution 167 (2005) 17-38.

[6]C. Lee, Y.J. Kim, S.-B. Hong, H. Lee, J. Jung, Y.-J. Choi, J. Park, K.-H. Kim, J.-H. Lee, K.-J. Chun, and H.-H. Kim, Measurement of Atmospheric Formaldehyde and Monoaromatic Hydrocarbons using Differential Optical Absorption

Spectroscopy during Winter and Summer Intensive Periods in Seoul, Korea. Water, Air, and Soil Pollution 166 (2005) 181-195.

[7]A. Volz-Thomas, J. Slemr, S. Konrad, T.H. Schmitz, E.C. Apel, and V.A. Mohnen, Quality Assurance of Hydrocarbon Measurements for the German Tropospheric Research Focus (TFS). Journal of Atmospheric Chemistry 42 (2002) 255-279.

[8]S.-H. Yeom, and A.J. Daugulis, A two-phase partitioning bioreactor system for treating benzene-contaminated soil. Biotechnology Letters 23 (2001) 467-473.

[9]K.-H. Kim, S.K. Pandey, and R. Pal, Analytical bias among different gas chromatographic approaches using standard BTX gases and exhaust samples. Journal of Separation Science 32 (2009) 549-558.

[10]K. Elke, E. Jermann, J. Begerow, and L. Dunemann, Determination of benzene, toluene, ethylbenzene and xylenes in indoor air at environmental levels using diffusive samplers in combination with headspace solid-phase microextraction and high-resolution gas chromatography–flame ionization detection. Journal of Chromatography A 826 (1998) 191-200.

[11]P.D. Kalabokas, J. Hatzianestis, J.G. Bartzis, and P. Papagiannakopoulos, Atmospheric concentrations of saturated and aromatic hydrocarbons around a Greek oil refinery. Atmospheric Environment 35 (2001) 2545-2555.

[12]F. Augusto, J. Koziel, and J. Pawliszyn, Design and validation of portable SPME devices for rapid field air sampling and diffusion-based calibration. Anal. Chem 73 (2001) 481-486.

[13]J. Koziel, M. Jia, and J. Pawliszyn, Air sampling with porous solid-phase microextraction fibers. Anal. Chem 72 (2000) 5178-5186.

[14]F.V. Parreira, Evaluation of indoor exposition to benzene, toluene, ethylbenzene, xylene, and styrene by passive sampling with a solid-phase microextraction device. Journal of chromatographic science 40 (2002) 122.

[15]S. Tumbiolo, J.F. Gal, P.C. Maria, and O. Zerbinati, Determination of benzene, toluene, ethylbenzene and xylenes in air by solid phase micro-extraction/gas chromatography/mass spectrometry. Analytical and bioanalytical chemistry 380 (2004) 824-830.

[16]V. Larroque, V. Desauziers, and P. Mocho, Development of a solid phase microextraction (SPME) method for the sampling of VOC traces in indoor air. Journal of Environmental Monitoring 8 (2006) 106-111.

[17]S. Tumbiolo, J.F. Gal, P.C. Maria, and O. Zerbinati, SPME sampling of BTEX before GC/MS analysis: Examples of outdoor and indoor air quality measurements in public and private sites. Annali di chimica 95 (2005).

[18]D. Gorlo, B. Zygmunt, M. Dudek, A. Jaszek, M. Pilarczyk, and J. Namie nik, Application of solid-phase microextraction to monitoring indoor air quality. Analytical and bioanalytical chemistry 363 (1999) 696-699.

[19]V. Larroque, V. Desauziers, and P. Mocho, Comparison of two solid-phase microextraction methods for the quantitative analysis of VOCs in indoor air. Analytical and bioanalytical chemistry 386 (2006) 1457-1464.

[20]J. Atienza, P. Aragón, M.A. Herrero, R. Puchades, and Á. Maquieira, State of the Art in the Determination of MTBE in Natural Waters and Soils. Critical Reviews in Analytical Chemistry 35 (2005) 317-337.

[21]F.J. Santos, and M.T. Galceran, Modern developments in gas chromatography–mass spectrometry-based environmental analysis. Journal of Chromatography A 1000 (2003) 125-151.

[22]H.L.C. Meuzelaar, J.P. Dworzanski, N.S. Arnold, W.H. McClennen, and D.J. Wager, Advances in field-portable mobile GC/MS instrumentation. Field Analytical Chemistry & Technology 4 (2000) 3-13.

[23]S. Zampolli, I. Elmi, J. Stürmann, S. Nicoletti, L. Dori, and G.C. Cardinali, Selectivity enhancement of metal oxide gas sensors using a micromachined gas chromatographic column. Sensors & Actuators: B. Chemical 105 (2005) 400-406.

[24]S. Zampolli, I. Elmi, F. Mancarella, P. Betti, E. Dalcanale, G.C. Cardinali, and M. Severi, Real-time monitoring of sub-ppb concentrations of aromatic volatiles with a MEMS-enabled miniaturized gas-chromatograph. Sensors & Actuators: B. Chemical (2009).

[25]J.W. Leonhardt, A new ppb-gas analyzer by means of GC-ion mobility spectrometry (GC-IMS). Journal of Radioanalytical and Nuclear Chemistry 257 (2003) 133-139.

[26]Y. Ueno, T. Horiuchi, O. Niwa, H.S. Zhou, T. Yamada, and I. Honma, Portable automatic BTX measurement system with microfluidic device using mesoporous silicate adsorbent with nano-sized pores. Sensors & Actuators: B. Chemical 95 (2003) 282-286.

[27]Y. Ueno, A. Tate, O. Niwa, H.S. Zhou, T. Yamada, and I. Honma, High benzene selectivity of mesoporous silicate for BTX gas sensing microfluidic devices. Analytical and bioanalytical chemistry 382 (2005) 804-809.

[28]E. Sokol, K.E. Edwards, K. Qian, and R.G. Cooks, Rapid hydrocarbon analysis using a miniature rectilinear ion trap mass spectrometer. The Analyst 133 (2008) 1064-1071.

[29]U. Platt, D. Perner, and H.W. Pätz, Simultaneous measurement of atmospheric CH_2O, O_3, and NO_2 by differential optical absorption. Journal of Geophysical Research 84 (1979) 6329-6335.

[30]K.H. Kim, Comparison of BTX measurements using a differential optical absorption spectroscopy and an on-line gas chromatography system. Environmental engineering science 21 (2004) 181-194.

[31]C. Lee, Y.J. Kim, S.B. Hong, H. Lee, J. Jung, Y.J. Choi, J. Park, K.H. Kim, J.H. Lee, and K.J. Chun, Measurement of atmospheric formaldehyde and monoaromatic hydrocarbons using differential optical absorption spectroscopy during winter and summer intensive periods in Seoul, Korea. Water, Air, & Soil Pollution 166 (2005) 181-195.

[32]K. Schäfer, Non-Intrusive measurements of aircraft and rocket exhaust emissions. Air & Space Europe 3 (2001) 104-108.

[33]K. Badjagbo, S. Sauvé, and S. Moore, Real-time continuous monitoring methods for airborne VOCs. Trends in Analytical Chemistry 26 (2007) 931-940.

[34]M. Lamotte, P. de Violet, P. Garrigues, and M. Hardy, Evaluation of the possibility of detecting benzenic pollutants by direct spectrophotometry on PDMS solid sorbent. Analytical and bioanalytical chemistry 372 (2002) 169-173.

[35]B. Lechner, H. Paar, and P.J. Sturm, Measurement of VOCs in vehicle exhaust by extractive FTIR spectroscopy, 2001, pp. 432.

[36]A. Sedlmaier, K. Schaefer, K.H. Becker, K. Brockmann, J. Heland, R. Kurtenbach, J. Loerzer, and P. Wiesen, Determination of VOCs in traffic exhaust by FTIR absorption spectrometry, 1999, pp. 176.

[37]C. Charlton, B.T. Thompson, and B. Mizaikoff, Hollow waveguide infrared spectroscopy and sensing. in: G. Orellana, and M.C. Moreno-Bondi, (Eds.), Springer Series on Chemical Sensors and Biosensors, Springer-Verlag, Heidelberg, 2005, pp. 133-167.

[38]J.A. Harrington, A review of IR transmitting, hollow waveguides. Fiber and Integrated Optic 19 (2000) 211-227.

[39]C. Young, S. Hartwig, A. Lambrecht, S.-S. Kim, and B. Mizaikoff, Optimizing Gas Sensors Based on Quantum Cascade Lasers and Photonic Bandgap Hollow Waveguides, IEEE Sensors, Atlanta, GA, 2007, pp. 1345-1348

[40]R.M. Silverstein, and G.C. Bassler, Spectrometric Identification of Organic Compounds, John Wiley & Sons, Inc., New York, 1967.

CHAPTER 2

FT-IR HWG TRACE GAS SENSORS FOR BTX DETECTION WITH UNIVARIATE AND MULTIVARIATE CALIBRATION

This chapter establishes direct, simultaneous, and molecularly selective detection of BTX at parts-per-million concentration levels using a FT-IR hollow waveguide (HWG) trace gas sensor with a response time of 39 seconds. Univariate calibration established limits of detection for benzene, toluene, and meta-xylene at 5, 11, and 17 ppm, respectively with high ”goodness of fit”. To adapt for real-world air sampling conditions with molecularly complex background signatures, a multivariate calibration model was established to predict concentrations of BTX within gas mixtures. This model was built using a partial least squares regression algorithm with a training set of 110 samples enabled by a customized gas mixing system.

2.1 Introduction

2.1.1 Motivation

Currently, there is increasing interest in trace gas sensing of aromatic hydrocarbons, such as benzene, toluene, and xylenes (BTX), with sensitivity, selectivity and short response times. Most commercially available hand-held BTX sensors are photoionization detectors (PID) or are colorimetric devices rendering them univariate to be quantitative and accurate. Univariate sensors are only capable of detecting one chemical compound at a

time, and do not allow simultaneous quantitative discrimination among multiple target compounds such as BTX constituents in complex environmental matrices. Instruments considered multivariate, such as gas chromatography and mass spectrometry techniques, are limited in quantitatively distinguishing between xylene isomers due to their innate similar molecular structure and molecular weight, typically requiring selective pretreatment/preconcentration (and desorption) steps. In addition, such benchtop sensor platforms usually provide response times on the order of several minutes or more.

On the contrary, mid-infrared spectroscopy has proven to be an excellent alternative for trace level BTX detection demonstrating inherent molecular selectivity due to sharp transitions within the fingerprint region, as well as high sensitivity. Additionally, compared to GC-MS, mid-infrared spectroscopy appears to have higher potential for miniaturized sensor platforms due to the advent of wavelength-tunable quantum cascade lasers[1] (discussed in Chapters 4-6). Furthermore, the FT-IR HWG trace gas sensor presented herein already exhibits a response time of only 39 seconds, which is well within the practically required time resolution for most sensing applications.

2.1.2 Partial Least Squares (PLS) Regression

While FT-IR spectroscopy provides an inherent ability for selective detection of organic molecules, multivariate calibration schemes may still be needed due to the inability of univariate calibration to adapt to statistical variations of the signal, to peak overlap within complex matrices, and to unknown species interfering with analyte absorptions.[2] Partial least squares-regression (PLS) is a particularly valuable calibration method because it

simultaneously correlates changes in absorbance with changes in concentration, thereby rendering the model more suitable than others for analyzing real-world samples with complex matrices in real-time. PLS reduces both the spectral and concentration information into scores and loadings at the same time, as illustrated in Figure 2-1.

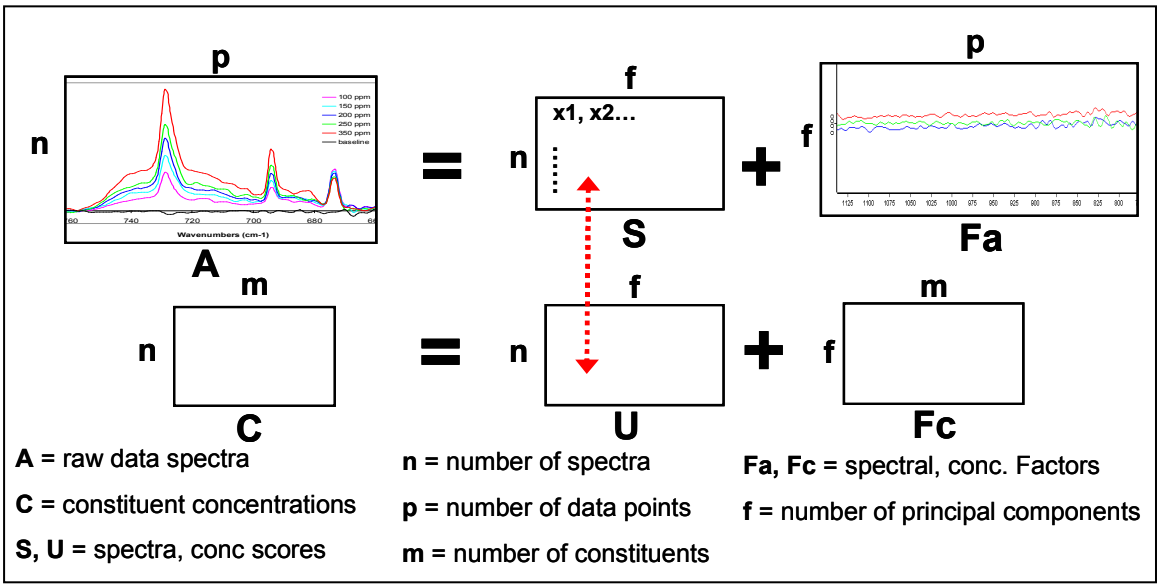

Figure 2-1: Spectral and concentration information in matrix format in PLS.

For PLS regression, the raw data spectra matrix (wavelength and absorbance, labeled "A" in Figure 2-1) is considered the "X block", while the concentration matrix (labeled "C" in Figure 2-1) is considered the "Y block" for a number of x training set standards. These blocks are reduced to only a few factors, so that spectral data may be represented by

$$X = t_1 p_1^T + t_2 p_2^T + t_3 p_3^T + \ldots + t_R p_R^T + F \qquad \text{(Eqn. 2-1)}$$

and concentration data may be represented by

$$X = t_1 q_1^T + t_2 q_2^T + t_3 q_3^T + ... + t_R q_R^T + G \qquad \text{(Eqn. 2-2)}$$

where t_i are the scores vectors, p_i or q_i are the loadings vectors, R is the number of factors, T represents the transpose of the respective loading vectors, and F and G are the residual matrices[2, 3].

From this regression, factors - also known as latent variables - are generated, which contain all relevant information needed for the calibration. A plot of the root mean square error of cross-validation (RMSECV) versus the number of latent variables yields the most likely number of factors, which should be selected to calculate a sufficiently robust model. It should be noted that most (analytically) relevant information is usually contained within the first few latent variables, and therefore the lowest number of latent variables should be used that avoids "underfitting" (not including enough information for the prediction of unknown samples), yet prevents "overfitting" (modeling spectral noise and not just the changes in spectra which correlate to concentration).

Building a PLS model ultimately results in the derivation of a calibration function that is used to calculate the concentration of an unknown sample introduced to the model.[2-6] Principle components regression (PCR) is another multivariate technique that is similar to PLS; however, the potential problem with PCR is that the loading vectors, which best represent the spectral data, may not be optimal for concentration prediction.[5] Additionally, the spectral vectors using PLS directly relate to the constituents of interest and consider the concentration matrix simultaneously, whereas PCR only considers

spectral variations without regard to the constituents of interest until the final – separate - regression step.

2.2 Materials and Methods

2.2.1 Preparation of Multivariate Gas Calibration Standards

Calibration standards were produced using the dilution method for preparing the desired concentration of each individual component of a multi-gas mixture, which consists of introducing two streams of gas - analyte(s) and diluent – into a static mixer. A schematic of the custom gas mixing system is described in Figure 2-2.

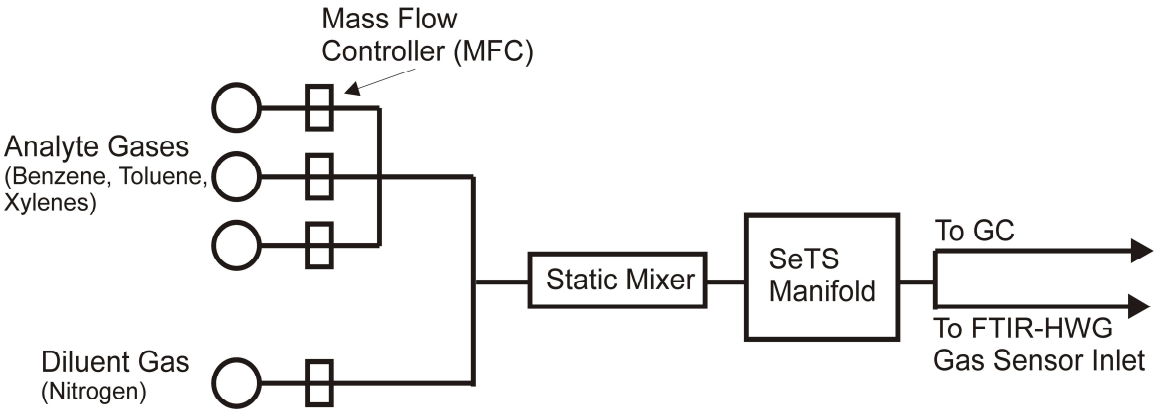

Figure 2-2: Schematic of custom gas mixing and delivery system (SeTS) for the preparation of calibration standards.

Analyte gases were individual cylinders of benzene, toluene, meta-xylene (for univariate calibration), or ortho, para, meta (o,p,m) - xylenes (Airgas, Port Allen, LA); certified standards at a concentration of 100 ppm (+/- 2%) in nitrogen balance.

Dilution of analyte gases was achieved by using mass flow controllers (MFCs) (Brooks Instrument, Hatfield, PA) to deliver a known and constant flow of diluent gas, which was nitrogen (Airgas, Port Allen, LA) throughout these studies, to the analyte gas stream(s), which were also of known and constant flow. The diluent stream MFC was calibrated for a range of 0-30 standard liters per minute (SLPM), and the analyte gas stream MFCs were calibrated for a range of 0 – 300 standard cubic centimeters per minute (SCCM). The final concentration of an analyte delivered to the FT-IR HWG gas sensor can be calculated by

$$[Desired\ Analyte] = \left(\frac{Analyte\ Gas\ Flowrate}{Process\ Stream\ Total\ Flowrate} \right) \times [Analyte\ Gas\ Standard]$$

(Eqn. 2-3)

where rectangular brackets denote concentrations, and *process stream total flowrate* describes the summation of analyte and diluent gas flows. The diluent gas flow can be determined by

$$Diluent\ Flowrate = Process\ Stream\ Total\ Flowrate - \left(\sum Analyte\ Gas\ Flowrates \right)$$

(Eqn. 2-4)

A custom-written Labview program (National Instruments, Austin, TX) was designed to operate and control all mass flow controllers to produce the desired analyte concentrations according to the equations above.

2.2.2 Validation by Gas Chromatography

The custom gas mixing system was externally validated using gas chromatography at the operating conditions listed in Table 2-1.

Initial Oven Temperature	60° C
Initial Hold Time	5 min
Ramp Rate A	20° C/min
Final Oven Temperature	80° C
Final Hold Time	4 min
Split Inlet Temperature	225° C
FID Temperature	250° C
FID Air	400 ml/min
FID Hydrogen	40 ml/min
FID Helium Make-Up	30 ml/min
Constant Column Pressure	9 psi
Split Flow	100 ml/min
Column Flow at 60° C	.66 ml/min
Split Ratio	58/1

Table 2-1: GC operating conditions.

A Hewlett Packard 5890 GC with a J&W 30M, 0.25 mm ID, 0.25 micron DB-1 column was used to provide component separation. The GC was configured with a split / split-less inlet and flame ionization detector (FID). The sample stream being analyzed was diverted from the sensor testing system (SeTS) manifold gas outlet to a Valco Multiport GC sampling valve (VICI Valco Instruments, Houston, TX) via a 6 port switching valve. The Valco 16 loop sampling valve collected 15 separate samples over time. The volume of each sample loop size was 3 mL to allow large volume injections. Analyses were conducted in splitless mode. Figure 2-3 presents the individual univariate calibration GC results for BTX confirming accurate and precise delivery of the desired analyte concentrations to the FT-IR HWG trace gas sensor.

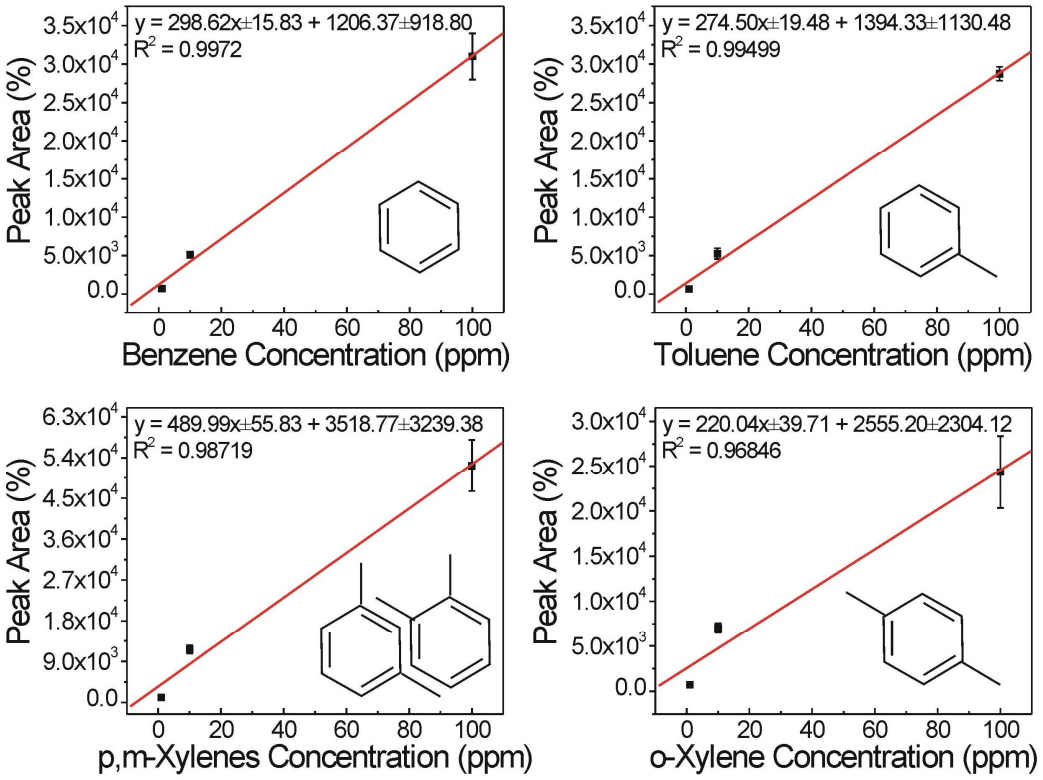

Figure 2-3: GC univariate calibration of BTX verifying custom gas mixing system performance. Each data point represents an average of fourteen loops.

Each concentration is an average of 14 of the 16 sample loops where one sample loop was determined to have a leak and was not considered for the present calibration.

2.2.3 Experimental Design

A training set with linearly independently varied concentrations of the BTX constituents was developed to model the behavior of the sensing system.[7] The training set used during the measurements reported in this chapter is based on a minimum correlation table[8] (Appendix A) in which concentrations of toluene and xylenes were varied randomly against benzene to avoid collinearity. This approach produced a set of randomized analyte concentration values, as graphically depicted in Figure 2-4.

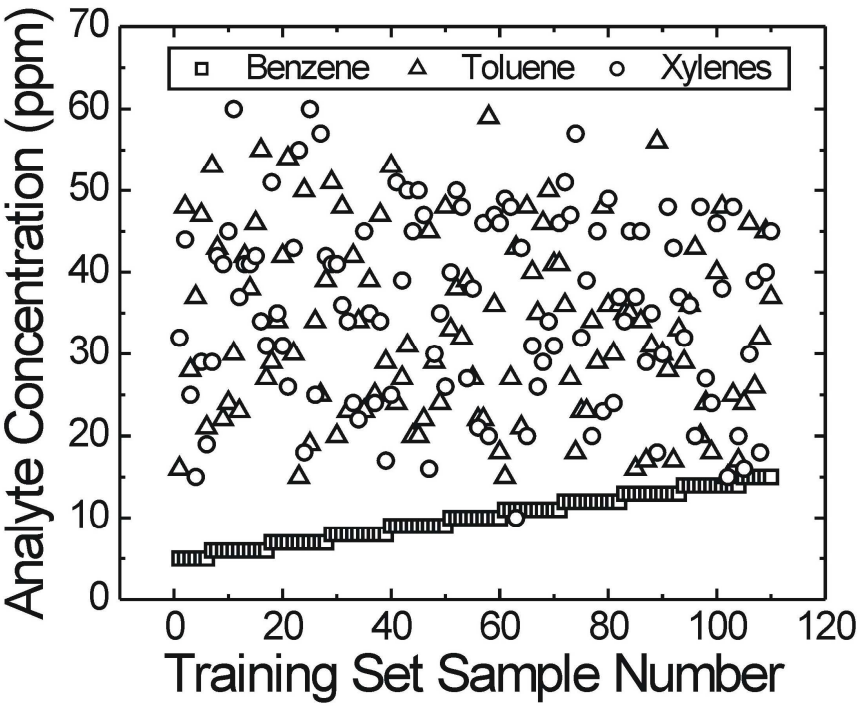

Figure 2-4: Training set analyte concentration values for BTX.

The training set contained 110 calibration standards each comprising five analytes per standard varying within concentration levels of 5 – 15 ppm for benzene, 15 – 59 ppm for toluene and 10 – 60 ppm for o,p,m-xylenes. Standards were executed in random order using a random number generator. Appendix A tabulates the analyte concentration values in Figure 2-4 according to training set mixture and random run order.

Constituents were plotted against each other to confirm the absence of linear relationships, as illustrated in Figure 2-5.

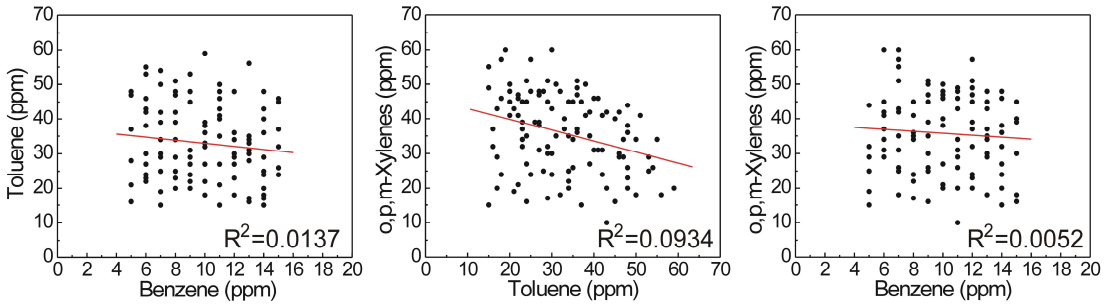

Figure 2-5: Relationship between constituent concentrations from the training set.

Low "goodness of the fit", as demonstrated in Figure 2-5, indicates a lack of correlation in concentration between constituents, thus confirming true randomization and avoiding any inherent dependency of concentration on constituent spectral features.

2.2.4 Optical Setup

A portable Fourier-transform infrared spectroscopy (FT-IR) hollow waveguide (HWG) trace gas sensor was developed and built in the course of this thesis. A diagram of the experimental setup is presented in Figure 2-6.

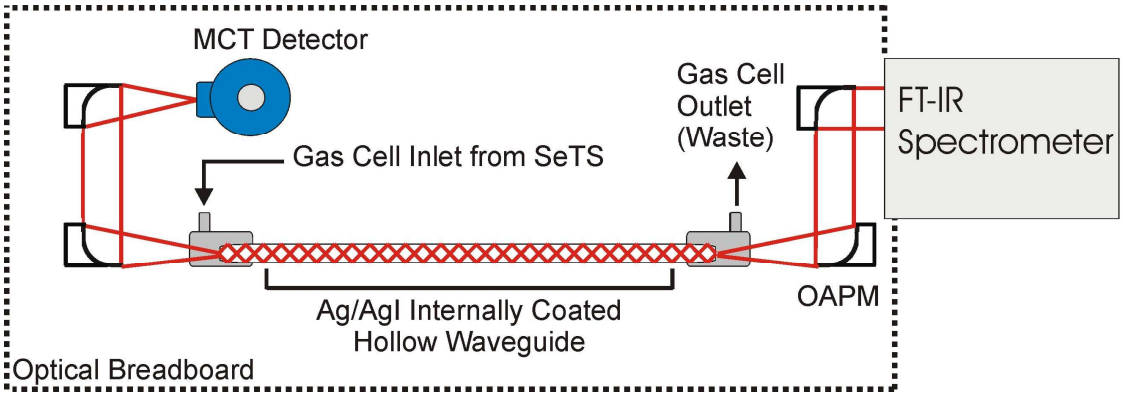

Figure 2-6: Diagram of a portable FT-IR HWG trace gas sensor.

Gold-coated off-axis parabolic mirrors (OAPM) externally focused incident radiation from a Bruker Matrix M FT-IR spectrometer (Bruker Optics, Billerica, Massachusetts) into a custom-made IR transparent gas cell attached to the gas inlet of the HWG. At the distal end of the HWG, also capped off with a gas cell, radiation was focused onto a liquid nitrogen cooled MCT detector (Infrared Assoc., Stuart, FL) after propagation through the waveguide resulting in broadband transmission/absorption spectra recorded from 4000 to 600 cm^{-1}. A labeled image of this setup is presented in Figure 2-7.

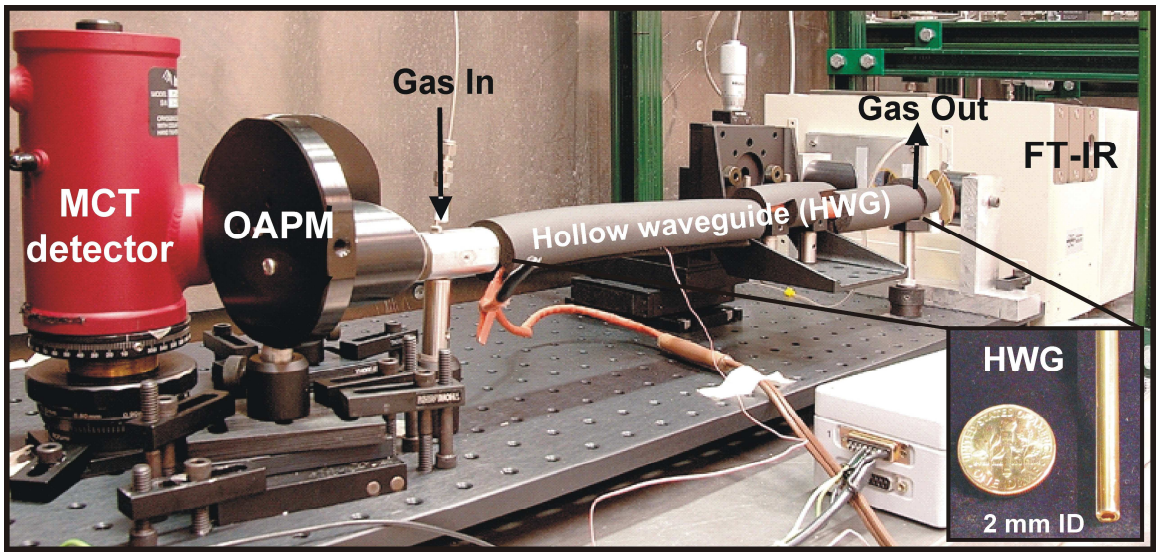

Figure 2-7: FT-IR HWG trace gas sensor. Photo courtesy of ExxonMobil Research and Engineering, Co.

Mid-infrared absorption spectra were collected using a spectral resolution of 2 cm^{-1}, and by averaging 100 spectra scans per measurement resulting in a response time of 39 seconds/final spectrum. The response time may be further reduced by increasing the spectral resolution, yet needs to be optimized for individual measurement scenarios as to determine which sacrifice in terms of sensitivity and selectivity (if multi-components are

present) is analytically acceptable. It should be noted that all measurements described herein directly probed the analyte present within the HWG without any preconcentration. All gas standards were injected from the custom gas mixing system (SeTS; previously described) into the custom-made HWG gas cell inlet via a 1⁄16″ stainless steel capillary connected via Swagelok airtight connections. All piping connections from the custom gas mixing system to the HWG gas cell inlet were leak tested with Snoop® leak detector liquid prior to any data collection. The HWG was temperature stabilized at 50 deg C using a heating jacket to prevent possible adherence of the analyte or condensation at the inside walls of the HWG.

2.2.5 Multivariate Calibration

Multivariate spectral analysis was accomplished by the established partial least squares regression model. Computations were performed with Mathworks Matlab version 7.4 (2007a) and PLS Toolbox version 4.1.1 (Eigenvector Research Inc., Wenatchee, WA).

Preprocessing of the spectra (details see below) isolated the contributable variation toward the BTX concentration data. Exemplary raw data of multivariate spectra are shown in Figure 2-8 with increasing benzene concentration and randomly varied concentration of toluene and the xylenes.

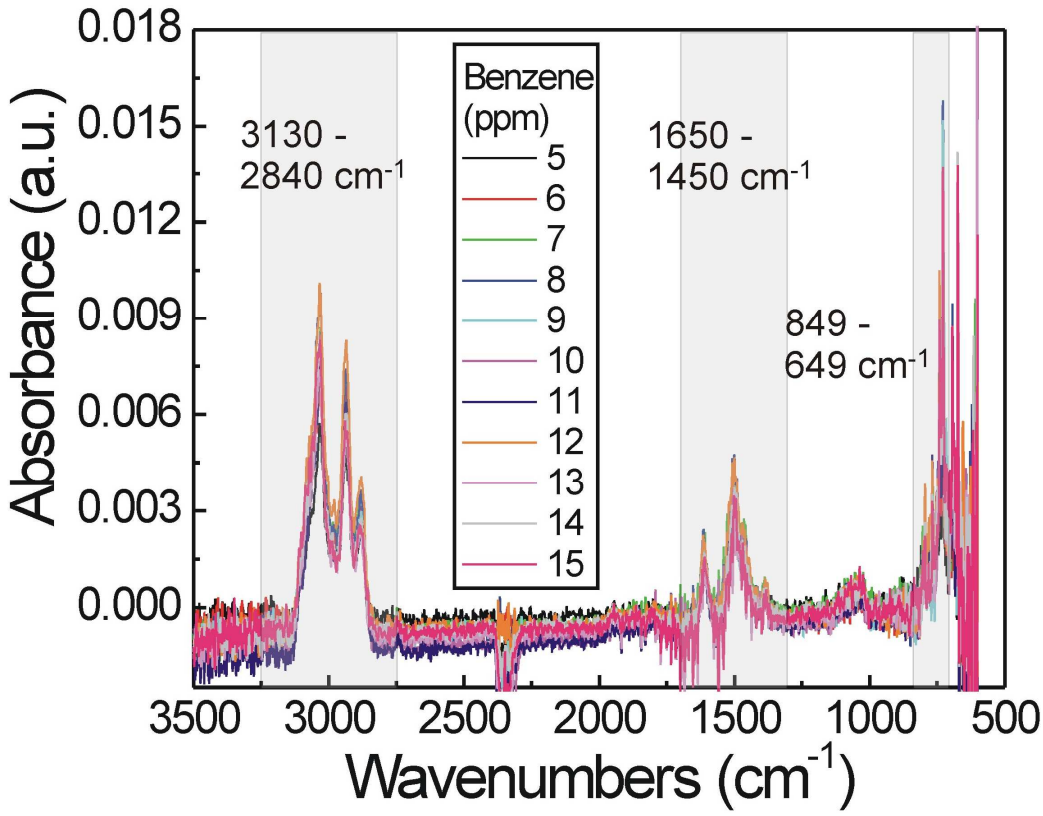

Figure 2-8: Raw data spectra of ppm-level BTX where the concentration of benzene is varied from 5 – 15 ppm, while toluene and xylenes concentrations are randomly varied. The shaded boxes identify the spectral regions of interest for multivariate calibrations.

In order to remove background contributions and some spectral noise, preprocessing of the spectra by multiplicative scatter correction (MSC)[3] was applied to the spectra. Three regions of interest for more in-depth data analysis were isolated; the =C-H bending and ring torsion region from 649 cm^{-1} to 849 cm^{-1}, the C=C stretching region from 1450 cm^{-1} to 1650 cm^{-1}, and the -C-H and =C-H stretch region from 2840 cm^{-1} to 3130 cm^{-1}. Two of the three regions were found to provide the best combination of spectral signal-to-noise (S/N) ratio and correlation to concentrations of BTX components. Further preprocessing by normalization to unit area and mean centering generated the final spectral row space.

Exemplary spectra after final preprocessing are shown in Figure 2-9, and were utilized to generate the multivariate model.

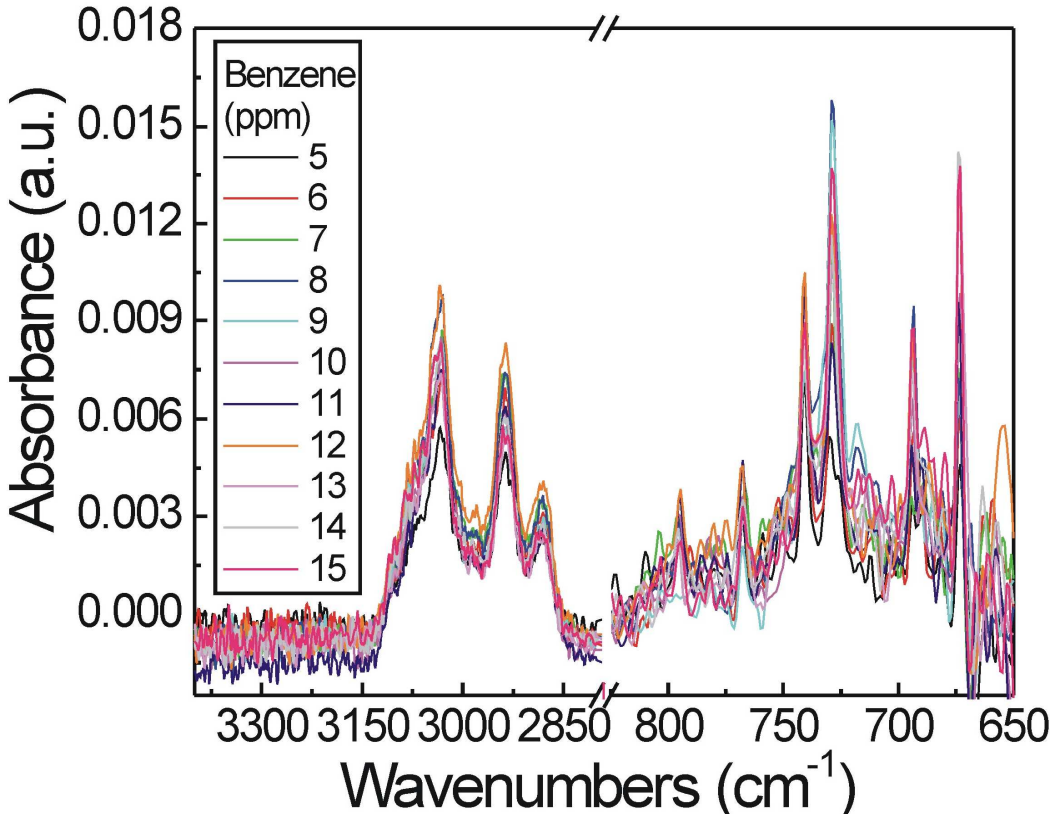

Figure 2-9: Select spectral regions used to generate the multivariate model.

The evaluation of the calibration model performance was performed via RMSECV. RMSECV was performed by removing random subsets of 10 spectra, building the PLS model using the remaining 100 spectra, and utilizing the model to estimate the concentration of BTX in the 10 removed spectra serving as quasi-unknowns. This procedure is known as cross-validation and was performed 11 times for one repetition such that every sample was removed and estimated exactly once. A total of 20 cross-validation repetitions were averaged to finally achieve a robust RMSECV as a measure of

individual model performance. Minimization of the RMSECV finally determined the optimal complexity of the calibration model.

2.3 Results and Discussion

2.3.1 Univariate Calibration of BTX

Univariate calibration relies on separated absorbance features for each analyte, which are individually evaluated by determining the peak height or by integrating the absorbance peak. Unknown concentrations of that analyte are then determined by the relationship between absorbance and concentration following the Beer-Lambert law, which yields a calibration function as discussed in Chapter 1. Figure 2-10 presents exemplary spectra for benzene, toluene, and meta-xylene at varying concentrations.

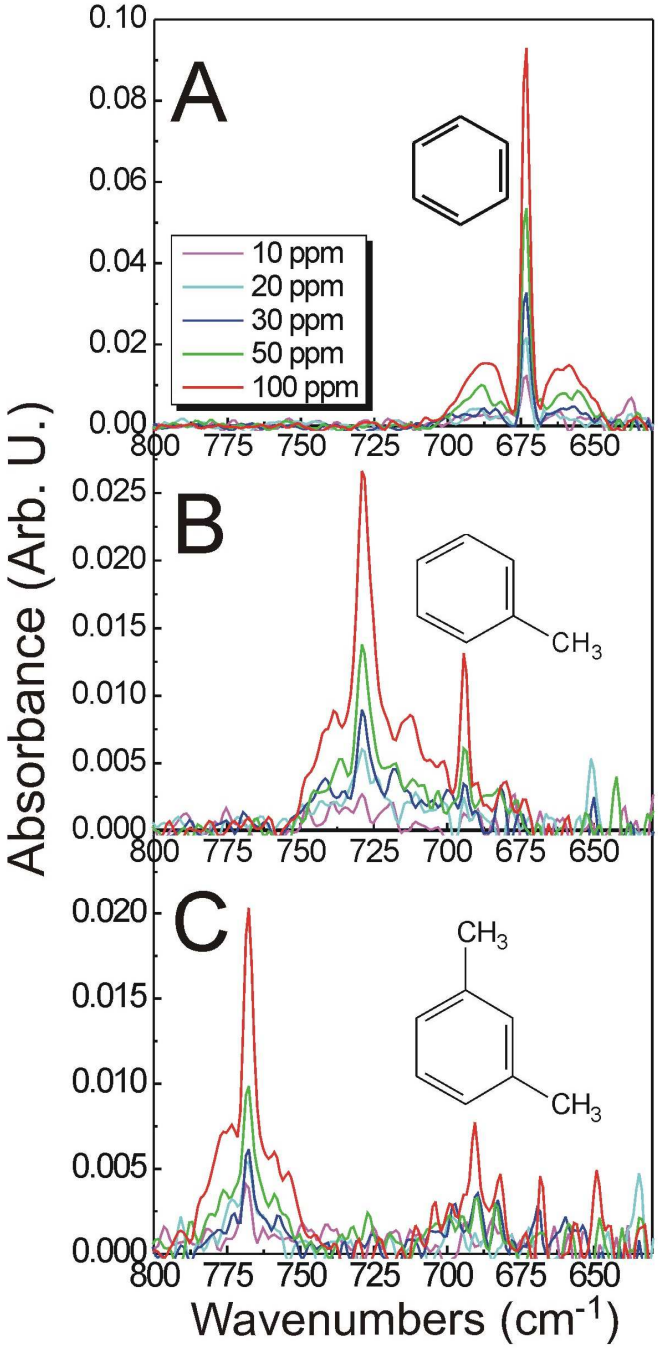

Figure 2-10: Exemplary mid-infrared spectra of ppm benzene (A), toluene (B), and meta-xylene (C).

Figure 2-11 presents the obtained univariate calibrations for BTX.

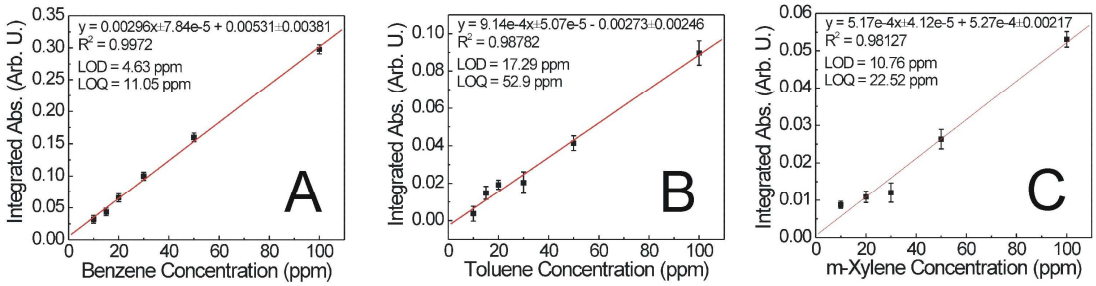

Figure 2-11: Univariate calibration of ppm benzene (A), toluene (B), and meta-xylene (C). Each data point of the calibration curves represents an average of three trials, nine spectra/trial where each individual spectrum was an average of one hundred.

Limits of detection (using 3σ as the criterion) were calculated as 5 ppm, 17 ppm, and 11 ppm, and limits of quantification (using 6σ as the criterion) as 11 ppm, 53 ppm, and 23 ppm for benzene, toluene, and meta-xylene, respectively. It should be noted that these detection limits are dependent on the selected spectral resolution, and on the number of averaged spectra; therefore, these values may be optimized for specific sensing applications using e.g. lower resolution and/or more averaged spectra providing for an enhanced signal-to-noise ratio. However, the sensor response time would increase accordingly.

2.3.2 Multivariate Calibration of BTX

As previously mentioned, partial least squares regression was used to build a multivariate calibration model for ppm-level BTX sensing. Outlier samples 4, 5, 94, and 105 were removed from the initial 110 samples within the training set. The calibration model performance for predicting the absolute concentration of BTX is shown in Figure 2-12.

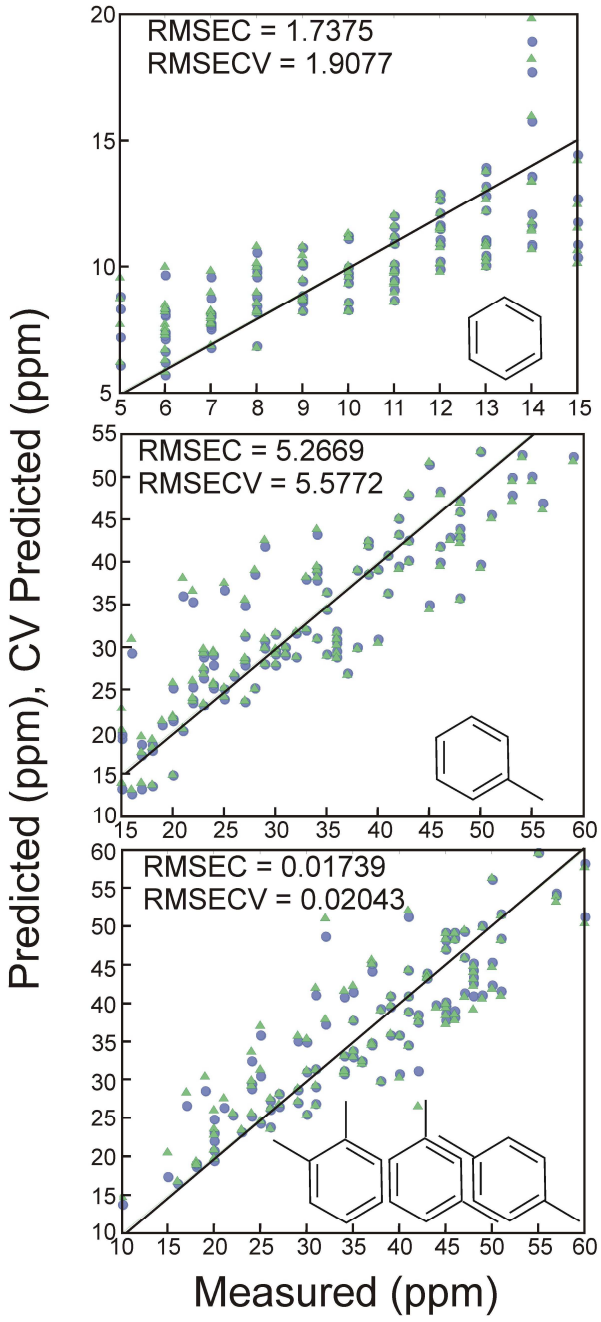

Figure 2-12: Performance of the PLS regression model for estimating the absolute concentration of benzene, toluene, and xylenes. Circles represent each sample during calibration, triangles represent each sample during cross-validation.

PLS calibration figures of merit for absolute concentrations of the three individual BTX components in mixtures are summarized in Table 2-2.

Constituent	**Absolute Concentration Range**	**Calibration Error (%)**	**Cross-Validation Error (%)**
Benzene	5 ppm – 15 ppm	1.7 ppm (17%)	1.9 ppm (20%)
Toluene	15 ppm – 59 ppm	5.2 ppm (12%)	5.7 ppm (13%)
Xylenes	10 ppm – 60 ppm	5.0 ppm (10%)	5.7 ppm (12%)

Table 2-2: PLS calibration figures of merit for absolute concentration.

In the case of evaluating absolute concentrations, cross-validation errors on the order of 2 ppm to 6 ppm (10% to 20% of the concentration ranges used to create the mixtures) were achieved. These errors were slightly larger than expected. Univariate calibration methods returned standard deviations of the regression of 2 ppm to 6 ppm; a more pronounced signal averaging benefit was expected from the PLS regression.

The training set used here was initially designed to quantitatively determine low ppm concentrations of benzene in mixtures at notably higher ppm concentrations of toluene and xylenes, which corresponds to real-world in-field industrial scenarios. Consequently, there are a couple of factors that may have limited accuracy and precision of the regression. The first is that the dynamic ranges for BTX were set in the low ppm range, which was not sufficiently above the limits of detections (3σ) derived from univariate calibrations and achievable with the present FT-IR HWG sensing system. Future optimization of the experimental design should focus on a wider dynamic range with

values well above the limit of quantification in addition to lower concentration values to train the model to recognize correlations between analyte concentration and spectral features with limited noise contribution. Another factor affecting the obtained results is that atmospheric carbon dioxide absorbs at 668 cm^{-1}, which - at very low benzene concentrations - significantly overlaps with the benzene absorbance at 674 cm^{-1}. Future optimization should thus be focused on designing a training set which takes into account carbon dioxide contribution using CO_2 as an additional calibrant, as well as incorporating benzene concentrations which produce absorbance larger than the carbon dioxide absorbance.

One method for optimizing the prediction capability is to normalize the spectra to unit area (that is, the total area under the spectra becomes unity), and to calibrate for percent relative concentration instead of absolute concentration values. This method also helps to correct for minute sample-to-sample variance in intensity, which may limit the reliability of the calibration model.

The calibration performance using relative concentrations is summarized in Table 2-3.

Constituent	**Relative Concentration Range**	**Calibration Error (%)**	**Cross-Validation Error (%)**
Benzene	0.05 – 0.32	0.010 (5.6%)	0.012 (4.4%)
Toluene	0.19 – 0.67	0.019 (4.0%)	0.021 (4.4%)
Xylenes	0.16 – 0.71	0.017 (3.1%)	0.020 (3.6%)

Table 2-3: PLS calibration figures of merit for relative concentrations.

The calibration model performance for predicting the relative concentration of BTX is shown in Figure 2-13.

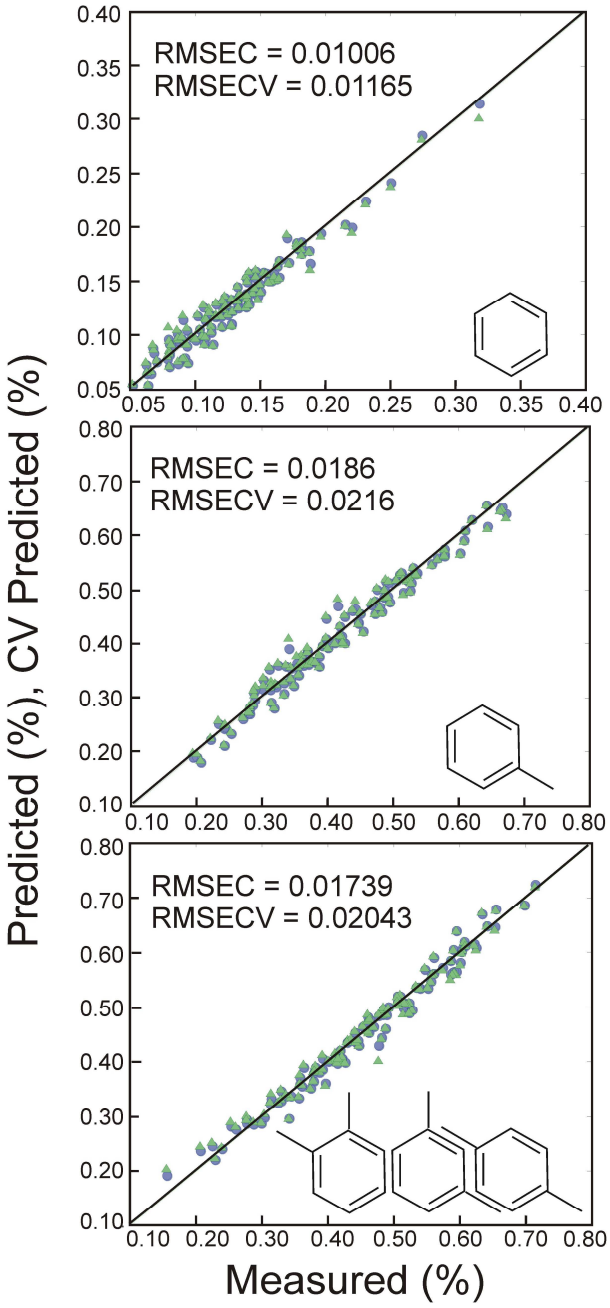

Figure 2-13: Performance of the PLS regression model for estimating the relative concentration of benzene, toluene, and xylenes. Circles represent each sample during calibration, triangles represent each sample during cross-validation.

Comparing the last two columns of Table 2-3 to the last two columns of Table 2-2, it is evident that the calibration model provides a much better quantitative fit to the data. The relative calibration and cross-validation errors (defined as relative to the range of concentrations in the calibration model for each analyte) are reduced by a factor of three.

2.4 Summary and Outlook

To summarize this chapter, direct and quantitative sensing of parts-per-million (ppm) BTX using a FT-IR-HWG trace gas sensor with a 39 second response time and without any sample preconcentration was demonstrated. Calculations from univariate calibration determined individual limits of detection (3σ) at 5 ppm for benzene, 17 ppm for toluene, and 11 ppm for meta-xylene, respectively. A multivariate calibration model was developed utilizing a custom gas mixing system to produce a 110 standard training set consisting of low benzene concentration range (5 to 15 ppm) with higher toluene and xylene constituent concentrations (20 to 65 ppm). Root mean squared errors of cross validation of 2 ppm for benzene, 5 ppm for toluene, and 5 ppm for total xylenes were realized. Normalization of the spectra to unit area prior to PLS model building presented RMSECV of 0.011 % constituency for benzene, 0.021 % constituency for toluene, and 0.018 % constituency for total xylenes.

While direct quantification of BTX via univariate and multivariate calibrations with a response time of less than a minute were achieved, limits of detection were in the low ppm concentration range, which are of limited suitability for some of the legally regulated exposure limits. However, there are other applications, such as process monitoring, in which direct measurement of ppm levels of BTX has utility. In the next chapter, an enhancement of the present FT-IR HWG method will be discussed, which integrates the developed trace gas sensor with preconcentration and thermal desorption for quantitatively determining BTX in environmental air samples at ppb concentration levels.

References

[1]J. Faist, F. Capasso, D.L. Sivco, C. Sirtori, A.L. Hitchinson, and A.Y. Cho, Quantum Cascade Laser. Science 264 (1994) 553-556.

[2]J.P. Conzen, A Practical Guide for Developing Methods in the Quantitative Analytical Chemistry, Bruker Optik, Ettlingen, 2003.

[3]P. Geladi, and B.R. Kowalski, Partial least-squares regression: a tutorial. Analytica chimica acta. 185 (1986) 1-17.

[4]E. Bouveresse, C. Hartmann, D.L. Massart, I.R. Last, and K.A. Prebble, Standardization of near-infrared spectrometric instruments. Anal. Chem 68 (1996) 982-990.

[5]D.M. Haaland, and E.V. Thomas, Partial least-squares methods for spectral analyses. 1. Relation to other quantitative calibration methods and the extraction of qualitative information. Analytical Chemistry 60 (1988) 1193-1202.

[6]H. Martens, and T. Naes, Multivariate Calibration, John Wiley & Sons, New York, 1989.

[7]P. Geladi, and B.R. Kowalski, Partial least-squares regression: a tutorial. Analytica Chimica Acta 185 (1986) 1-17.

[8]*Strategy of Experimentation*, Edition 4.2, E.I. du Pont de Nemours and Company, Wilmington (1988).

CHAPTER 3

PARTS-PER-BILLION BTX DETECTION USING PRECONCENTRATION-ASSISTED FT-IR HWG TRACE GAS SENSORS

This chapter discusses simultaneous, selective, parts-per-billion detection of BTX using a preconcentration / thermal desorption assisted FT-IR hollow waveguide (HWG) trace gas sensor. A calibration with a dynamic range of 1000 - 100 ppb analyte/N_2 was developed in the laboratory and utilized to predict the concentration of BTX in blinded environmental air samples. The predicted concentration results were in close agreement with the validation method used during these field studies (GC-FID), as well as several conventional and experimental analytical techniques used in industrial hygiene including GC-PID, ultra-fast GC-FID, and GC-DMS, which were simultaneously operated in the field.

3.1 Motivation and Introduction

3.1.1 Exposure Limits

Chapter 2 demonstrated simultaneous detection of BTX at ppm concentration levels during directly measurments without aby sample pretreatment, thereby resulting in a response time of only 39 seconds; however, environmentally relevant concentrations, and particularly of benzene, need to be determined at the low ppm to ppb concentration range. BTX exposure limits (ppm) set by the Occupational Safety and Health Administration (OSHA), the National Institute for Occupational Safety and Health (NIOSH), and the

American Conference of Governmental Industrial Hygienists (ACGIH) are listed in Table 3.1.

		OSHA	NIOSH	ACGIH
Benzene	TWA	1	0.1	0.5
	STEL	5	1	2.5
Toluene[§]	TWA	200	100	50
	STEL	[‡]	150	----
Xylenes	TWA	100	100	100
	STEL	----	150	150

Table 3-1: BTX exposure limits in ppm.

TWA represents the time weighted average over an eight hour period, and STEL is the short term exposure limit during 15 minutes. Notably, the exposure limits for benzene are significantly lower than for toluene and xylenes, where the TWA range varies from 1000 ppb to 100 ppb.

3.1.2 Sample Pretreatment

To lower detection limits from the ppm to the ppb range, a sample pretreatment step was introduced. In the work reported herein, gas adsorption onto an adsorbent material was used to preconcentrate gas standards or field samples prior to FT-IR HWG measurements. Subsequently, thermal desorption was used to release the trapped analytes as a concentrated plume into the hollow waveguide over time. Gas adsorption

[§] ACGIH threshold limit value (TLV) for toluene is 20 ppm.
[‡] Exposures shall not exceed 300 ppm (ceiling) with the following exception: exposures may exceed 300 ppm, but not more than 500 ppm (peak), for a single time period up to 10 minutes for any 8-hour shift. OSHA Standard 29 CFR 1910.1000.

occurs when the gas sample is allowed to equilibrate with the sorbent material such that the concentration of gas molecules is always greater at the surface than within the free gas volume.[1] During the present studies, gas adsorption was performed in an active sampling mode, i.e. the gas standard or field sample was pumped across the sorbent material - graphitized carbon black - and allowed to adsorb to the sorbent surface.

Graphitized carbon black is a non-porous material with a high surface area where adsorption interactions are only dependent on London dispersion forces.[2, 3] The material is also hydrophobic, which renders the surface especially useful for trapping VOCs in a humid environment, i.e. during field measurements. Furthermore, graphitized carbon black exhibits a Gaussian type adsorption energy distribution due to the high surface homogeneity.[3]

Pogodina, et. al. have previously used preconcentration and thermal desorption to measure ethene down to ~1 ppb in ambient air with a FT-IR HWG gas sensor.[4] The present chapter demonstrates ppb detection of BTX with a FT-IR-HWG trace gas sensor for the first time by establishing a sufficiently robust laboratory calibration enabling later in-field evaluation of blinded real-world samples determined at similar conditions using active sampling onto the sorbent material and thermal desorption. The prediction of BTX concentrations of field samples were independently validated by GC-FID, and compared to current off-the-shelf industrial hygiene devices and industrial prototypes utilized for evaluating the same samples during the same field measurement campaign.

3.2 Materials and Methods

3.2.1 Adsorption Material

The sorbent tubes utilized during the present studies were packed with Carbopack B 40/60 (Supelco Inc., Bellefonte, PA), a graphitized carbon black with a 60-80 mesh and a surface area ~100 m^2/g. A schematic of the sorbent tube is shown in Figure 3-1.

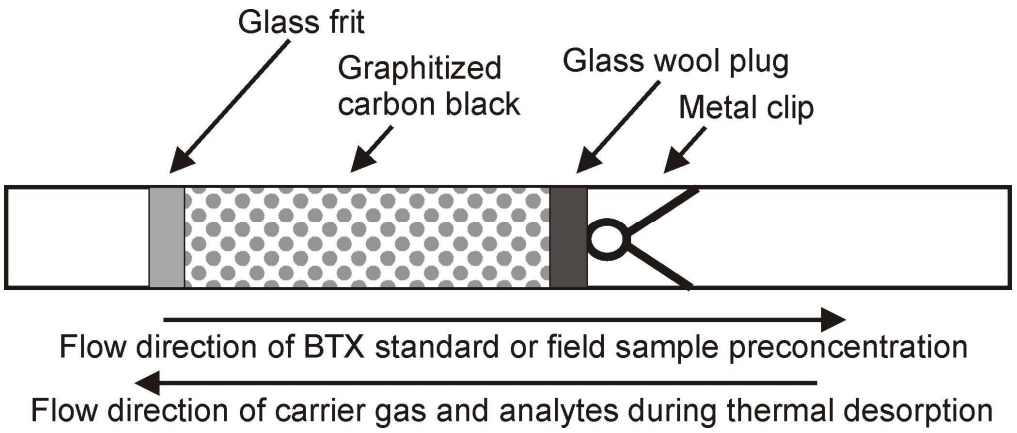

Figure 3-1: Sorbent tube schematic used for selective preconcentration and thermal desorption of analytes from gas standards or environmental air.

As shown in this figure, the flow direction of the BTX gas standard for laboratory calibrations or measurements of a field sample was glass-frit-first through the tube. The glass wool plug and the metal clip held the packed sorbent material in place.

Graphitized carbon black was selected as a suitable sorbent tube material for BTX based on its ability to selectively adsorb and release BTX, while limiting the amount of artifacts from the sampling and heating procedure. Tenax TA-packed sorbent tubes (Supelco Inc., Bellefonte, PA) were additionally evaluated, however, contributions to the toluene and

the benzene absorbance features evolved from the polymeric sorbent material, thereby leading to non-quantifiable results. Carbopack B sorbent tubes were conditioned for at least two hours by heating at 350 deg C and flowing ~50 mL/min of nitrogen through the tube. IR spectra using the FT-IR HWG system were continuously collected during preconditioning to confirm smooth baselines indicative of blank (zero-background) tubes and adequate preconditioning.

3.2.2 Adsorption Method

The sorption system consisted of a low flow sample pump (SKC model 222-3, Eighty Four, PA), which was used to draw the certified gas standard sample or field sample through a syringe needle that pierced the air-tight septum of the used Tedlar bags (SKC, Model 232, Eighty Four, PA). A syringe needle was used to ensure completely sealed gas transfer paths, and subsequently avoiding any possible gas leakage arising from sampling directly from the Tedlar bag release valve. All other openings to the bag including the side-arm valve were appropriately sealed. The sample pump withdrew gas from a 10 L capacity Tedlar bag (SKC, Model 232, Eighty Four, PA) across a sorbent tube at a rate of 162 mL/min for 7 min resulting in a volume of 1.1 L of gas sampled, as depicted in Figure 3-2.

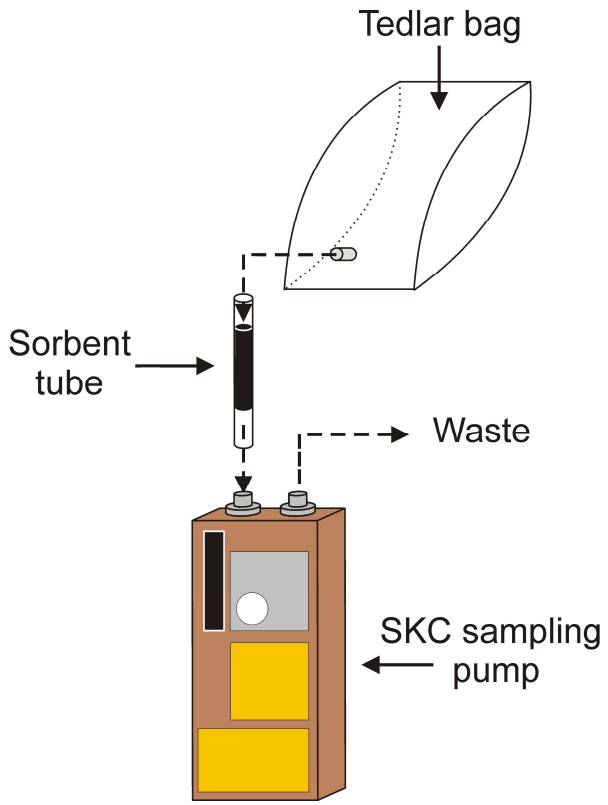

Figure 3-2: Schematic of the preconcentration experimental setup.

The sample pump flow was calibrated using a using manual SKC Model 303 film flowmeter (SKC, Eighty Four, PA).

3.2.3 Thermal Desorption

Thermal desorption was used to slowly release preconcentrated analytes over time into the hollow waveguide with consistent reproducibility. Following BTX adsorption onto the sorbent material, a Dynatherm ACEM 9300 thermal desorption (TD) unit (CDS Analytical, Oxford, PA, USA) was used to desorb the analytes of interest from the tube onto a focusing trap (also packed with Carbopack B) at a flowrate of 50 mL/min, and at a temperature of 150 °C for 5 min. The trap was maintained at temperatures < 40 °C during

collection, and subsequently flash heated to 300 °C for 30 min, thereby producing a concentrated time-resolved gas plume released into the HWG at a slow carrier gas flow, known henceforth as *column flow*.

3.2.4 Optical Setup

Introduction of the concentrated gas plume into the hollow waveguide (2 mm ID, 50 cm length) was achieved by custom-engineered gas cells with a small internal volume (~1 cm^3) and equipped with IR transparent zinc selenide (ZnSe) windows allowing coupling of the IR radiation into the waveguide. Incident radiation was externally coupled from a Bruker Matrix M spectrometer (Bruker Optics, Billerica, MA, USA) and directed into the output gas cell utilizing gold-coated off-axis parabolic mirrors (OAPM). Finally, the attenuated radiation was focused onto a liquid nitrogen cooled mercury-cadmium-telluride (MCT) detector (Infrared Associates Inc., Stuart, FL, USA) yielding a broadband transmission/absorption spectrum (4000 to 600 cm^{-1}). Figure 3-3 shows a schematic of this optical setup.

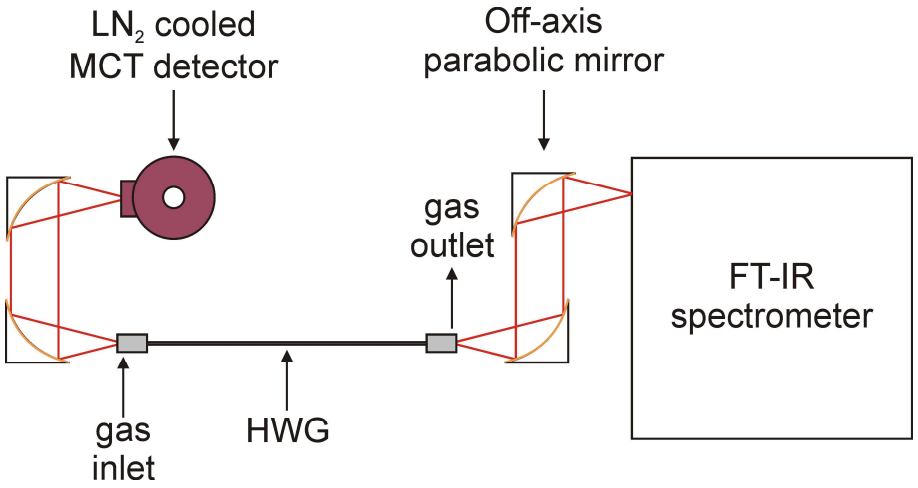

Figure 3-3: Diagram of optical setup.

The spectrometer was computer controlled and operated from outside the fume hood. The temperature of the HWG was elevated using a heating jacket (Watlow Electric Manufacturing Co., St. Louis, MO, USA) in an effort to minimize potential condensation or wall adsorption of BTX within the HWG. The collected spectra correspond to the averaged absorbances from 100 spectra scans at a spectral resolution of 2 cm^{-1}. Figure 3-4 describes the overall measurement process with the involved flow paths.

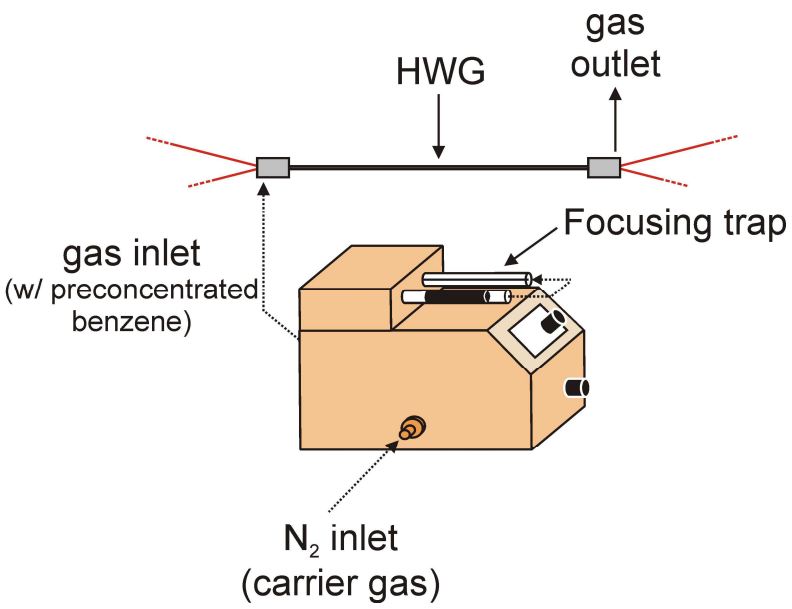

Figure 3-4: Diagram of overall experimental setup with flow paths.

3.2.5 Field Sampling Procedure

Field samples were collected at various locations of an industrial site using a Gillian HFS 113A pre-calibrated high-flow sample pump (Gillian Instrument Corp., NJ, USA) drawing samples directly from environmental air collected into 25 L Tedlar bags (SKC, Eighty Four, PA, USA). A volume of ~ 6 L of air sample was then transferred from the

central 25 L bag into individual 10 L Tedlar bags. Blinded air samples were then extracted from one of the 10L Tedlar bags using the same preconcentration/thermal desorption procedure previously described for the laboratory calibration, and subsequently analyzed by the TD-FTIR-HWG trace gas sensor directly at the field site.

3.2.6 Comparison with Other Methods

Several instruments were operated in parallel to the TD-FTIR-HWG trace gas sensor during this field test, and comprised photoionization detectors (PID) - one of which was benzene-specific, a gas chromatograph with a flame ionization detector (GC-FID), a gas chromatograph with a photoionization detector (GC-FID), colorimetric detector tubes, and a gas chromatograph utilizing a photoionization/differential ion mobility spectrometer. The validation method used during these studies was GC-FID, with the analyses independently performed by ExxonMobil Biomedical Sciences, Inc., Annandale, NJ. The gas samples for validation were collected from the same Tedlar bags, as those analyzed by all other field methods, and were preconcentrated onto coconut charcoal tubes and subsequently desorbed with carbon disulfide.

3.3 Results and Discussion

3.3.1 Laboratory Calibration

A robust calibration for ppb BTX detection was established in the laboratory prior to the evaluation of field samples on site. Nine certified gas standards (Praxair, Baton Rouge, LA) for BTX with concentrations of 100, 500, and 1000 ppb in nitrogen were individually adsorbed onto graphitized carbon black, and subsequently thermally

desorbed into the FT-IR-HWG trace gas sensor. From optimization, a sorption/desorption protocol was designed, which was then also used during the field measurements.

Parts-per-billion BTX laboratory calibrations were established by integrating absorbance peaks from these gas standards providing verified and known concentrations. Absorbance spectra were obtained from releasing concentrated gas plumes into the HWG sensor. An exemplary time resolved plot of the benzene absorbance is shown in Figure 3-5.

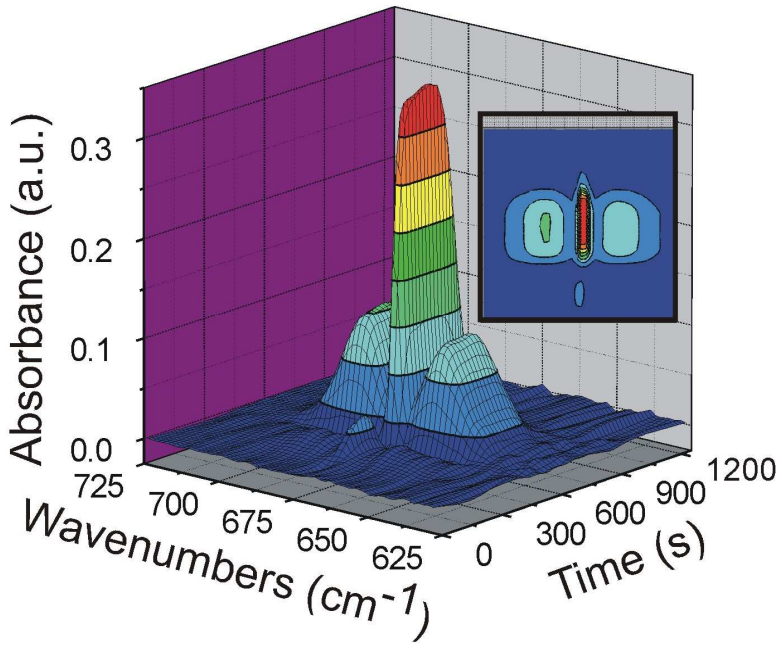

Figure 3-5: Absorbance of benzene measured inside the HWG with time. (Inset) Contour plot of the sensor regeneration.

The absorbance of toluene with time was also evaluated, as shown in Figure 3-6.

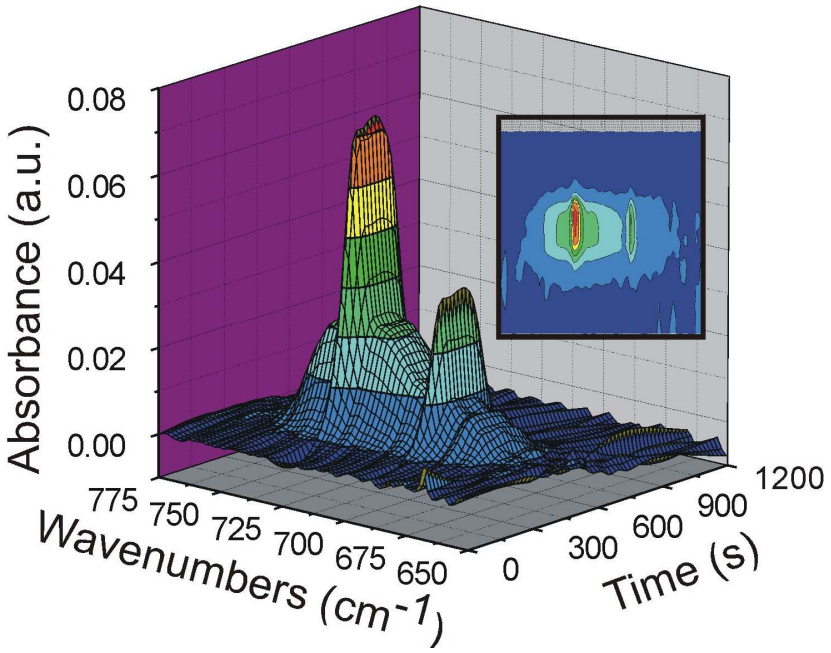

Figure 3-6: Absorbance of toluene measured inside the HWG with time. (Inset) Contour plot of the sensor regeneration.

Figure 3-7 presents the absorbance of all three xylene isomers as a function of time.

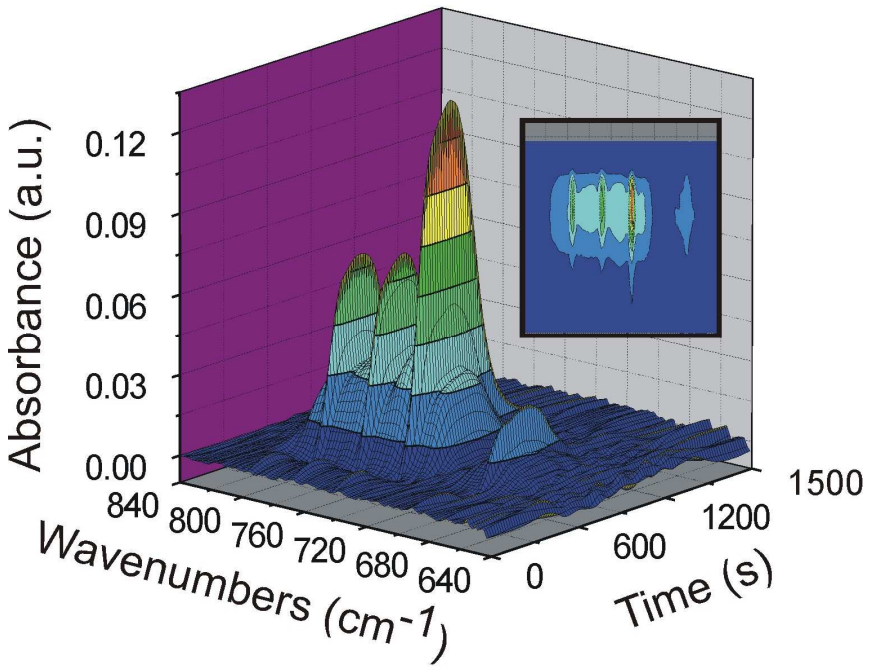

Figure 3-7: Absorbance of ortho, para, and meta-xylenes measured inside the HWG with time. (Inset) Contour plot of the sensor regeneration.

As evident in Figures 3-5, 3-6, and 3-7, the absorbance increases to a maximum and subsequently decreases with time representing the desorbed plume from the preconcentrater passing through the HWG gas cell. The resolution of this plume is largely dependent on the column flow, i.e. a fast column flow, fewer absorption peaks (because the analyte is flushed through the HWG faster), faster response time, and vice versa. In order to obtain precise and accurate calibrations, the column flow was decreased until multiple reproducible maximum peaks were generated, which were then integrated for obtaining quantitative data. Figure 3-8 further illustrates this concept.

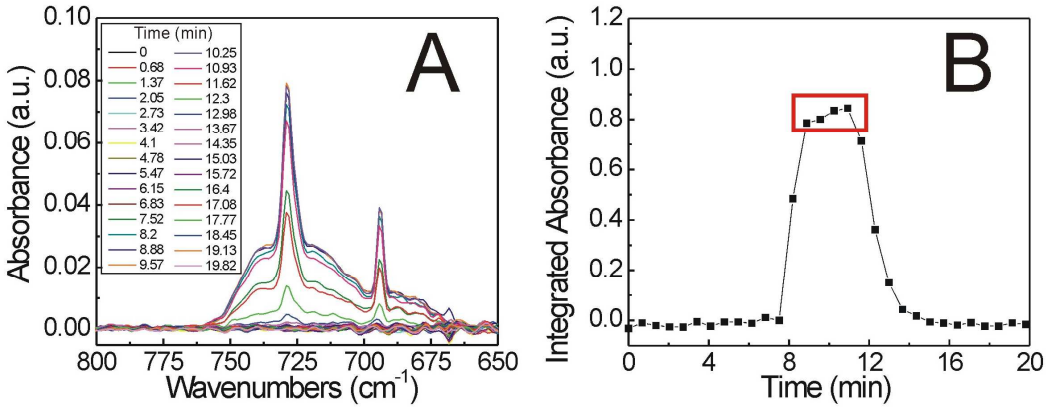

Figure 3-8: Spectra of 1000 ppb toluene absorbance (A) and integrated absorbance of the same spectra as a function of time (B). The red box denotes the several peak maxima selected for laboratory calibrations.

Here, Figure 3-8 A shows a raw data example of 1000 ppb toluene absorbance. The peak at 727 cm^{-1} was integrated and plotted as a function of time as illustrated in Figure 3-8 B. The red box shows the maximum integrated absorbance values used for laboratory calibrations.

Figure 3-9 A-C displays exemplary absorbance spectra for the BTX laboratory calibrations.

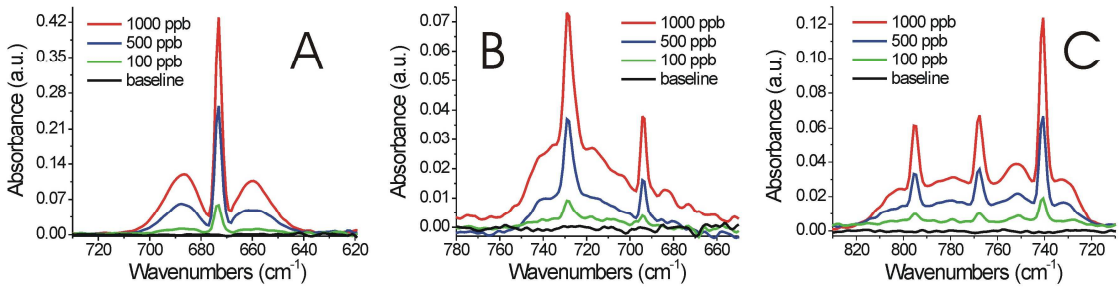

Figure 3-9: Laboratory calibration using absorbance spectra of benzene (A), toluene (B), and the xylenes (C).

As expected, the absorbance linearly increases with an increase in concentration in agreement with the Beer-Lambert law. The specific spectra shown here were the maximum absorbance spectra evident as the plume travels through the HWG. Figure 3-10 A-C graphically illustrate the corresponding calibration curves with a goodness of the fit (R^2) of 0.99297, 0.99716, 0.9942, 1.0000, and 0.9986 for benzene, toluene, and (o,m,p)-xylenes, respectively exhibiting excellent quantitative calibration models.

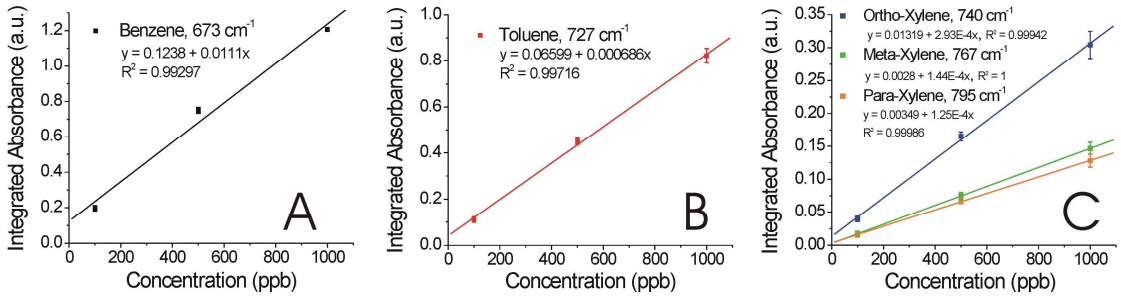

Figure 3-10: Laboratory calibrations for benzene (A), toluene (B), and the xylenes (C).

Absorbance values were obtained by integrating the maximum peak of IR spectra from 677.15 – 668.01 cm^{-1} for benzene, 762.97 – 705.30 cm^{-1} for toluene, 744.92 – 736.41 cm^{-1} for ortho-xylene, 771.41 – 762.24 cm^{-1} for meta-xylene, and 799.68 – 788.53 cm^{-1} for para-xylene. It should be noted that at the time of the field measurement campaign, only the laboratory calibration for benzene had been completed, as initially only quantification of this particular analyte was requested. Toluene and the xylenes were calibrated several months after the field measurement campaign again in the laboratory using the same FT-

IR HWG sensor set-up. These calibrations were then used derive concentration predictions post-field for toluene and the xylenes from the spectra collected during the field measurement campaign still providing excellent agreement with the validation results. These results further demonstrate the superior instrumental robustness of the developed FT-IR HWG sensing device.

3.3.2 Field Measurements

Upon completion of the laboratory calibration (for benzene), the instrument was taken out of the laboratory and into the field to an industrial location, where blinded environmental air samples were collected and analyzed over the course of one week. Prior to the daily data collection, a one-point calibration with a known gas standard (Air Liquide America Specialty Gases, Plumsteadville, PA, USA) was performed on site to validate that the current instrumental condition of the FT-IR HWG system in the field remains comparable to the previously established laboratory calibration, as shown in Figure 3-11.

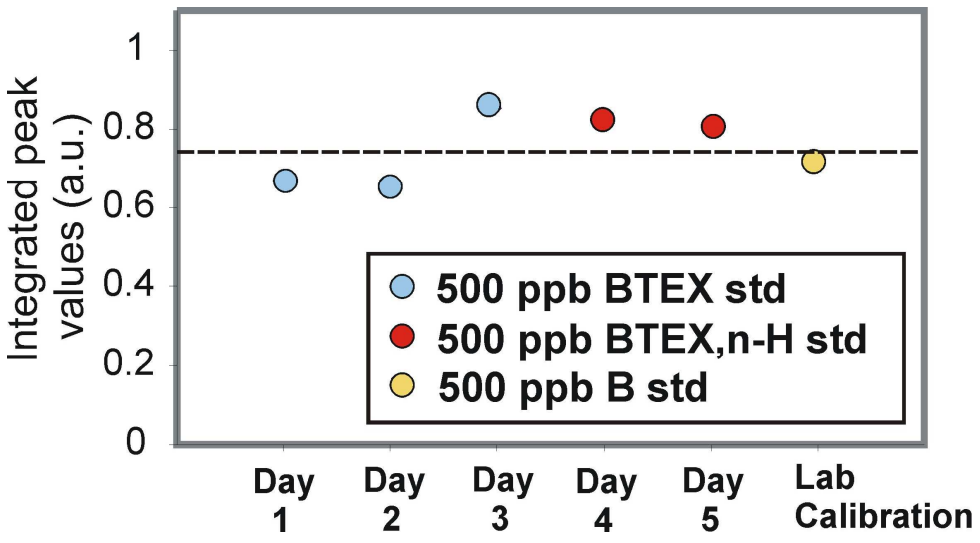

Figure 3-11: Daily one-point calibrations of benzene absorbance in field using certified gas standards. The dotted line represents the laboratory calibration level.

Environmental air samples were collected and analyzed immediately after the daily one-point calibration routine. Three individual bags per location number were analyzed to evaluate the variance. Figure 3-12 shows a typical IR spectrum of a field air sample indicating the relevant absorbances for BTX.

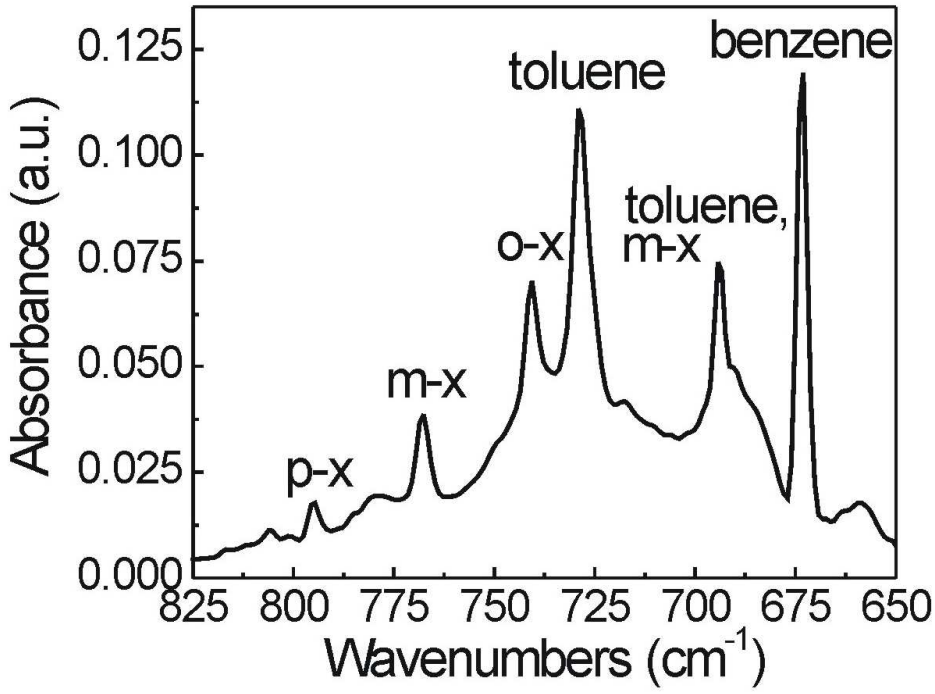

Figure 3-12: Typical absorbance spectrum of an environmental air sample.

It is evident that all five expected analytes are present with distinct Q-branch absorbance peaks centered at 674 cm^{-1}, 727 cm^{-1}, 740 cm^{-1}, 767 cm^{-1}, and 795 cm^{-1} for benzene, toluene, and (o,m,p)-xylenes, respectively in the mid-infrared fingerprint region.

GC-FID was used to validate the method reported here by analyzing the same field samples after the field measurement campaign. Figure 3-13 compares the difference between the GC-FID validation results, and the TD-FTIR-HWG trace gas sensor analyses.

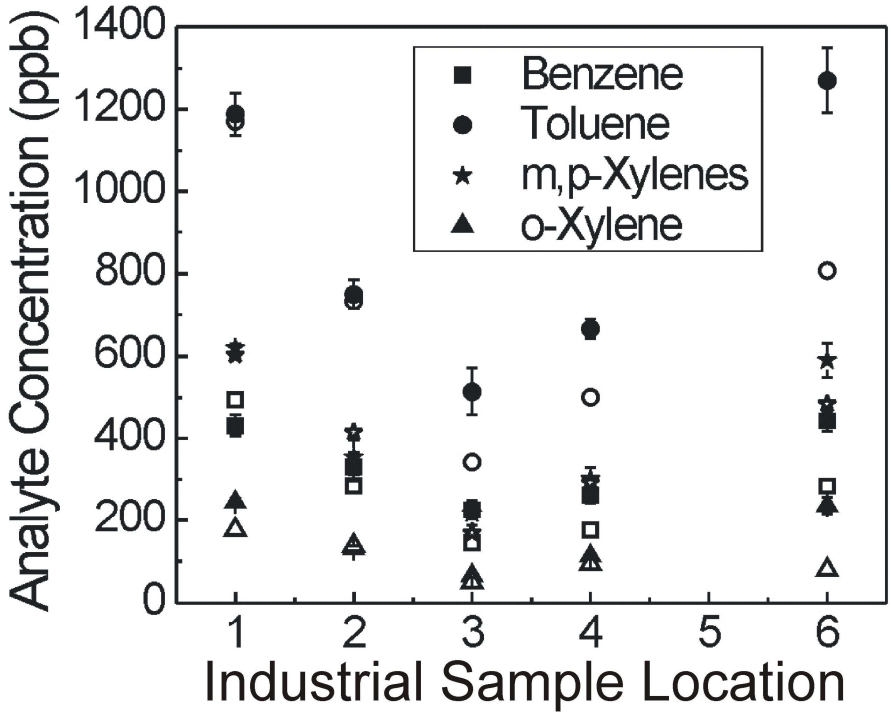

Figure 3-13: Direct comparison of TD-FT-IR-HWG results with GC-FID validation. Solid points represent TD-FT-IR-HWG data, and outlined points represent GC-FID data.

It should be noted that among all the instruments compared in this field study, only the TD-FTIR-HWG trace gas sensor was able to successfully quantitatively discriminate all three isomers of xylene, whereas all GC techniques could not distinguish between meta-xylene and para-xylene conformations. As such, in Figure 3-13, the predicted

concentrations for meta and para-xylene isomers were added enabling a direct comparison with the GC technique.

Toluene appears to consistently provide higher values than the validation method suggests, particularly for location six; this is thought to be due to peak overlap and spectral contributions from other analytes in the mixture such as meta-xylene and ethylbenzene, with the latter not included in the calibrations. Here, using multivariate calibration in lieu of univariate calibration is expected to significantly improve the accuracy of the toluene concentration prediction by discriminating spectral contributions of toluene from those of other hydrocarbons.

It should also be noted that data from location 5 was excluded from the values reported here. This sample has revealed significantly higher variation between the different analysis techniques used during this field study compared to any of the other samples in the high ppb range. Furthermore, samples from location 5 for the GC-FID validation were prepared and analyzed the day after the sample bag was collected. Hence, it is likely that an operator error may have led to a wrong bag being used for these analyses resulting in the larger range for the reported concentrations of this particular sample. A Grubb's test at the 5% significance level on the range between sample averages for the various techniques for the first six samples indicates that on this basis analyses from location 5 may reasonably be rejected ($G\ 1.697 > 1.580$, $\alpha = 5\%$) as an outlier within this data set; later, data for toluene and meta-, para-xylenes confirmed the Grubb's Test results

performed for benzene for location 5. Therefore, this location was not considered a representative data set for any of the tested field techniques.

Figure 3-14 describes the analyte prediction capability of the TD-FTIR-HWG trace gas sensors in comparison with other instrumental techniques, which were simultaneously operated for analyzing the same field samples.

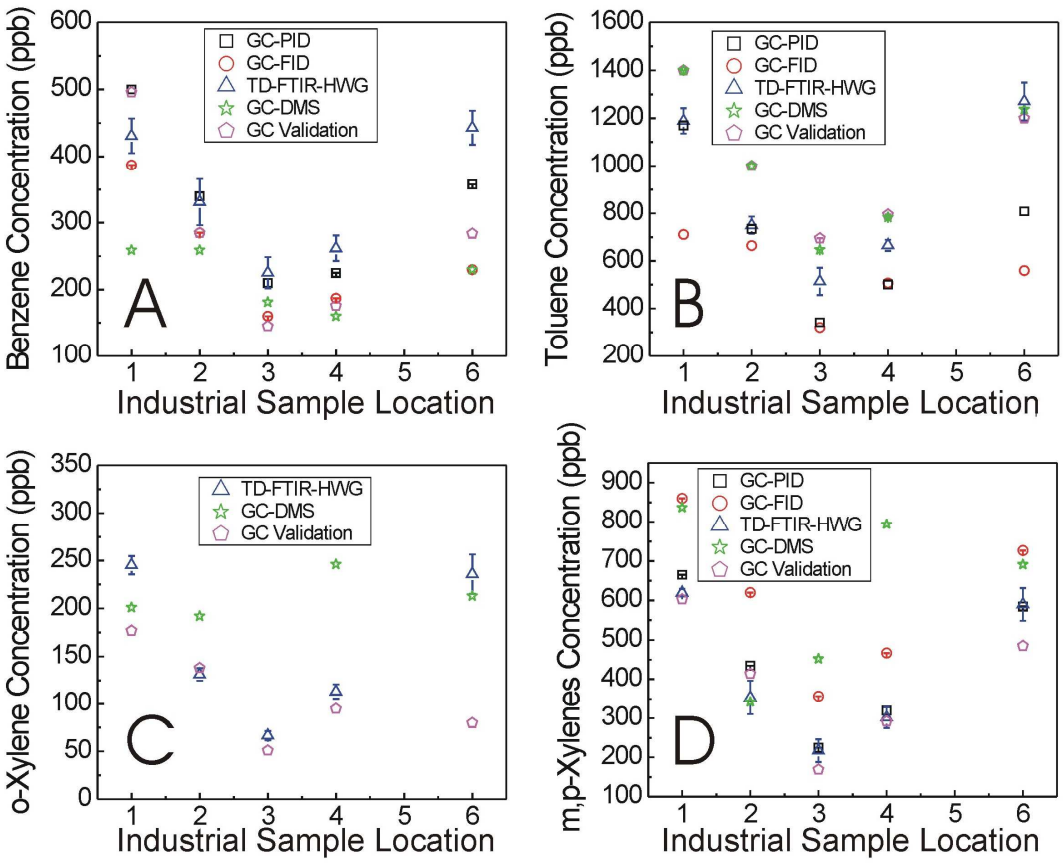

Figure 3-14: Analyte prediction capability of all techniques which simultaneously analyzed the same environment air samples in field for benzene (A), toluene (B), ortho-xylene, and (C), and meta,para-xylenes (D).

With the exception of location 6, the TD-FTIR-HWG predicted the present analyte concentrations within close proximity to results derived from the validation method, which were also comparable to or better than the currently used commercially available devices. In summary, these results clearly suggest that mid-infrared spectroscopy - as exemplified here with the developed FT-IR HWG trace gas sensors - is a viable and comparable technique for selective ppb detection of BTX in complex environmental matrices usable during in-field studies.

3.4 Optimization of the Experimental Parameters

The sampling parameters presented in this chapter were specifically tailored to be compatible with the field trial requirements, which had to be based on a unified procedure for all tested techniques. However, this may not imply that the best performance conditions for individual devices were met. Hence, in a separate study the preconcentration parameters for the TD-FT-IR-WHG system were further investigated, in particular for achieving lower detection limits for benzene.

3.4.1 Preconcentration Time

The most relevant experimental parameter that can be optimized for this purpose is the preconcentration time. In the studies described herein, a preconcentration time of seven minutes was used to yield a signal-to-noise ratio consistently well above the limit of quantification (6σ). However, an important figure of merit is to reduce the time it takes for sample pretreatment steps, which in turn reduces the overall sensor response time. Figure 3-15 portrays the integrated absorbance of 100 ppb benzene at varying preconcentration times.

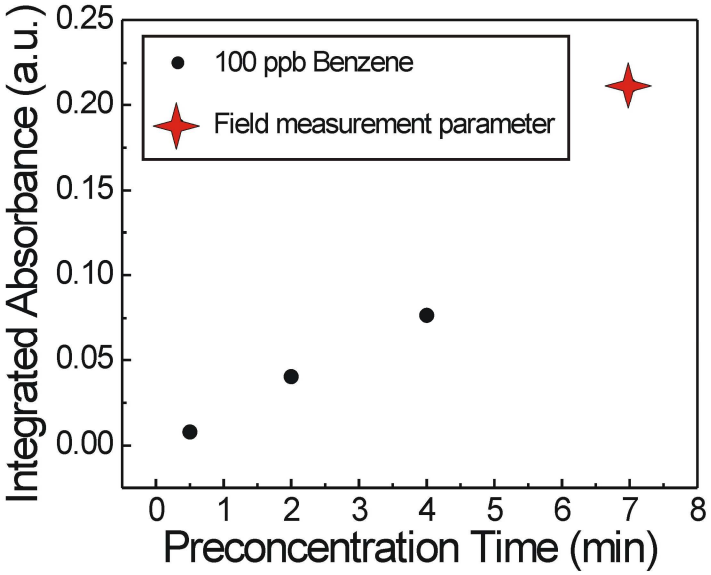

Figure 3-15: The integrated absorbance of 100 ppb benzene over a range of preconcentration times.

From Figure 3-15 it is conceivable that the time it takes for preconcentrating a field sample, and thus the actual sample volumes, could be reduced below a couple of minutes. For direct comparison, these gas samples were acquired with the sample pump flow as applied during the field measurements, i.e. 162 mL/min.

3.4.2 Plume Resolution

Analyte(s) that were preconcentrated onto the sorbent tube are released into the hollow waveguide over time by heating and desorption into a carrier gas flow. The temperature required to thermally desorb the analytes is inherent to the sorbent material itself; thus, as long as the temperature is at or above this requirement, this is not a parameter than would yield significantly improved results. However, the carrier gas flow controls how fast or

slow the concentrated gas plug is released into the gas cell, i.e. the hollow waveguide. As previously mentioned, the resolution of this plume is largely a function of the carrier gas flow rate through the trap, i.e. the column flow. The maximum integrated absorbance as a function of varying column flows is shown in Figure 3-16.

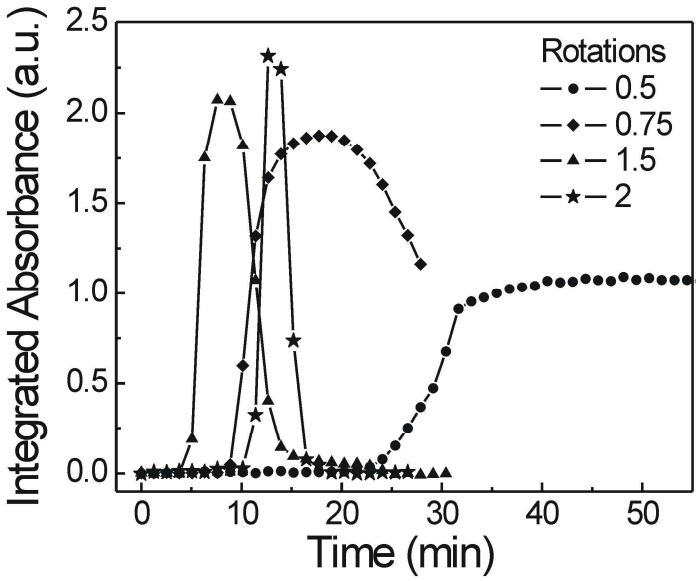

Figure 3-16: Integrated absorbance of 50 ppm benzene as a function of time at various column flows.

A relatively slow column flow results in many reproducible absorbance peak maxima (for more information, refer to Figure 3-8), which yield precise measurements with low 'within tube' and 'tube to tube' variance; however, the time elapsed between column flow start and the time until maximum absorbance is achieved can be significantly extended up to 30 minutes or more. On the other hand, a fast column flow releases the analyte(s) into the hollow waveguide relatively quickly, thereby resulting in a few absorbance peaks where the maximum absorbance may not be clearly determined. For

the work presented herein, the column flow was optimized to determine the lowest response time achievable given at least three reproducible absorbance peak maxima are present with low standard deviation.

It should be noted that the thermal desorption unit used here utilized a manual flow controller for adjusting the column flow. The values given for the flow settings in Figure 3-16 are analog rotary valve settings for the adjustment of column flow and represent a systematic way to reproducibly set the column flow. The actual flow of the carrier gas through the trap and into the hollow waveguide was approximately within the range of 0 > 2 mL/min, which is too low for analyzing with statistical certainty using the tools at hand. Future work should be focused on utilizing an automated mass flow controller with a dynamic range of a few milliliters for more precise control on the plume resolution.

3.4.3 Lower Detection Limits

In a final step, spectral resolution and column flow (plume resolution) were optimized to effectively measure benzene concentrations of 5 ppb with integrated absorbance reproducibly above the limit of quantification. Figure 3-17 presents an absorbance spectrum of 5 ppb benzene in comparison to 100 and 500 ppb.

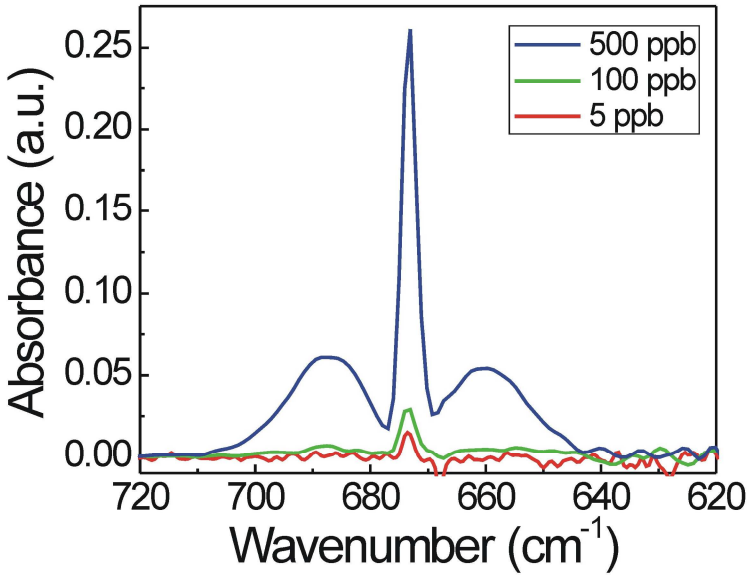

Figure 3-17: 500 ppb benzene at 2 cm^{-1} resolution (Blue), 100 ppb benzene at 2 cm^{-1} resolution (Green), and 5 ppb benzene at 1 cm^{-1} resolution (Red).

Measurements of 500 and 100 ppb benzene were collected at the previously described measurement conditions of 2 cm^{-1} spectral resolution and by averaging 100 spectra scans yielding a response time of 42 seconds. Measurements of 5 ppb benzene were achieved by optimizing the spectral resolution to 1 cm^{-1} averaging 50 spectra scans yielding a comparable response time of 43 seconds. To obtain a statistically significant signal-to-noise ratio, the preconcentration time was increased to 40 minutes using the same pump flowrate (162 mL/min) as previously applied during the field measurements.

Additionally, it was shown that preconcentration volumes ranging from 0.2 L to 100 L for BTX at 50 mL/min with a desorption temperature of 330 degrees Celsius result in recovery rates exceeding 80%[5]. This evidence further suggests that large volumes of low concentration (ppb to ppt) gas phase BTX may be reproducibly preconcentrated over time

to significantly improve the signal-to-noise ratio prior to reaching the breakthrough volume limitation, thereby possibly allowing for parts-per-trillion (ppt) sensitivity with TD-FT-IR-HWG sensors.

3.5 Summary and Outlook

The FT-IR HWG method used here demonstrates the capability of mid-infrared spectroscopy as a compact, portable, and powerful sensing tool to quantify and discriminate ppb level structurally related constituents (BTX) within real-world environmental air samples in the field based on robust laboratory calibrations. This technique compares well both with the validation method (GC-FID), as well as off-the-shelf industrial hygiene methods and industrial prototypes. The experimental parameters used here were adjusted to meet unified field trial requirements for all tested sensing techniques; however, it was shown that parameters such as preconcentration time, column flow, and spectral resolution may be further optimized for yielding shorter response times and lower detection limits (low ppb) with the developed TD-FT-IR-HWG sensor system.

The industrial hygiene devices compared here were in part hand-held, whereas the TD-FTIR-HWG described herein was portable, yet exhibited a bench-top style footprint. It is anticipated that with the advent of quantum cascade lasers emitting at the long wavelength fingerprint region of the mid-infrared spectrum required for BTX detection will improve both sensitivity and selectivity (further discussed in Chapter 7) of IR devices in a hand-held format. Consequently, limits of detection reaching the low ppb or

high ppt concentration range without preconcentration may be achievable. Given the enhanced spectral density provided by QCLs efficiently overlapping the absorbance feature of the analyte by appropriate emission wavelength tuning may in future provide maximum absorbance with inherent molecular selectivity for the detection of individual analytes within complex environmental mixtures, as already demonstrated for QCL-HWG trace gas sensors designed by our research group for other analytes.[6-8]

References

[1]D.M. Young, and A.D. Crowell, Physical Adsorption of Gases, Butterworths, Washington, 1962.

[2]F. Bruner, P. Ciccioli, and F. Di Nardo, Use of graphitized carbon black in environmental analysis. Journal of chromatography 99 (1974) 661.

[3]F. Bruner, G. Crescentini, and F. Mangani, Graphitized carbon black: A unique adsorbent for gas chromatography and related techniques. Chromatographia 30 (1990) 565-572.

[4]O.A. Pogodina, V.V. Pustogov, F. de Melas, C. Haberhauer-Troyer, E. Rosenberg, H. Puxbaum, A. Inberg, N. Croitoru, and B. Mizaikoff, Combination of sorption tube sampling and thermal desorption with hollow waveguide FT-IR spectroscopy for atmospheric trace gas analysis: determination of atmospheric ethene at the lower ppb level. Analytical Chemistry 76 (2004) 464-468.

[5]J. Brown, and B. Shirley, A Tool for Selecting an Adsorbent for Thermal Desorption Applications, Supelco, Bellafonte, 2001.

[6]C. Charlton, F. de Melas, A. Inberg, N. Croitoru, and B. Mizaikoff, Hollow-waveguide gas sensing with room-temperature quantum cascade lasers. IEE Proceedings: Optoelectronics 150 (2003) 306-309.

[7]C. Charlton, B. Temelkuran, G. Dellemann, and B. Mizaikoff, Midinfrared sensors meet nanotechnology: Trace gas sensing with quantum cascade lasers inside photonic band-gap hollow waveguides. Applied Physics Letters 86 (2005) 194102/1-194102/3.

[8]C. Young, S.-S. Kim, Y. Luzinova, M. Weida, D. Arnone, E. Takeuchi, T. Day, and B. Mizaikoff, External cavity widely tunable quantum cascade laser based hollow waveguide gas sensors for multianalyte detection. Sensors & Actuators: B. Chemical 140 (2009) 24-28.

CHAPTER 4

FUNDAMENTALS OF QUANTUM CASCADE LASERS AND THEIR ROLE IN TRACE GAS SENSORS

In this chapter, the fundamentals of quantum cascade lasers (QCL) will be covered in detail, demonstrating their potential as light source in next-generation miniaturized trace gas sensors. QCLs will also be contrasted against other state-of-the-art mid-infrared laser sources, as well as conventional broadband sources used in FT-IR spectrometers. State-of-the-art in QCL based trace gas sensors will also be discussed for providing an enhanced understanding on chemical sensing methods that have been researched in the past decade as a preface for the QCL based sensor research presented in the following chapters.

4.1 Motivation

Chemical sensing at MIR (5000–500 cm^{-1}, 2–20 μm) frequencies requires appropriate radiation sources covering the entire spectral regime. Conventional radiation sources in the MIR range utilize blackbody emission characteristics are limited to emitting incoherent radiation. Most importantly, the energy density per spectral band is limited, as the emitted radiative energy is distributed across a broadband emission spectrum. Consequently, during molecular analysis utilizing, for example, MIR absorption spectroscopy, most of the emitted radiation in fact does not effectively overlap with the characteristic absorptions of analyte molecule(s), with the exception of the frequencies

where resonant energy transfer gives rise to vibrational or rotational transitions resulting in distinct molecular signatures providing a pattern of absorption features.

Since the advent of laser technology, scientists and engineers in spectroscopy and sensor technology have increasingly adopted laser radiation sources due to their emissive power concentrated into a very narrow spectral band, thereby providing a high spectral density per spectral band unit. In addition, lasers emit coherent radiation, thereby enabling phase sensitive measurements[1].

4.2 State-of-the-Art in Mid-Infrared Light Sources for Trace Gas Sensing

4.2.1 Gas Lasers, Lead Salt Laser Diodes, DFGs, and OPOs

The carbon dioxide (CO_2) gas laser developed by Patel at Bell Laboratories in 1964[2, 3] is among the most commonly applied laser light sources in the MIR regime. The lasing wavelength is tunable between 1087 and 926 cm^{-1} (9.2 and 10.8 μm), and emission powers up to few tens of kilowatts are provided. The carbon monoxide (CO) laser is another commonly applied gas laser in the MIR range covering a wavelength range of 2000 – 1667 cm^{-1} (5 – 6 μm); utilizing overtone vibrations, the lasing wavelength can be extended up to 3704 cm^{-1} (2.7 μm)[4].

Although gas lasers provide an excellent MIR radiation source for absorption spectroscopy, they have a few drawbacks such as complexity of operation, usually bulky dimensions, limited wavelength bandwidth for molecular spectroscopy, and rather high initial investments, which limit their application predominantly to laboratory benchtop

usage. To implement more portable, field-deployable optical chemical sensors, it is essential to miniaturize the entire sensing system comprising the MIR radiation source, the light delivery system (i.e. optics), a wavelength selection device (if needed, e.g. in case of a broadband IR source), and an appropriate detector. Hence, miniaturizing the MIR radiation source without losing the merits of laser technology is of crucial importance, and has lead to substantial research in the field of semiconductor laser technology for MIR frequencies, which promises compact coherent MIR radiation sources at acceptable cost.

As a result, significant research efforts have been dedicated to finding adequate semiconductor materials with an energy bandgap separation narrow enough to facilitate emission of photons at MIR wavelengths. Various lead salt materials are used for direct bandgap laser diodes, in which electrons from the conduction band recombine with holes from valence band, thereby emitting coherent photons. This type of semiconductor laser is called a p–n junction diode laser, and the lead salt material group includes binary mixtures such as PbTe, PbSe, PbS, SnSe, SnTe, and CdS, and ternary materials such as $Pb_{1-x}Sn_xTe$, $Pb_{1-x}Sn_xSe$, and variations thereof. Although lead salt laser diodes emit MIR radiation with certain gaps in the region 3333 – 333 cm^{-1} (3 – 30 μm), their application is somewhat limited by the need for cryogenic cooling (15 – 80 K), especially if appreciable emission powers are required; in general, comparatively low-power output, limited manufacturing consistency of the lasing heterostructure, design of the emission wavelength only by the material composition, and lack of suitable laser materials in certain regions of the MIR spectrum.

Next to semiconductor lasers, alternative light source concepts providing coherent MIR radiation have been studied focusing particularly on nonlinear optical effects such as DFG (difference frequency generation) and OPO (optical parametric oscillation). Both techniques do not inherently generate MIR radiation, but up-convert the wavelength of the fundamental pump laser beam, usually based on Vis/NIR (visible or near infrared) emission sources, into MIR radiation via nonlinear optical processes. Optical crystals without structural inversion symmetry may generate electromagnetic radiation (ω_1, idler) from a pump beam (ω_3, pump) with or without another input beam (ω_2, signal) via second-order nonlinear optical coefficients, $\chi^{(2)}$, which are techniques referred to as DFG (with ω_2 external input) and OPO (without ω_2 external input), respectively. Examples of typical nonlinear optical crystals are $AgGaS_2$, $AgGaSe_2$, GaSe, $LiNbO_3$, $LiTaO_3$, and potassium titanyl phosphate (KTP). The relationship among the three waves follows energy conservation and momentum conservation with frequency down-conversion taking advantage of mature and well-established Vis/NIR laser sources providing sufficient output power, beam quality, etc., thereby generating coherent MIR radiation. Despite the benefits of such down-conversion schemes, the rather complicated phase matching process imposed by momentum conservation, the dimensions of the optical setup, and the achievable output powers favor compact MIR laser light sources for optical sensing and in-field application scenarios[1].

4.2.2 Quantum Cascade Lasers (QCLs)

One of the most relevant technical advances in MIR light source technology has been the design and realization of the QCL. QCLs were first conceptualized by Kazarinov and Suris[5], and experimentally realized for the first time in 1994 by a team of researchers at Bell Laboratories[6]. QCLs give rise to light emission on the basis of fundamentally different principles, as compared to other semiconductor laser diodes. Most semiconductor laser diodes emit photons by radiative recombination of electrons from conduction bands and holes from valence bands. QCLs emit photons while electrons in the conduction band are transported through cascading small 'energy ladders', a process known as intersubband transitions. These small 'energy ladders' are called *subbands*, and are supported by quantum wells.

For chemical sensing applications, QCLs have several advantages over lead salt diode lasers and other conventional MIR laser sources. QCLs can be engineered to emit radiation anywhere between 2857 and 417 cm^{-1} (3.5 – 24 μm) (MIR), and even beyond into the THz (terahertz) frequency regime. They inherently provide more optical output power than lead salt laser diodes, for example, a peak power of 0.6 W at room temperature has been reported for a QCL with 100 stages of active regions in pulsed operation[7]. Furthermore, the threshold current of QCLs is considered less sensitive to temperature in contrast to conventional diode lasers. Finally. the QCL chip is miniaturized (typically ~ 2 mm), thereby providing an ideal basis for next-generation chip-integrated QCL-based sensing platforms.

As a result, merely a decade after their practical introduction, QCLs are acknowledged as the most advanced MIR light sources with particular relevance for chemical sensing applications.

4.2.3 Comparison of QCLs with FT-IR

The conventional light source used for mid-infrared spectroscopy of trace gases is the Fourier-transform infrared spectrometer (FT-IR). The reader is referred to Chapters 1-3 for further introductory information on FT-IR spectrometers for trace gas sensing.

One of the requirements of a light source for integration into hand-held trace gas sensors is the potential for miniaturization. Currently, FT-IR spectrometers are still bulky with a benchtop sized footprint, while QCLs are much more compact, generally already packaged into a hand-held format. As an example for the most compact formats of either technology (to date), two commercially available devices as used in our laboratory are presented in Figure 4-1.

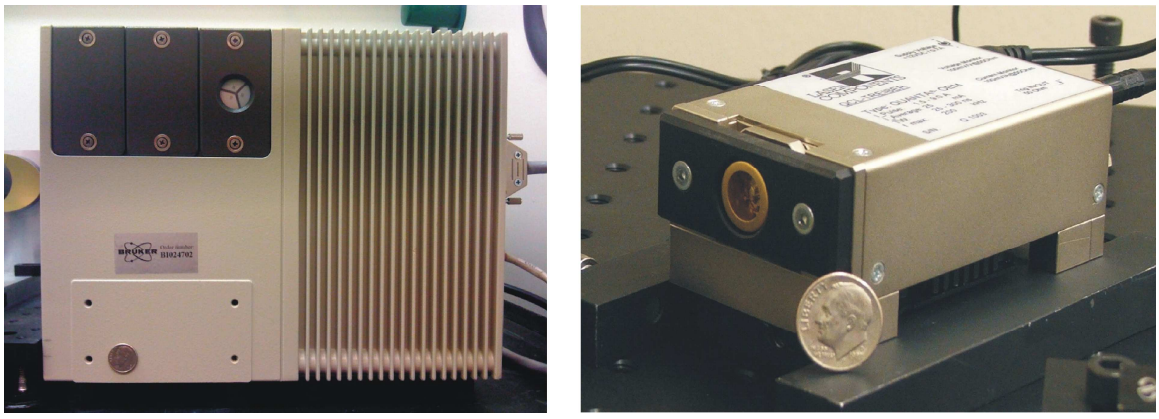

Figure 4-1: Bruker Matrix-M portable FT-IR spectrometer (left), and Laser Components, Inc. QCL (right). A dime is presented in each photo to show the scale.

It should be noted that the QCL shown in Figure 4-1 contains the appropriate protective and commercial housing, and the driver electronics for the device to operate within the shown package; the laser itself is of much smaller footprint and contained in the TO-package visible on the front (golden ring) sealed off with an IR-transparent window.

Besides the need for the light source to be compact, power consumption is an additional figure-of-merit to consider, particularly for trace gas sensors, which should be portable, wearable, or used for on-site continuous stand-alone monitoring such as in an industrial setting. The power consumption for a portable, yet still bulky FT-IR spectrometer can be as high as 140 W, whereas miniaturized, hand-held devices such as QCLs typically consume 28 times less power, i.e. only 1.5–5 W[8, 9].

While QCLs are compact and consume less power, FT-IR spectrometers still have a significant advantage over a laser light source inherent to broadband radiation, i.e. that multiple analytes can be simultaneously determined. The inherent nature (narrow linewidth) of a laser light source typically allows for the detection of only one or very few analytes within this narrow spectral band. However, widely tunable QCLs are rapidly emerging as a viable option for frequency tunable, hand-held, sensitive, and selective trace gas sensors[9], as discussed in the next chapter.

4.3 Fundamentals of Quantum Cascade Lasers

4.3.1 Brief Theory on Quantum Mechanics

To understand the unique features provided by QCLs, the operation principles of conventional bandgap laser diodes such as lead salt lasers are briefly summarized. The lasing principle of these diodes is based on radiative recombination of electrons from the conduction band, and holes from the valence band. As an example, the operation principle of a double heterostructure laser diode (GaAs/AlGaAs) is shown in Figure 4-2A.

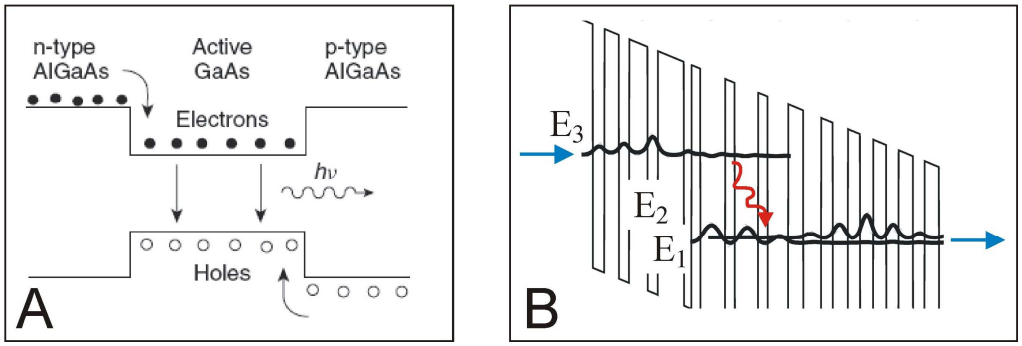

Figure 4-2: Different photon generation schemes of conventional laser diodes (A), and of QCLs (B).

If electrons from the conduction band of the GaAs active region combine with holes from the valence band, photons with energies compatible to the bandgap are generated. In this case, the wavelength of the emitted radiation is governed by the energy bandgap of the material, and therefore represents an intrinsic material property; hence, designing the laser emission frequency requires changing the composition of the alloy.

As previously mentioned, the most distinctive feature of the QCL is the unique photon generation scheme providing several advantages over conventional semiconductor laser diodes. In a simplified view, QCLs emit photons by optical transition of electrons within the conduction band without the contribution of holes in the valence band. QCLs provide a staircase-like energy state arrangement such that - ideally - photons are generated whenever electrons transit down to the next energy state. The essential operation scheme of a QCL is shown in Figure 4-2B representing the conduction band structure of two active regions separated by an injection region. QCLs have more than one active region for harvesting a series of photons per electron, which may range from few tens to hundreds of steps ('cascade'). Each active region comprises three or more coupled quantum wells to form electron eigenstates, i.e. so-called 'subbands'. As an example, the quantum wells in the active regions are made of GaInAs with AlInAs barriers, which are lattice-matched to an InP substrate. Alternatively, the quantum wells and the barrier layers can either be made of GaAs and AlGaAs or other suitable materials[10]. The active region has three electron eigenstates labeled E_3, E_2 and E_1, as shown in Figure 4-2B. Electrons in E_3 transit down to level E_2, thereby releasing photons, and eventually thermalize to level E_1 in a non-radiative process. Finally, electrons in level 1 of the active region tunnel through the potential barrier wall of the injector region, and are available for the next 'cascade' to produce another coherent photon. The conduction band structure of the injection region consists of multiple coupled quantum wells, i.e. the so-called 'superlattices (SLs)' forming very closely spaced electron eigenstates or so-called 'minibands'. Once electrons from the previous active region enter the injection region, they non-radiatively relax down to the energetically lower region of the miniband, which

is well aligned to the E_3 state of the next active region. The role of the injection region is of critical importance to achieve population inversion, which is a necessary condition for lasing, and to assure cascading photon generation by bridging neighboring active regions. Despite the ultrafast carrier relaxation mechanism within one band, population inversion between E_3 and E_2 may be achieved by deliberate band structure engineering. The quantum well and the barrier structures are carefully designed to optimize subband energy levels, carrier scattering rate, optical dipole coupling strength, tunneling time, etc., for achieving population inversion. In contrast to conventional heterostructure laser materials, bandstructure engineering enables the lasing frequency of QCLs to be tuned anywhere throughout the entire MIR range by designing the properties of the appropriate quantum wells, rather than changing the material composition. Each active region of a QCL usually has an identical structure, and the total number of cascades can be easily scaled up to more than one hundred stages[11]. Since efficient compact high-power laser sources in the field of MIR sensing have been in high demand for a considerable period of time, QCLs complement a long-term need in the optical sensing community.

4.3.2 Lasing Cavity Structures: Multimode and Single-Mode

The simplest resonant cavities for semiconductor lasers are cleaved FP (Fabry–Perot) cavities. Therefore, FP-QCLs typically provide multimode lasing spectra. High-reflectivity coatings at the end facets of the cavity may improve the optical quality of the lasing structure. Usually, such lasers exhibit several lasing peaks, as the free spectral range of the neighboring resonant peaks is inversely proportional to the cavity length. Typically, FP lasers of practically relevant length will be characterized by multiple

resonant peaks within the gain curve, thereby supporting longitudinal multimode operation. Although FP-QCLs are suitable for covering comparatively broad absorptions in condensed phases, they prove less practical for trace gas sensing applications. Usually, gas phase molecules are characterized by very sharp MIR absorption peaks resulting from additional rotational transitions, which are difficult to address individually given the emission characteristics of FP-QCLs. Consequently, decreased sensitivity and selectivity are expected in MIR gas phase absorption spectroscopy due to the multimode nature of the emitted radiation.

To help overcome this challenge, single-mode operation was enabled with the introduction of the first DFB (distributed feedback) QCL in 1997[12-14]. DFB structures in QCLs have proven successful for powerful longitudinal single-mode operation, as previously demonstrated for NIR telecommunications wavelengths.

Although single-mode QCLs with fixed lasing wavelengths are convenient light sources, application limitations exist for simultaneously addressing multiple analytes. Therefore, ideal MIR light sources for molecular sensing applications should comprise all the merits inherent to DFB-QCLs, while providing broadband tunability.

4.4 State-of-the-Art in QCL based Trace Gas Sensors

A selection of relevant QCL-based gas sensing methods are described in detail following an in-depth literature review, and are illustrated using relevant application examples. QCL-based gas sensors consist of three main components: (i) the QCL light source, (ii)

the gas cell, and (iii) the detector. Limits of detection usually range from molecular concentration levels at parts per million (ppm) to parts per trillion (ppt), therefore rendering these types of gas sensors particularly useful for gas sensing applications at trace levels including but not limited to e.g. breath diagnostics and environmental monitoring.

4.4.1 QCL Gas sensing using Direct Absorption

Quantitative optical sensing schemes utilizing QCLs as the MIR light source in direct absorption measurement scenarios follow the Lambert–Beer law as discussed in Chapter 1. Molecules present within the optical beam selectively absorb radiation at specific frequencies, if the conditions for resonant energy transfer of photon energy to discrete vibrational or rotational molecular transitions are provided. A typical gas cell with defined optical pathlength applied for direct absorption measurements either contains a discrete sample of interest or facilitates a continuous gas flow through the measurement cell. As these cells do not provide reflective surfaces extending the optical path length 'l' in the Lambert-Beer law equation usually corresponds to the physical length of the gas cell where photons interact with gas phase molecules. The usually rather short optical path length for minimizing the dimensions of the gas cell and the required volume of gaseous sample result in low sensitivities as compared to other techniques discussed hereafter. A conventional experimental setup for gas sensing via direct absorption using a QCL as the radiation source is schematically shown in Figure 4-3.

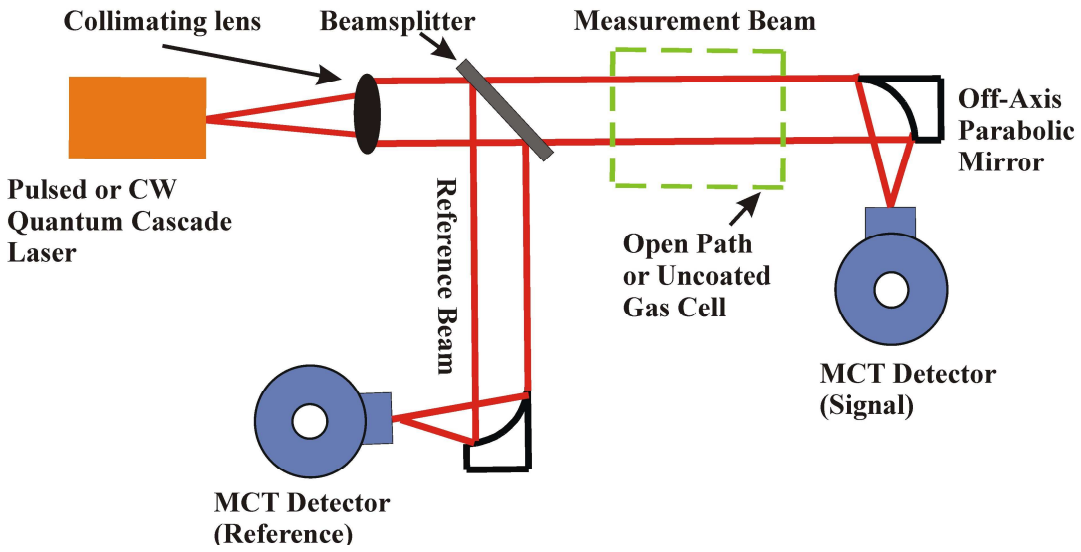

Figure 4-3: Exemplary setup for a QCL based direct absorption gas sensor. The measurement beam uses an open path or an uncoated gas cell to pass through radiation, which is selectively absorbed by analyte molecules. Occasionally, a reference beam is used with the measurement beam and reference bean divided using a beamsplitter, and the reference signal focused onto a reference detector. The reference beam may also contain the same type of cell as the measurement beam with or without a known concentration of the analyte or only containing the background matrix.

For consistency throughout this chapter, all schematics of QCL-based sensor concepts use following color code: orange = QCL, red = radiation path, black = optics for light guiding, green = sample compartment, and blue = detector. Despite the lack of sensitivity, direct absorption measurements with QCLs have found application in sensing/monitoring situations at appropriate concentration levels, where additional optical elements for e.g., folding the optical path for extending the absorption path length is not possible or feasible such as monitoring gaseous constituents within exhaust streams. Wysocki et al. have developed a pulsed QCL-based gas sensor capable of parts-

per-billion (ppb) detection of nitric oxide, carbon dioxide (CO_2), water (H_2O) and ammonia (NH_3) with the same laser by current tuning at comparatively harsh conditions that would potentially be harmful to additional optical elements within the measurement region. In situ monitoring of nitric oxide (NO) in industrial exhaust systems produced a noise-equivalent sensitivity (1σ) of approximately 100 and 200 ppbmHz$^{-1/2}$ at room temperature and at 630 K, respectively[15]. Combustor exhaust streams were also probed by using a pulsed QCL-based gas sensor with nearly 1 meter of optical path length in response to increasing concerns on negative effects of sulfur oxides on the ambient atmosphere. Continuous detection of sulfur dioxide (SO_2) and sulfur trioxide (SO_3) was achieved to a limit of approximately 1–2 ppmvmHz$^{-1/2}$ at 300 torr and at elevated temperatures ranging from 300 to 700 K[16].

Direct absorption with continuous wave (cw) QCLs was applied for the detection of ammonia (NH_3) down to a noise-equivalent sensitivity of 18 ppm with an optical path length of 1 m. The detection limit was further improved by a factor of three down to a normalized noise-equivalent sensitivity of 82 ppbmHz$^{-1/2}$ by using second-harmonic-detection wavelength-modulation spectroscopy[17].

Although the optical layout for direct absorption sensing with QCLs is simplified compared to other techniques, the detection limit suffers owing to the usually short optical path lengths that are frequently determined by the dimensions of, for example, an exhaust port. Consequently, the sensitivity of direct absorption measurements could be

improved by one order of magnitude or more utilizing an increased optical path length achieved via multiple reflections or beam folding, as discussed in the next sections.

4.4.2 QCL Gas sensing using Multipass Gas Cells

One strategy to improve the sensitivity using QCL-based gas sensors is the application of multipass gas cells, which use two or more mirrors to fold the beam multiple times. Thus, extended optical path length improves the signal-to-noise ratio until mirror reflection losses compensate for the achievable benefit[18] or interference fringes generated by multiple reflections counteract the signal improvement[19]. Figure 4-4 provides the general layout of a typical experimental scheme for QCL-based multipass gas sensors.

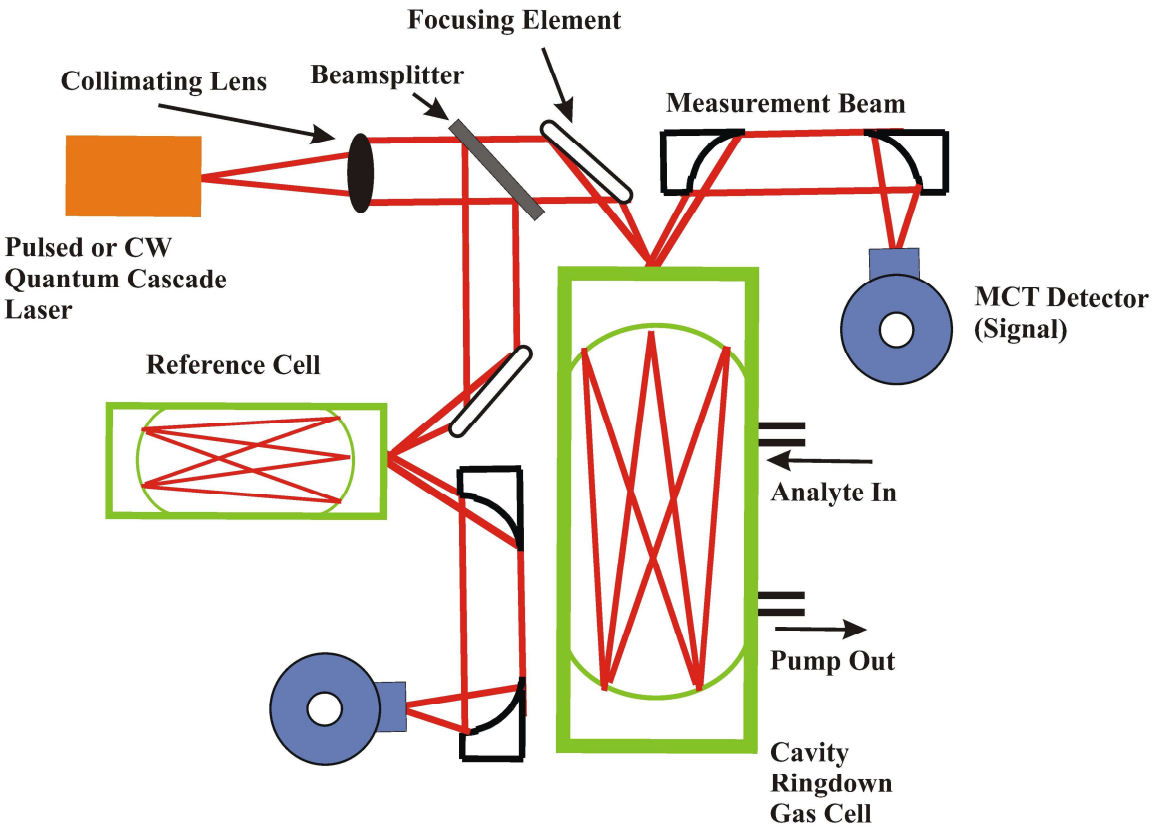

Figure 4-4: Example of a measurement setup using a QCL based multipass gas sensor. The measurement beam uses a multipath gas cell. After selective analyte absorption, the radiation is focused onto a mercury-cadmium-telluride (MCT) – or similar - detector. The reference beam may also contain the same type of cell as the measurement beam with or without a known concentration of the analyte or only containing the background matrix.

QCLs combined with multipass gas cells have been applied to trace gas analysis in human breath aiming at a noninvasive tool for detecting and quantifying volatile molecular constituents that could serve as biomarkers reflecting health or disease conditions. Menzel et al. have used a multipass gas cell with an effective optical path length of 100 meters for the detection of nitrous oxide (NO) in exhaled air down to concentrations of 3 ppb[20]. Another analyte quantified via pulsed QCLs and a multipass gas cell down to a noise-equivalent sensitivity (1σ) of 1.2 ppb with a 36 meter optical path length using the Herriott configuration is carbonyl sulfide (CS)[21], a volatile molecular constituent which at elevated concentrations in exhaled breath reportedly characterizes liver diseases in certain patient populations[22] and acute organ rejection for lung transplant patients[23].

Multipass gas cells with QCLs have also been implemented for environmental monitoring scenarios detecting ethylene (C_2H_4) down to concentrations of 30 ppb[24], and NO and methane (CH_3) down to levels of 0.3 and 4 ppb, respectively[17].

Water vapor isotope ratio measurements in air were also performed to monitor ozone conditions[25].

A wavelength-modulated QCL was used to measure NO concentrations with a multipass Herriott-type cell providing a 100 meter optical path length at concentration levels of a few parts per billion in diluted exhaust gas bag samples collected during vehicle certification processes[26].

Simultaneous analysis of mainstream and sidestream cigarette smoke was achieved using QCL-based gas phase spectroscopy in combination with a dual multipass gas cell setup to measure concentrations of NH_3, C_2H_4, NO and carbon dioxide (CO_2)[27].

Lastly, a single-mode pulsed InP-based QCL was coupled to a White cell with a 2.4 meter effective optical path length to obtain minimum noise-equivalent concentrations of NO between 16.7 and 23.3 ppbv[28].

Despite multipass gas cells improving detection limits down to the low-parts per billion concentration range, the required sample volumes can be as high as 3.5 L, thereby limiting the response time for continuous monitoring scenarios, and in some cases prove unfeasible due to the rather high sample volume such as in breath diagnostics, which frequently has to deal with breath sample volumes as low as 2–3 mL.

4.4.3 QCL Gas sensing using Cavity Enhancement Schemes

Cavity ring-down (CRD) spectroscopy is an extremely sensitive method for trace gas sensing with QCLs. Similar to multipass gas cells, CRD measurements also rely on multiple reflections between mirrors; however, a few main differences render this technique exquisitely sensitive. In a CRD setup, the gas absorption cell comprises two very low loss, highly reflective mirrors creating a high-finesse optical cavity. If QCL radiation is focused into this cavity in the absence of an analyte, the radiation intensity exponentially decays over a period of time (ring-down time) depending on the reflectance of the mirrors and the distance between them. In the presence of an analyte, this ring-down time decreases, as molecular species selectively absorb radiation, and thus, contribute to further losses in intensity of the initially provided radiation. Granted this absorption follows the Lambert–Beer law (see also section on transmission absorption spectroscopy), the CRD time can be defined in Equation 4-1:

$$\tau_0 \approx \frac{L}{c\left[\left(1-R_{eff}\right)+\alpha(\nu)L\right]} \qquad \text{(Eqn. 4-1)}$$

where R_{eff} is the effective reflectance of the mirrors, L is the distance between the mirrors, $\alpha(\nu)$ is the absorption coefficient of the molecular species as a function of frequency and c is the speed of light in vacuum[29]. The difference in ring-down time between an empty cavity and one containing analyte molecules can be used to derive the molecular absorption, and thus, the concentration of molecular species in a gaseous mixture. A diagram of a typical CRD experimental setup using QCLs is described in Figure 4-5.

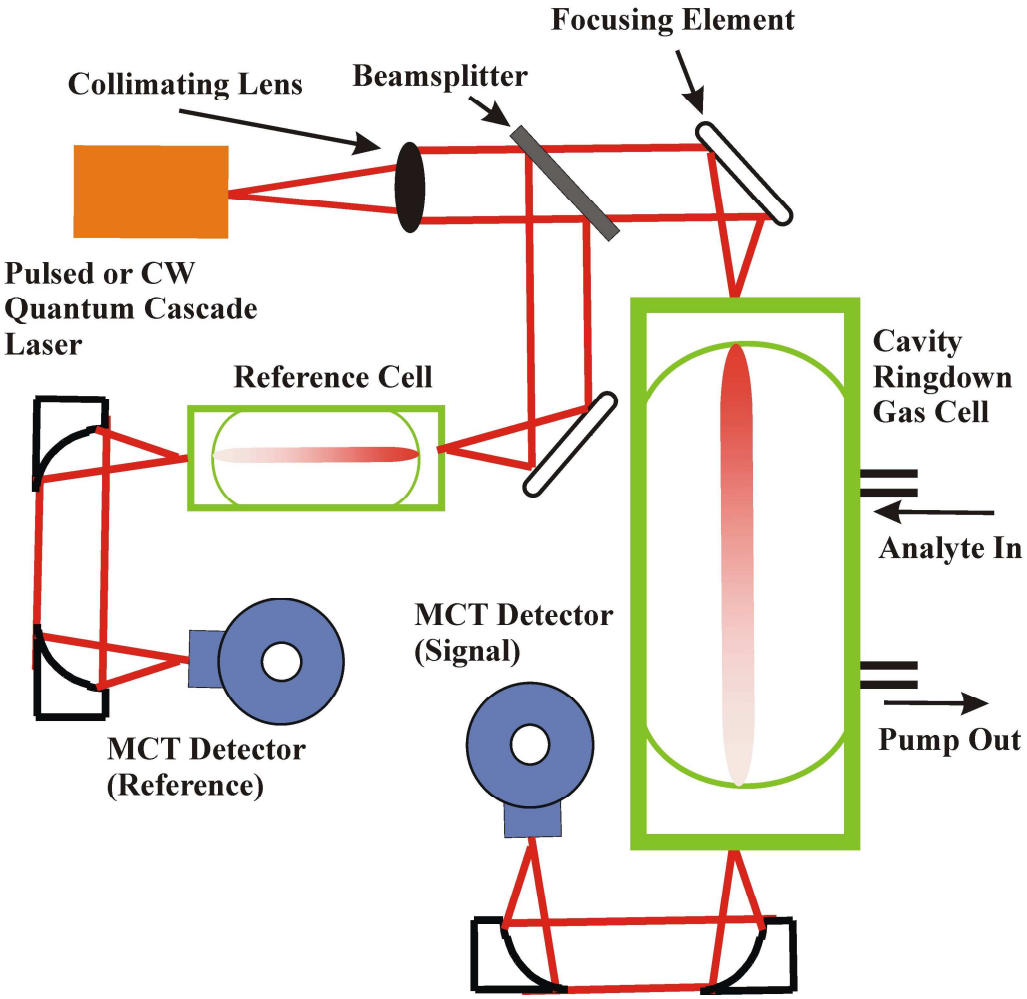

Figure 4-5: Example of a measurement setup using a QCL based cavity ringdown gas sensor. The decay of laser intensity after repetitive reflections between ultra low loss mirrors is measured over time. This decay time decreases by selective absorption of the analyte(s) of interest. The reference beam may also contain the same type of cell as the measurement beam with or without a known concentration of the analyte or only containing the background matrix.

One application of CRD spectroscopy combined with QCLs is the detection of biomarkers for breath diagnostics, whereby the sample volume is significantly smaller, as compared to, for example, multipass gas cells. Ammonia is among the biomarkers existing in breath of healthy individuals at a few parts per billion; however, in patients with malfunctioning kidneys the ammonia concentration frequently exceeds 1 ppm[29]. Paldus and coworkers have derived a noise-equivalent detection limit of 0.25 ppbv ammonia in nitrogen at standard temperature and pressure (STP) using a 16 mW cw DFB-QCL emitting at 1177 cm^{-1} (8.5 μm); however, this result was reported in nitrogen and at ideal experimental conditions, not in human breath[30]. More recently, Manne and coworkers have reported a sensitivity of 50 ppb ammonia in human breath with a time resolution of 20 s using a pulsed QCL-based CRD gas phase sensor[29].

NO is not only an analyte relevant in environmental monitoring, as previously described here, but is also an important volatile biomarker in breath and at cellular surfaces. One study, in particular, applied CRD spectroscopy in combination with a cw DFB-QCL operating at 1923 cm^{-1} (5.2 μm) to determine NO in nitrogen down to 48.4 ppb with a collection time of 8 s. In the outlook of this study, improved measurement conditions for ultimately determining NO in human breath are discussed[31].

A variation of CRD spectroscopy is a measurement scheme called cavity-enhanced absorption spectroscopy (CEAS), which is also known as integrated cavity output spectroscopy (ICOS). Herein, the signal exiting the optical cavity after absorption is

integrated over time, thereby resulting in orders of magnitude lower detection limits[32]. This technique yields an output signal that can by Equation 4-2 as:

$$I = \frac{I_L C_P T}{2(1-R)}(1-\exp(t/\tau)),\ \tau = \frac{L/c}{1-R} \qquad \text{(Eqn. 4-2)}$$

where I is the output signal after absorption, I_L is the laser intensity, C_P is the cavity coupling parameter, R and T are the mirror intensity reflection and transmission coefficients, ν is the CRD time, L is the distance between the two mirrors and c is the speed of light in vacuum[33].

Several studies have utilized off-axis ICOS in combination with QCLs to successfully quantify analytes in the gas phase. Off-axis ICOS is a variation of ICOS with QCL radiation focused into the device at an angle with respect to the cavity axis. One interesting application using this type of gas sensor was on board a NASA DC-8 aircraft, in which CO mixing ratios (molar fractions) down to 0.2 ppbv with an averaging time of 1 second were reported[33]. Noise-equivalent sensitivities of nitrous oxide were detected using this approach with wavelength modulation down to 2 ppbv and 15 s acquisition time[34], and further improved down to the sub-parts per billion by volume (ppbv) level (0.7 ppb) at 1 second acquisition time[35] in a related study.

4.4.4 QCL Gas sensing using Photoacoustic Transduction

Unlike the previous methods of gas detection based on optical absorption described above, photoacoustic spectroscopy relies on detecting a pressure change in a small

sample chamber that is generated by modulated MIR radiation[36]. This phenomenon occurs when incoming light is periodically modulated at rather low frequencies, thereby periodically heating the sample gas inside a resonant or non-resonant cavity resulting in an increase and decrease of pressure. Figure 4-6 shows the main components of a typical setup for QCL sensors based on photoacoustic spectroscopy.

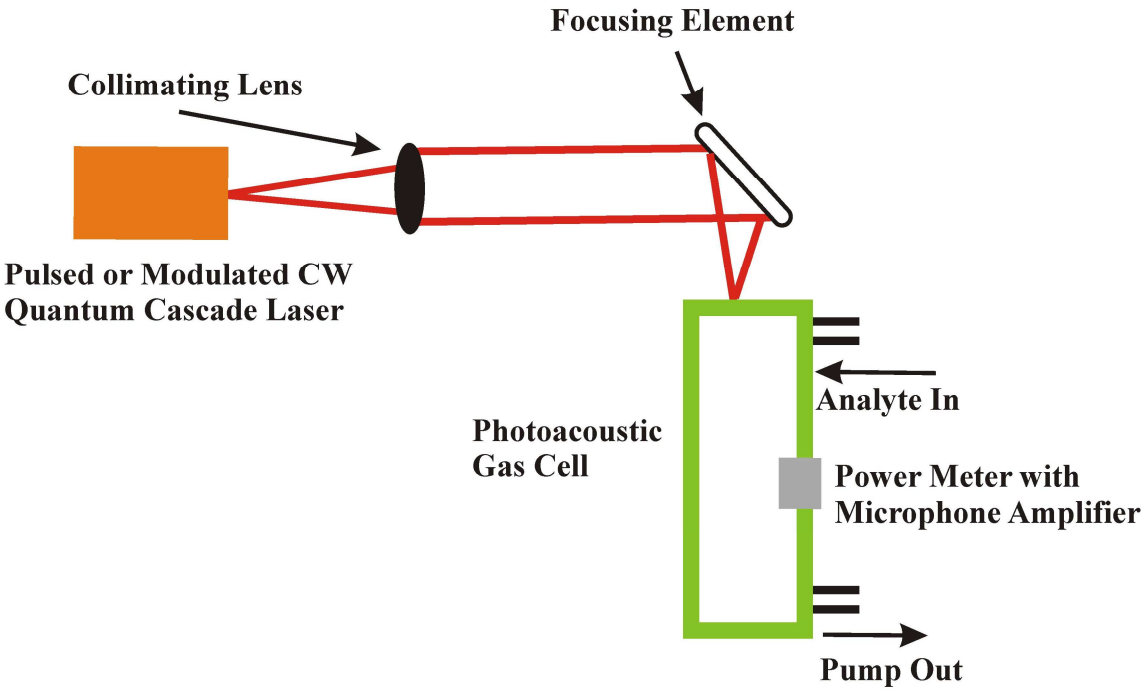

Figure 4-6: Example of measurement setup using a QCL based photoacoustic gas sensor. Modulated QCL radiation periodically heats the gas, thereby producing a pressure wave detectable at acoustic frequencies as a function of analyte concentration.

The detector, which can be a simple microphone or – in its latest incarnation – a quartz tuning fork[37-39], transduces the sound wave resulting from the pressure fluctuations as a function of the gas concentration. Gas sensors utilizing a resonant photoacoustic cell

(PAC) and a conventional microphone produce a photoacoustic signal (S) defined by Equation 4-3:

$$S = C \cdot P(\lambda) \cdot \alpha(\lambda) \qquad \text{(Eqn. 4-3)}$$

where C is the cell constant in volt centimeter per watt, P(λ) is the optical power of the QCL and α(λ) is the absorption coefficient of the molecular species as a function of frequency[40].

QCL PAC-based gas sensors have found a plethora of environmental monitoring applications dominated by the detection of atmospheric gases in the parts per billion concentration range. Ammonia is among the constituents of environmental concern due to its role in the nitrogen cycle[41], and as a human respiratory irritant[42]. Detection of ammonia in the gas phase was demonstrated by Paldus et al. down to a limit of detection of 100 ppbv with a 16 mW cw DFB-QCL lasing at 1176 cm^{-1} (8.5 μm) at a measurement time of 10 min and a PAC resonance at 1.6 kHz[43]. In another study, the detection limit of ammonia was further reduced down to 66 ppbv with a 2 mW pulsed DFB-QCL. The excitation radiation was modulated at 3.8 kHz, therefore, exciting the first longitudinal acoustic mode[42].

NO detection using a QCL PAC system was achieved down to concentrations of 500 ppb with a pulsed DFB-QCL lasing near 1886.79 cm^{-1} (5.3 μm), and an average laser power of 8 mW. Here, the resonator was excited to its first longitudinal mode at 1.38 kHz[44].

Another group attempted to enhance the sensitivity by using a radial 16-microphone array in lieu of a single microphone as the detector for their QCL-based PAC ammonia gas sensor. Consequently, a detection limit of 300 ppb with a Herriott cell multipass arrangement around the PAC was achieved[45].

Additional atmospheric gases have also been explored with QCL-based PAC gas sensors, such as the detection of ozone down to approximately 100 ppbv[46]. A setup utilizing two different QCLs was applied to measure nitric oxide and methane separately down to concentration levels of 3 and 14 ppb, respectively[47].

Alternatively, a quartz tuning fork can be used as the detector in lieu of a conventional microphone in combination with QCL-based photoacoustic measurements. This technique pioneered by Tittel and Kosterev is frequently referred to as quartz-enhanced photoacoustic spectroscopy (QEPAS)[38]. Utilizing a tuning fork instead of a microphone offers several distinct advantages, including most importantly, a much smaller probed volume for trace gas samples (<1 mm^3); the sample volume is no longer limited by the cell volume, but by the size of the tuning fork, as modulated QCL radiation is focused through the fork prongs instead of passing through an optical cell. This method naturally lends itself to field applications with improved immunity to interferences, that is, acoustic noise and a miniaturized sensor footprint (approximately 5 mm^3 as the typical dimensions)[48].

A QEPAS gas sensor developed by Kosterev et al. was used to measure NO down to a noise-equivalent sensitivity of 4 ppbv with a response time of 3 seconds[48]. Additional studies by the same group have demonstrated the detection of 1,1,1,2-tetrafluoroethane in nitrogen down to a normalized noise-equivalent absorption sensitivity (NEAS) of 2.0×10^{-8} Wcm^{-1} $Hz^{-1/2}$ with an amplitude-modulated QCL lasing at 1189 cm^{-1} (8.4 μm)[49]. Another exciting foray into photoacoustic spectroscopy has been the integration of EC tunable QCLs, as previously described in this chapter. More recently, Lewicki et al. were able to distinguish between two analytes, pentafluoroethane and acetone, in the same gaseous mixture by externally tuning the central QCL emission frequency to the main IR absorption features of each analyte. This was especially useful for this particular combination of molecules, as these analytes exhibit overlapping absorption features, which complicate quantitative discrimination of one analyte within a mixture without the aid of widely tunable QCLs. A single amplitude-modulated QCL source was tuned across 135 cm^{-1} (74.1 μm), thereby facilitating quantification of pentafluoroethane in mixture to a normalized NEAS of 2.64×10^{-9} Wcm−1 $Hz^{-1/2}$ [50].

4.4.5 QCL Gas sensing using Hollow Waveguides

Hollow waveguides (HWGs) can be described as light pipes comprising a structural tube (e.g. silica) internally coated with an IR reflective layer (e.g. silver), which is usually overcoated with a thin protective layer of silver iodide (AgI), thereby allowing for propagation of radiation via metallic reflection inside the hollow core[51]. This optical gas cell results in an enhanced optical beam path, and thus, increased absorption of gas

analytes present within the HWG core. Figure 4-7 visualizes a typical setup for QCL-based HWG gas phase chemical sensors.

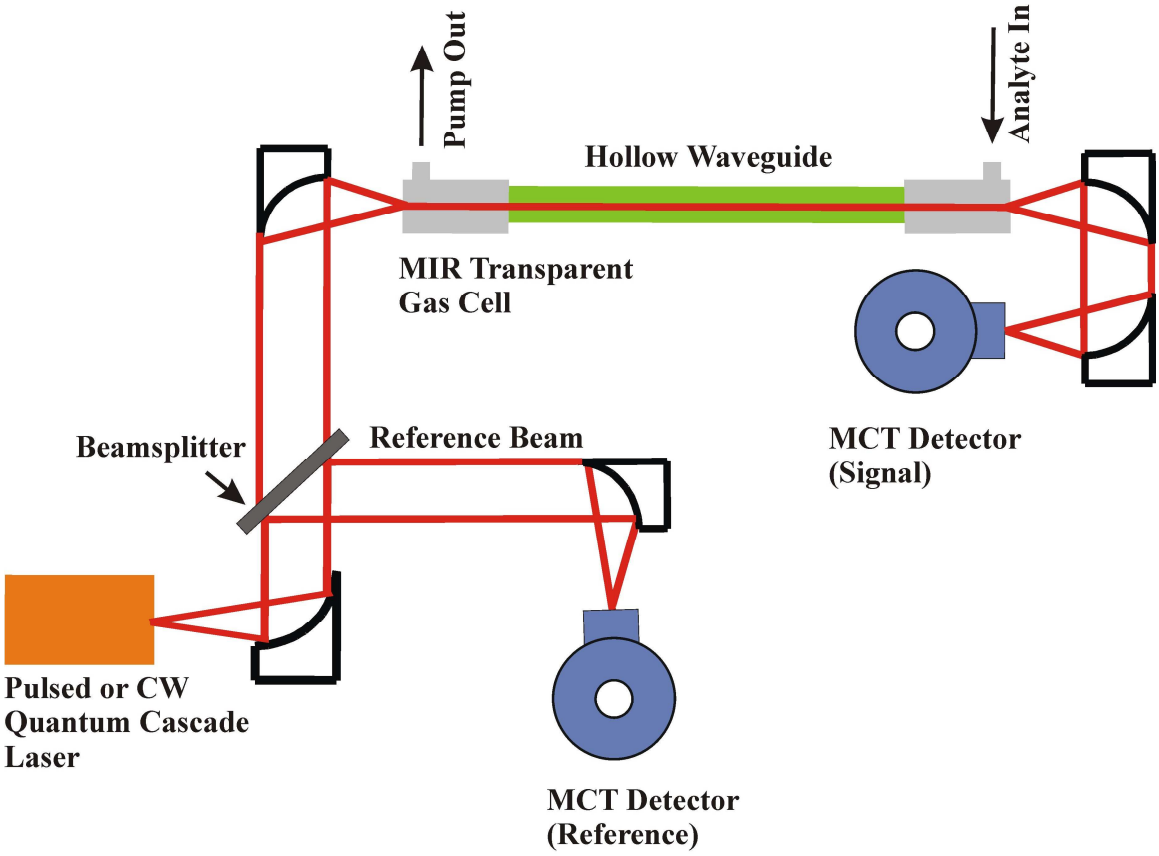

Figure 4-7: Example of measurement setup using a QCL based hollow waveguide gas sensor. The hollow waveguide simultaneously acts as both a gas cell and a light pipe, providing intimate interaction between photons and the analyte molecules within a small volume. The reference beam may also contain the same type of HWG cell as the measurement beam with or without a known concentration of the analyte or only containing the background matrix.

The HWG is used to efficiently transport radiation from the light source to the detector, and simultaneously serves as a miniaturized absorption gas cell.

A distinct advantage of HWGs to some of the other methods presented herein is the small internal volume, which usually suffices measurements at few milliliters of gaseous sample, thereby facilitating rapid response times (usually <10 seconds) in continuous sensing scenarios. As previously discussed, minute sample volumes are particularly advantageous for applications restricted to small sample volumes (i.e. few milliliters) such as breath diagnostics. In addition, due to the unique design of this particular type of gas sampling cell, HWGs could be used for remote sensing applications or at considerably harsh conditions providing a well-defined yet confined optical path of sufficient robustness against vibrations and other environmental parameters, due to the inherent integration of optical path and sample compartment.

In 2000, the group of Mizaikoff and collaborators pioneered the use of HWGs for gas sensing applications in combination with QCLs. A QCL lasing at 999 cm^{-1} (10 μm) coupled through a 43.4-cm-long segment of HWG, with the signal at the distal end of the HWG coupled into a Fourier-transform infrared (FT-IR) spectrometer for further analysis. With this setup, various concentrations of ethane in helium down to a detection threshold of approximately 250 ppm were determined [52].

The achievable detection limits were further improved by using a 4-m-long segment of HWG, as reported by Charlton et al. In this study, a QCL emitting at 971 cm^{-1} (10.3 μm)

was used to determine concentrations of ethyl chloride in air down to a limit of detection of approximately 500 ppb (v/v). Again, the QCL emission is quantitatively dampened in respect to the analyte concentration present within the HWG core[53]. Additionally, detection of ethyl chloride in air down to 30 ppb (v/v)[54] was achieved utilizing a frequency-matched photonic bandgap HWG and a QCL emitting at 970 cm^{-1} (10.3 μm) during exponential dilution experiments[55].

Limits of detection in the low parts per billion concentration range yet utilizing direct absorption techniques are an exciting prospect for QCL-based HWG gas sensors, as these levels are required for biomedical applications such as breath analysis and air monitoring, in addition to maintaining a simple and robust measurement technique with high time resolution[56]. Future research in this area predominantly focuses on biologically relevant constituents such as breath biomarkers, and seeks pushing the detection limits to sub-parts per billion levels.

4.5 Summary

In conclusion, to lay the foundation for the QCL based trace gas chemical sensors results presented in this thesis it is crucial to first review the state-of-the-art in mid-infrared light sources, as well as the basic operating principles of QCLs and related sensing schemes. This chapter discussed how QCLs function in contrast to conventional laser sources, demonstrating that this fundamentally different approach allows for room temperature operable and miniaturized light sources with flexible tuning options. Rather than electron-hole recombination, QCLs generate photons via cascaded electron tunneling producing many photons per electron. Mid-infrared chemical sensors utilizing quantum cascade lasers offer an excellent solution to modern sensing applications demanding high-molecular selectivity, low sensitivity and fast response times by taking advantage of distinct molecular signatures inherent to most molecules with flexible tuning options, while offering robust devices, and a compact footprint facilitating real-world utilization.

Sections of this chapter are taken from the pre-peer reviewed version of the following book chapter: Young, C.; Kim, S.-S.; Mizaikoff, B.; Lackner, M. (ed.). Lasers in Chemistry: Probing and Influencing Matter. Pages 73 – 94. Copyright Wiley-VCH Verlag GmbH & Co. KGaA. Reproduced with permission.

References

[1]C. Young, S.-S. Kim, and B. Mizaikoff, Quantum Cascade Laser Based Gas and Liquid Chemical Sensors. in: M. Lackner, (Ed.), Lasers in Chemistry, Wiley-VCH, Weinhem, 2008.

[2]C.K.N. Patel, Interpretation of CO_2 Optical Maser Experiments. Physical Review Letters 12 (1964) 588-590.

[3]C.K.N. Patel, Continuous-Wave Laser Action on Vibrational-Rotational Transitions of CO_2 Physical Review Letters 136 (1964) A1187-A1193.

[4]W. Urban, Physics and Spectroscopic Applications of Carbon-Monoxide Lasers, A Review. Infrared Physics and Technology 36 (1995) 465-473.

[5]R.F. Kazarinov, and R.A. Suris, Possible amplification of electromagnetic waves in a semiconductor with a superlattice. Fizika i Tekhnika Poluprovodnikov 5 (1971) 797-800.

[6]J. Faist, F. Capasso, D.L. Sivco, C. Sirtori, A.L. Hitchinson, and A.Y. Cho, Quantum Cascade Laser. Science 264 (1994) 553-556.

[7]C. Gmachl, R. Paiella, A. Tredicucci, A.L. Hutchinson, D.L. Sivco, J.N. Baillargeon, A.Y. Cho, and H.C. Liu, New frontiers in quantum cascade lasers and applications. IEEE Journal of Selected Topics in Quantum Electronics 6 (2000) 931-947.

[8]S. Forget, C. Faugeras, E.B. Duchemin, J.Y. Bengloan, C. Sirtori, M. Calligaro, O. Parillaud, H. Page, M. Giovannini, and J. Faist, Room-temperature CW operation of (lambda~ 9 m) InP-based quantum cascade lasers in: A. Jonathan, C. Terry,

and W.A. Clarkson, (Eds.), Solid State Laser Technologies and Femtosecond Phenomena, SPIE, Bellingham, WA, 2004, pp. 101-111.

[9]C. Young, S.-S. Kim, Y. Luzinova, M. Weida, D. Arnone, E. Takeuchi, T. Day, and B. Mizaikoff, External cavity widely tunable quantum cascade laser based hollow waveguide gas sensors for multianalyte detection. Sensors & Actuators: B. Chemical 140 (2009) 24-28.

[10]C. Sirtori, H. Page, C. Becker, and V. Ortiz, GaAs-AlGaAs Quantum Cascade Lasers: Physics, Technology, and Prospects. IEEE Journal of Quantum Electronics 38 (2002) 547-558.

[11]C. Gmachl, F. Capasso, A. Tredicucci, D.L. Sivco, R. Kohler, A.L. Hutchinson, and A.Y. Cho, Dependence of the device performance on the number of stages in quantum cascade lasers. IEEE Journal of Selected Topics in Quantum Electronics 5 (1999) 808-816.

[12]J. Faist, C. Gmachl, F. Capasso, C. Sirtori, D.L. Sivco, and J.N. Baillargeon, Applied Physics Letters 71 (1997) 986.

[13]J. Faist, C. Gmachl, F. Capasso, C. Sirtori, D.L. Sivco, J.N. Baillargeon, and A.Y. Cho, Distributed feedback quantum cascade lasers. Applied Physics Letters 70 (1997) 2670-2672.

[14]C. Gmachl, J. Faist, J.N. Baillargeon, F. Capasso, C. Sirtori, D.L. Sivco, C. S.N.G., and A.Y. Cho, Complex-coupled quantum cascade distributed-feedback laser. IEEE Photonics Technology Letters 9 (1997) 1090-1092.

[15]G. Wysocki, A.A. Kosterev, and F.K. Tittel, Spectroscopic trace-gas sensor with rapidly scanned wavelengths of a pulsed quantum cascade laser for in situ NO

monitoring of industrial exhaust systems. Applied Physics B: Lasers and Optics 80 (2005) 617-625.

[16]W.T. Rawlins, J.M. Hensley, D.M. Sonnenfroh, D.B. Oakes, and M.G. Allen, Quantum cascade laser sensor for SO2 and SO3 for application to combustor exhaust streams. Applied Optics 44 (2005) 6635-6643.

[17]D. Weidmann, F.K. Tittel, T. Aellen, M. Beck, D. Hofstetter, J. Faist, and S. Blaser, Mid-infrared trace-gas sensing with a quasi-continuous-wave Peltier-cooled distributed feedback quantum cascade laser. Applied Physics B: Lasers and Optics 79 (2004) 907-913.

[18]P. Werle, and F. Slemr, Signal-to-noise ratio analysis in laser absorption spectrometers using optical multipass cells. Applied Optics 30 (1991) 430-434.

[19]J.B. McManus, P.L. Kebabian, and M.S. Zahniser, Astigmatic mirror multipass absorption cells for long-path-length spectroscopy. Applied Optics 34 (1995) 3336-3348.

[20]L. Menzel, A.A. Kosterev, R.F. Curl, F.K. Tittel, C. Gmachl, F. Capasso, D.L. Sivco, J.N. Baillargeon, A.L. Hutchinson, A.Y. Cho, and W. Urban, Spectroscopic detection of biological NO with a quantum cascade laser. Applied Physics B: Lasers and Optics 72 (2001) 859-863.

[21]G. Wysocki, M. McCurdy, S. So, D. Weidmann, C. Roller, R.F. Curl, and F.K. Tittel, Pulsed quantum-cascade laser-based sensor for trace-gas detection of carbonyl sulfide. Applied Optics 43 (2004) 6040-6046.

[22]S.S. Sehnert, L. Jiang, J.F. Burdick, and T.H. Risby, Breath biomarkers for detection of human liver diseases: preliminary study. Biomarkers 7 (2002) 174-187.

[23]S.M. Studer, J.B. Orens, I. Rosas, J.A. Krishnan, K.A. Cope, S. Yang, J.V. Conte, P.B. Becker, and T.H. Risby, Patterns and significance of exhaled-breath biomarkers in lung transplant recipients with acute allograft rejection. J. Heart Lung Transplant 20 (2001) 1158-1166.

[24]D. Weidmann, A.A. Kosterev, C. Roller, R.F. Curl, M.P. Fraser, and F.K. Tittel, Monitoring of ethylene by a pulsed quantum cascade laser. Applied Optics 43 (2004) 3329-3334.

[25]L. Joly, V. Zeninari, B. Parvitte, D. Courtois, and G. Durry, Water-vapor isotope ratio measurements in air with a quantum-cascade laser spectrometer. Optics Letters 31 (2006) 143-145.

[26]W.H. Weber, J.T. Remillard, R.E. Chase, J.F. Richert, F. Capasso, C. Gmachl, A.L. Hutchinson, D.L. Sivco, J.N. Baillargeon, and A.Y. Cho, Using a wavelength-modulated quantum cascade laser to measure NO concentrations in the parts-per-billion range for vehicle emissions certification. Applied Spectroscopy 56 (2002) 706-714.

[27]R.E. Baren, M.E. Parrish, K.H. Shafer, C.N. Harward, Q. Shi, D.D. Nelson, J.B. McManus, and M.S. Zahniser, Quad quantum cascade laser spectrometer with dual gas cells for the simultaneous analysis of mainstream and side-stream cigarette smoke. Spectrochimica Acta, Part A: Molecular and Biomolecular Spectroscopy 60A (2004) 3437-3447.

[28]C. Mann, Q. Yang, F. Fuchs, W. Bronner, K. Koehler, T. Beyer, M. Braun, and A. Lambrecht, Single-mode InP-based quantum cascade lasers for applications in

trace-gas sensing. Proceedings of SPIE-The International Society for Optical Engineering 5365 (2004) 173-183.

[29]J. Manne, O. Sukhorukov, W. Jager, and J. Tulip, Pulsed quantum cascade laser-based cavity ring-down spectroscopy for ammonia detection in breath. Applied Optics 45 (2006) 9230-7.

[30]B.A. Paldus, C.C. Harb, T.G. Spence, R.N. Zare, C. Gmachl, F. Capasso, D.L. Sivco, J.N. Baillargeon, A.L. Hutchinson, and A.Y. Cho, Cavity ringdown spectroscopy using mid-infrared quantum-cascade lasers. Optics Letters 25 (2000) 666-668.

[31]A.A. Kosterev, A.L. Malinovsky, F.K. Tittel, C. Gmachl, F. Capasso, D.L. Sivco, J.N. Baillargeon, A.L. Hutchinson, and A.Y. Cho, Cavity ringdown spectroscopic detection of nitric oxide with a continuous-wave quantum-cascade laser. Applied Optics 40 (2001) 5522-5529.

[32]A.A. Kosterev, and F.K. Tittel, Chemical sensors based on quantum cascade lasers. IEEE Journal of Quantum Electronics 38 (2002) 582-591.

[33]R. Provencal, M. Gupta, T.G. Owano, D.S. Baer, K.N. Ricci, A. O'Keefe, and J.R. Podolske, Cavity-enhanced quantum-cascade laser-based instrument for carbon monoxide measurements. Applied Optics 44 (2005) 6712-6717.

[34]Y.A. Bakhirkin, A.A. Kosterev, C. Roller, R.F. Curl, and F.K. Tittel, Mid-infrared quantum cascade laser based off-axis integrated cavity output spectroscopy for biogenic nitric oxide detection. Applied Optics 43 (2004) 2257-2266.

[35]Y.A. Bakhirkin, A.A. Kosterev, R.F. Curl, F.K. Tittel, D.A. Yarekha, L. Hvozdara, M. Giovannini, and J. Faist, Sub-ppbv nitric oxide concentration measurements

using cw thermoelectrically cooled quantum cascade laser-based integrated cavity output spectroscopy. Applied Physics B: Lasers and Optics 82 (2006) 149-154.

[36]A.G. Bell, Upon the Production of Sound by Radiant Energy. Philosophical Magazine 11 (1881) 510-528.

[37]A. Kosterev, F. Tittel, D. Serebryakov, A. Malinovsky, and I. Morozov, Applications of quartz tuning forks in spectroscopic gas sensing. Review of Scientific Instruments 76 (2005) 043105.

[38]A.A. Kosterev, Y.A. Bakhirkin, R.F. Curl, and F.K. Tittel, Quartz-enhanced photoacoustic spectroscopy. Optics Letters 27 (2002) 1902-1904.

[39]R. Lewicki, G. Wysocki, A.A. Kosterev, and F.K. Tittel, QEPAS based detection of broadband absorbing molecules using a widely tunable, cw quantum cascade laser at 8.4 μm. Optics Express 15 (2007) 7357-7366.

[40]A. Elia, C. Di Franco, P.M. Lugara, and G. Scamarcio, Photoacoustic spectroscopy with quantum cascade lasers for trace gas detection. Sensors 6 (2006) 1411-1419.

[41]J. Kaiser, The other global pollutant: nitrogen proves tough to curb. Science 294 (2001) 1268-1296.

[42]M.B. Filho, M.G. da Silva, M.S. Sthel, D.U. Schramm, H. Vargas, A. Miklos, and P. Hess, Ammonia detection by using quantum-cascade laser photoacoustic spectroscopy. Applied Optics 45 (2006) 4966-4971.

[43]B.A. Paldus, T.G. Spence, R.N. Zare, J. Oomens, F.J.M. Harren, D.H. Parker, C. Gmachl, F. Cappasso, D.L. Sivco, J.N. Baillargeon, A.L. Hutchinson, and A.Y. Cho, Photoacoustic spectroscopy using quantum-cascade lasers. Optics Letters 24 (1999) 178-180.

[44]A. Elia, P.M. Lugara, and C. Giancaspro, Photoacoustic detection of nitric oxide by use of a quantum-cascade laser. Optics Letters 30 (2005) 988-990.

[45]D. Hofstetter, M. Beck, J. Faist, M. Nagele, and M.W. Sigrist, Photoacoustic spectroscopy with quantum cascade distributed-feedback lasers. Optics Letters 26 (2001) 887-889.

[46]M.G. da Silva, H. Vargas, A. Miklos, and P. Hess, Photoacoustic detection of ozone using a quantum cascade laser. Applied Physics B: Lasers and Optics 78 (2004) 677-680.

[47]A. Grossel, V. Zeninari, B. Parvitte, L. Joly, and D. Courtois, Optimization of a compact photoacoustic quantum cascade laser spectrometer for atmospheric flux measurements: application to the detection of methane and nitrous oxide. Applied Physics B: Lasers and Optics 88 (2007) 483-492.

[48]A.A. Kosterev, Y.A. Bakhirkin, and F.K. Tittel, Ultrasensitive gas detection by quartz-enhanced photoacoustic spectroscopy in the fundamental molecular absorption bands region. Applied Physics B: Lasers and Optics 80 (2005) 133-138.

[49]M.D. Wojcik, M.C. Phillips, B.D. Cannon, and M.S. Taubman, Gas-phase photoacoustic sensor at 8..41 mm using quartz tuning forks and amplitude-modulated quantum cascade lasers. Applied Physics B: Lasers and Optics 85 (2006) 307-313.

[50]R. Lewicki, G. Wysocki, A.A. Kosterev, and F.K. Tittel, QEPAS based detection of broadband absorbing molecules using a widely tunable, cw quantum cascade laser at 8.4 mm. Optics Express 15 (2007) 7357-7366.

[51]J.A. Harrington, A review of IR transmitting, hollow waveguides. Fiber and Integrated Optic 19 (2000) 211-227.

[52]L. Hvozdara, S. Gianordoli, G. Strasser, W. Schrenk, K. Unterrainer, E. Gornik, C.S.S.S. Murthy, M. Kraft, V. Pustogow, B. Mizaikoff, A. Inberg, and N. Croitoru, Spectroscopy in the gas phase with GaAs/AlGaAs quantum-cascade lasers. Applied Optics 39 (2000) 6926-6930.

[53]C. Charlton, F. de Melas, A. Inberg, N. Croitoru, and B. Mizaikoff, Hollow-waveguide gas sensing with room-temperature quantum cascade lasers. IEE Proceedings: Optoelectronics 150 (2003) 306-309.

[54]C. Charlton, B. Temelkuran, G. Dellemann, and B. Mizaikoff, Midinfrared sensors meet nanotechnology: Trace gas sensing with quantum cascade lasers inside photonic band-gap hollow waveguides. Applied Physics Letters 86 (2005) 194102/1-194102/3.

[55]J.E. Lovelock, Ionization methods for the analysis of gases and vapors. Analytical Chemistry 33 (1961) 162-78.

[56]C. Charlton, A. Inberg, N.I. Croitoru, and B. Mizaikoff, Hollow waveguide infrared gas sensing for biomedical applications. Proceedings of SPIE-The International Society for Optical Engineering 4957 (2003) 116-123.

CHAPTER 5

ENHANCING QCL WAVELENGTH SELECTION BY CAVITY LENGTH VARIATION

QCL based chemical sensors require the ability to precisely select emission frequency to directly overlap analyte absorption bands for sensitive and selective molecular detection. This chapter discusses a new technique to deliberately select QCL wavelength by varying the cavity length. In contrast to the tuning techniques discussed in Chapter 5, modifying the cavity length is a straightforward postprocessing procedure. A systematic shift in spectral emission wavenumbers in QCLs is observed over a variation in cavity lengths from 0.5 to 3 mm resulting in a gain peak shift ranging from 2404 to 2286 cm^{-1}. Thereby, a wavelength selection range of 118 cm^{-1} is provided, which is sufficiently broad for selecting the laser emission across the entire CO_2 absorption band at 2326 cm^{-1} (4.3 μm). Experimental evidence confirms that this frequency shift is due to a change in threshold voltage and applied electric field as a function of cavity length which is in agreement with the theory.

5.1 Motivation and State-of-the-Art

The ability to deliberately select a QCL emission frequency is of significant interest for precisely overlapping analyte vibrational-rotational absorption bands with the laser emission, thereby providing inherent molecular selectivity and enhanced sensitivity for trace gas and liquid chemical sensors[1, 2]. Current methods for selecting the QCL emission

frequency include the use of an external cavity[3-8], an array of single-mode lasers with a variety of emission frequencies monolithically fabricated on one chip[9], or adjusting the heatsink temperature using a cryostat or dc laser injection current[9-11].

The simplest tuning scheme for the emission wavelength is provided by thermal tuning. Thermal tuning takes advantage of thermal expansion of the laser gain medium and the increase of the optical index with temperature. Therefore, changing the temperature of the gain medium causes the resonant condition of the cavity to change, which works in FP and DFB lasers. Although thermal tuning of QCLs offers tunability to some extent, the tuning rate is limited from approximately −0.05 to −0.15cm^{-1} K^{-1} [2, 4].

External cavity tunable QCLs[3-8] operate by changing the angle of an external diffraction grating, which creates single mode emission via frequency selective feedback, thereby continuously tuning over a broad spectral range[2]. Although a tuning range of over 250 cm^{-1} has recently been demonstrated[5], the gain spectrum does not tune at all or at a much smaller rate than optical tuning, therefore resulting in a decrease in output power for both blueshift and redshift from the central emission frequency. While a shift of the gain spectrum may be achieved by temperature tuning, this is not widely applicable to room temperature operated systems; therefore, alternative strategies for tuning the gain spectrum are in demand. Additional information regarding external cavity tunable QCLs is provided in the next chapter.

In contrast to thermal and external cavity tuning, the present study describes tailoring the QCL cavity length for tuning the gain spectrum. Modification of cavity length is a straight forward post-processing selection parameter, and therefore ideally suited for conveniently adjusting the QCL gain spectrum and selecting the peak gain wavelength. For the QCL presented here, the wavelength selection range is wide enough to span an entire vibrational-rotational absorption feature of carbon dioxide (CO_2)[12].

5.2 Theory

5.2.1 Conduction Band Energy Diagram

As QCLs emitting at the wavelength relevant for BTX are not available to date, quantum cascade lasers designed for a central emission frequency at 2326 cm^{-1} (4.3 μm) were used in the present study. A corresponding band diagram is shown in Figure 5-1 where the blue color designates the upper laser level, the green color designates the injector ground level to the lower laser level and the red arrow symbolizes the 3-2 optical lasing transition in which a photon is generated.

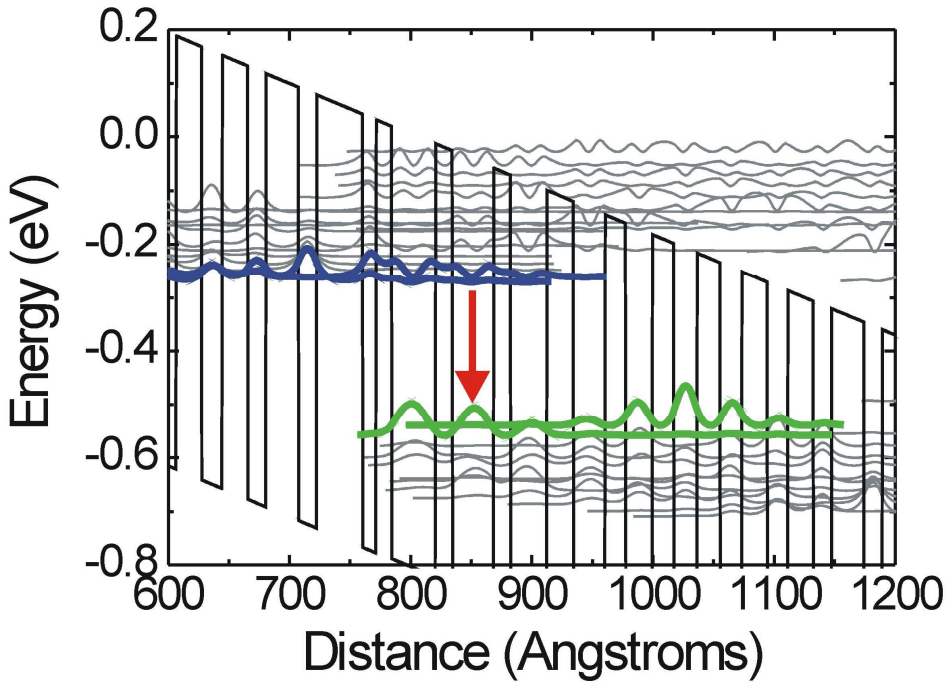

Figure 5-1: Conduction band energy diagram of the QCL designed to emit at 4.3 μm.

The layer sequence in Angstroms of one period of the active region and injector is 26/**17**/22/**18**/<u>19/**19**</u>/18/**21**/17/**21**/15/**27**/15/**38**/11/**13**/36/**14**/34/**14**/30/**22**, where $Al_{0.65}In_{0.35}As$ barrier layers are marked in bold, $Ga_{0.32}In_{0.68}As$ well layers are given in regular font, and n-doped (2.1×10^{17} cm^{-3}) layers are underlined.

While Figure 5-1 illustrates one period, the generation of many photons is a cascading mechanism through several periods (i.e. 33) for the QCL presented in this study. Figure 5-2 shows three periods with injector and active regions labeled with blue and black borders, respectively.

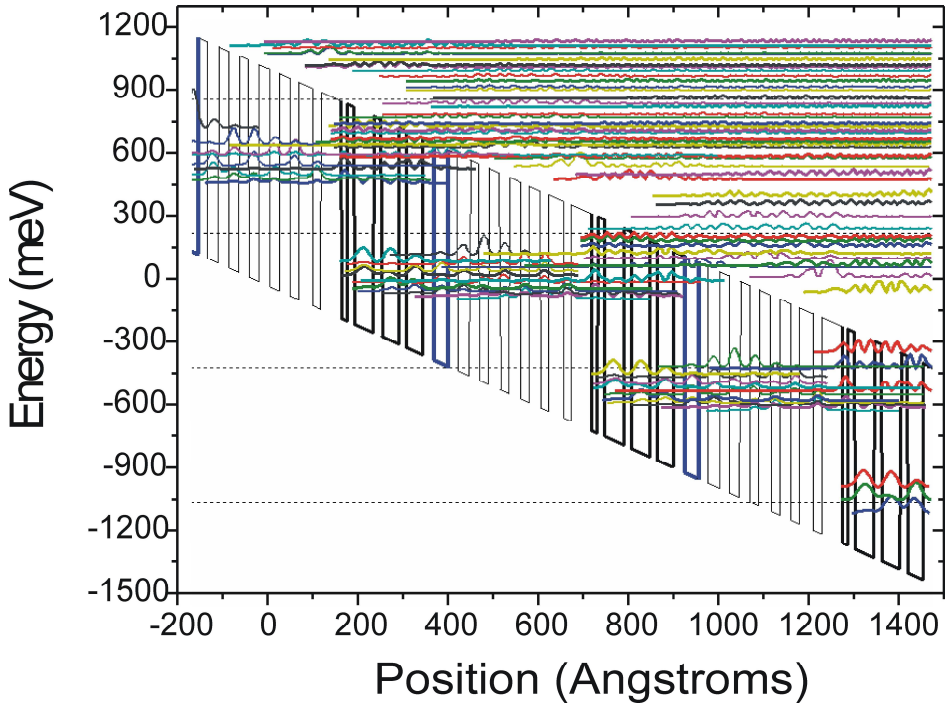

Figure 5-2: BH QCL band energy diagram of three periods designed to emit at 4.3 microns. The blue and black borders represent injector and active regions, respectively and the multicolored lines represent wavefunctions. Dr. Kale Franz, Prof. Claire Gmachl, and her group at Princeton University, Department of Electrical Engineering, are credited for assistance in production of this plot.

Appendix B details the heterostructure design with layer thicknesses in Angstroms.

5.2.2 Theoretical Prediction of the Emission Wavelength

The conduction band energy diagram of this structure was calculated as a function of the applied electric field from 87 to 116 kV/cm yielding an expected transition frequency range from 2137 to 2583 cm^{-1}, as illustrated in Figure 5-3.

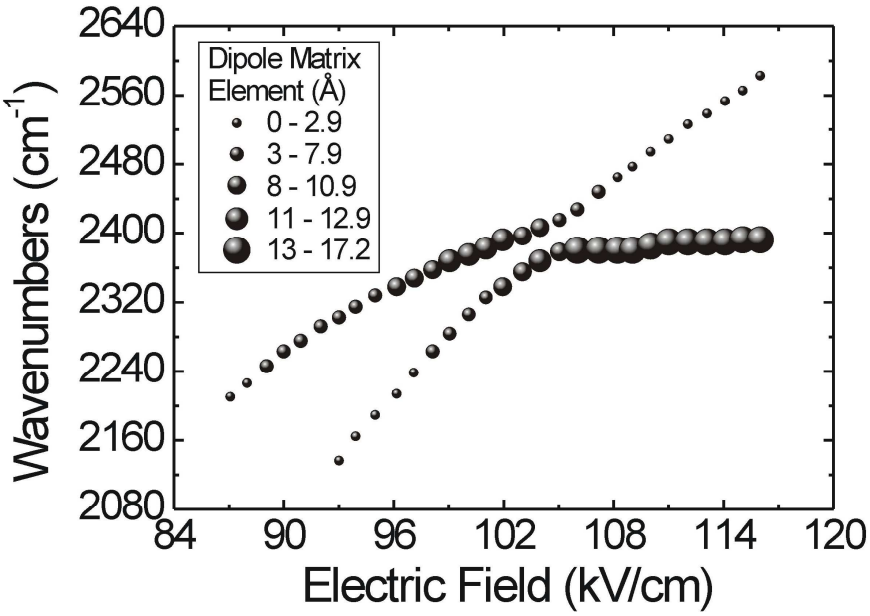

Figure 5-3: Theoretical prediction of the laser emission wavenumber versus the electric field.

It is important to note in this figure that the overall blueshift of the transition with increasing field can be observed.

The theoretical electric field in Figure 5-3 (x-axis) is calculated by Equation 5-1:

$$Electric\ Field = \frac{Theoretical\ Bias\,(kV) - Contact\ Voltage\,(kV)}{\left(\sum Active\ Core\ Layers\right) * \left(\#\ of\ Periods\right)} \qquad \text{(Eqn. 5-1)}$$

where the contact voltage is assumed to be one Volt, and the sum of active core layers as 467 Angstroms.

The theoretical emission in wavenumbers (y-axis) of Figure 5-3 is calculated using Equation 5-2:

$$\lambda_{TH} = \frac{hc}{E} = \frac{6.63x10^{-34}\,Js * 3x10^{8}\,m/s}{\left(Energy\,Difference\left(meV\right) * 0.001\right) * 1eV} \qquad \text{(Eqn. 5-2)}$$

where the energy difference in meV is for the 3-2 lasing transition given the electric field (Equation 5-1) and the bandstructure above.

From Chapter 4 it is known that population inversion between the upper and lower states is achieved by altering the thickness of quantum heterostructure layers, which in turn affects the energy difference, and thus the emission wavelength, as described in Equation 5-2. Once band structure engineering is optimized, changing the theoretical electric field may yield several possible optical transitions resulting in a specific wavelength, each with a certain likelihood of occurrence, as characterized by the strength of the frequency transition. How well the upper and lower laser states are coupled is represented here by the optical dipole matrix element (Angstroms), which may be calculated from Equation 5-4:

$$\int_{-\infty}^{\infty} \Psi_{E_3}^{*} * z * \Psi_{E_2}\, dz \qquad \text{(Eqn. 5-4)}$$

where $\Psi_{E_3}^{*}$ and Ψ_{E_2} are the upper and lower states, respectively, and z is the direction of laser epitaxial growth. The closer this integral approaches the value of 1, the higher the

probability of achieving emission, if a photon is near the optical transition. Additionally, the closer this integral approaches the value of 0, the opposite is true.

Figure 5-3 presents these peak transition energies for the upper laser level and the injector ground level to the lower laser level by the optical dipole matrix element, as indicated by the size of the symbols (spheres).

The peak transition energies plotted in Figure 5-3 only demonstrate two of several possible optical transitions, because the strengths of their dipole matrix elements make them more likely to be the transitions that support the experimental spectral emissions desired here. For a more comprehensive representation, Figure 5-4 also illustrates some additional calculated transitions that could theoretically occur.

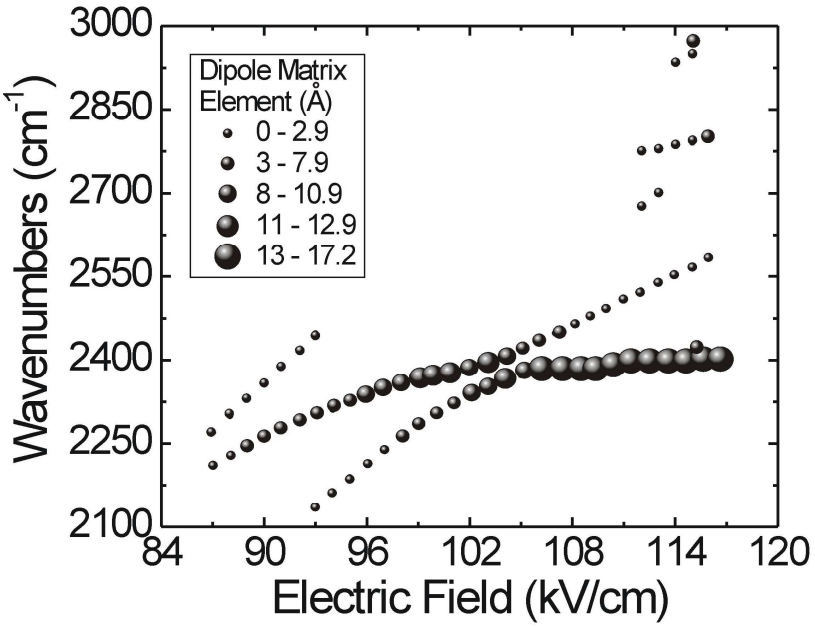

Figure 5-4: Possible theoretical transitions according to the strength of the frequency transition.

Appendix C tabulates all possible optical transitions with calculated optical dipole matrix elements and non-radiative (LO phonon) scattering times for the quantum heterostructure presented here, which were numerically solved from Schrödinger's Equation.

In addition, it is also important to note that the calculated frequency increases with increasing applied electric field due to the linear Stark effect inherent to the "diagonal" transition design[13]. The dipole matrix element reaches a maximum around the designated electric field of 103 kV/cm, which coincides with the anticrossing field. As the emission frequency depends on the operating threshold voltage (Figures 5-3 and 5-4), a change in laser threshold voltage therefore enables tuning of the gain spectrum. The former can be achieved by changing the threshold current density, which in turn is most efficiently modified by changing the cavity length. This circumstance has been experimentally verified during this thesis, thereby establishing this novel concept for tailoring the laser emission frequency as a useful and practically applicable tool.

5.3 Experimental

5.3.1 QCL Sub-Mount Preparation

Having modeled the theoretical wavelength emission given an optimized quantum heterostructure design, the laser is then be grown by molecular beam epitaxy (MBE). The result is a FP-QCL chip, from which - prior to emission characterization experiments via

FT-IR spectroscopy - single QCL cavities are cleaved. An image of the FP-QCL chip is shown in Figure 5-5 with the white lines representing alignment lines. These lines are used to measure the length of the cavity to be cleaved.

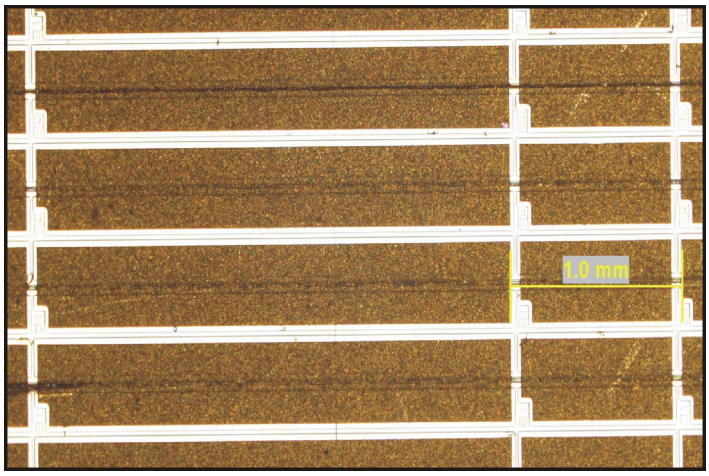

Figure 5-5: Microscope image of FP-QCL chip with alignment lines. The yellow scale bar represents a length of 1.0 mm.

The cleaving and mounting procedure is schematically described in Figure 5-6.

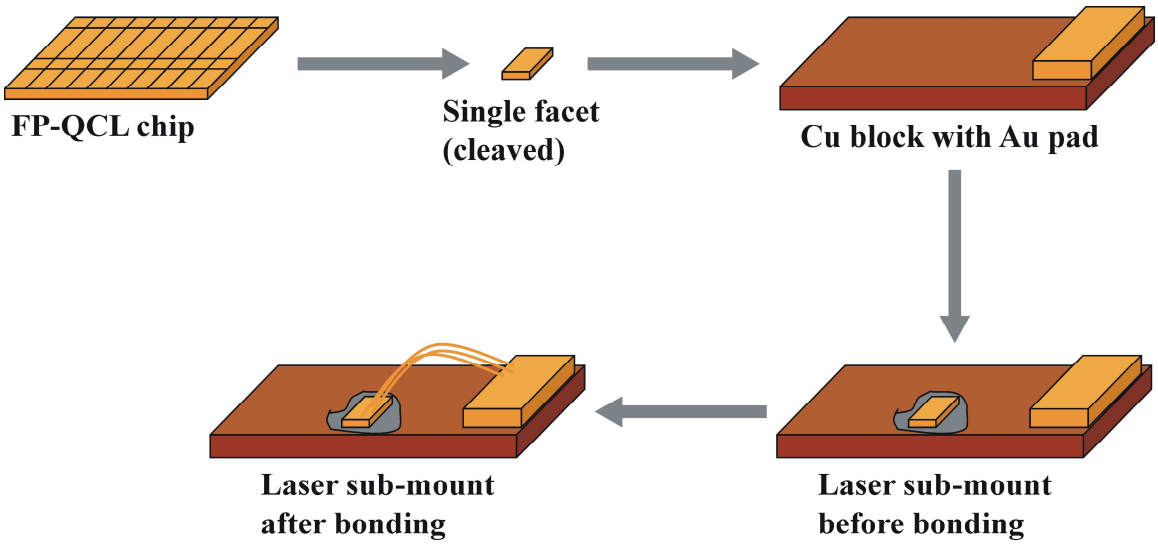

Figure 5-6: Cleaving and mounting process for a QCL.

The first step in this process was to cleave in the plane of the crystal lattice using a diamond knife under the microscope by scribing in place along the alignment lines onto the FP-QCL chip resulting in a single cleaved facet. Next, a laser sub-mount was prepared by gluing an insulated gold pad onto a copper block. $In_{0.97}Ag_{0.3}$ was then applied to a copper (Cu) block, and the laser was aligned on top with micro-tweezers. The copper block served as both a heatsink and electrical ground. As alignment continued, the sub-mount was heated from 130 degrees Celsius to 180 degrees Celsius, and then then back to 130 degrees Celsius, which chemically bonded the single facet to the copper block. Finally, gold (Au) wires were bonded from the gold pad to QCL chip for transporting electrical current. Laser widths ranged from 4.6 to 6.1 μm, as measured by a microscope. Figure 5-7 shows a single cleaved facet mounted and bonded to a copper block. The scale represented here as "L" is the length of the cleaved cavity. Different cavity lengths may be individually fabricted using the aforementioned process.

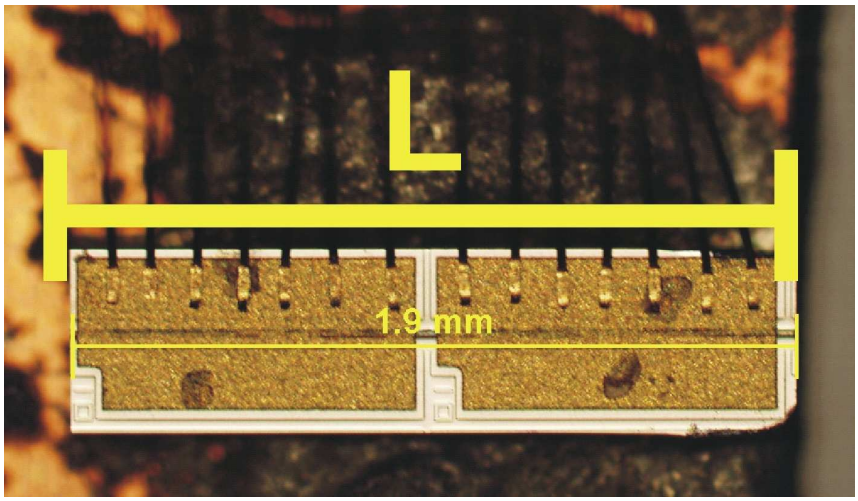

Figure 5-7: Microscope image of a single cleaved QCL facet with gold wires bonded to the surface. The yellow scale bars represent a length of 1.9 mm.

The laser sub-mount shown here is used in a typical laboratory approach. Figure 5-8 illustrates the "C-mount", which is an industrial standard for packaging QCLs.

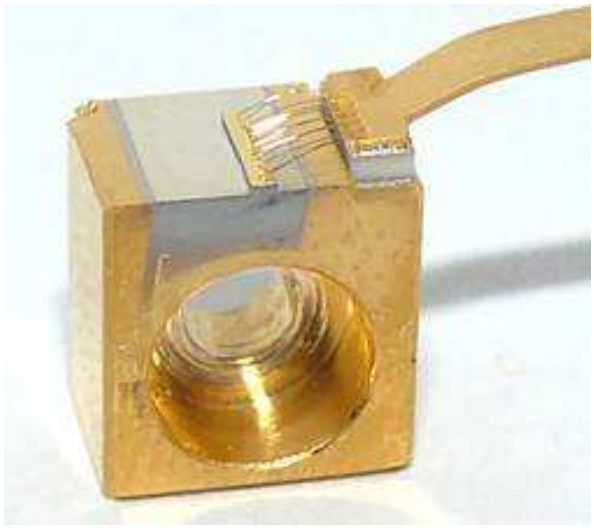

Figure 5-8: QCL C-mount. Image courtesy of Matthew Escarra, Princeton University.

5.3.2 Experimental Setup for Emission Characterization

Once a QCL was cleaved to the desired cavity length and mounted/bonded, it was inserted into a liquid nitrogen (LN_2) cooled cryostat, which allowed for precise heatsink temperature control. Figure 5-9 presents a schematic showing the experimental setup used to characterize the spectral emission.

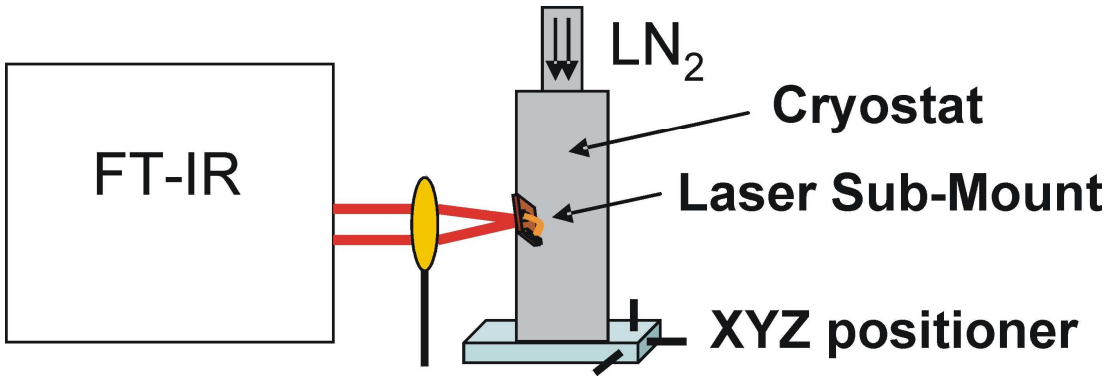

Figure 5-9: Experimental setup for measuring spectral emission with FT-IR.

The QCLs were operated in pulsed mode using a pulse generator with a frequency of 80 kHz, and a pulse width of 100 ns. A bias was applied to each QCL, and was independently measured first by using the XYZ positioner to align radiation emitted into the FT-IR spectrometer. The current was simultaneously measured using a current probe during spectra acquisition. The heatsink temperature was varied between 80 and 300 K by both controlling the flow of LN_2 into the cryostat, and by adjusting a heater. The spectra were then acquired using a LN_2 cooled MCT detector mounted within the FT-IR spectrometer at a spectral resolution of 0.125 cm^{-1} by averaging 10 spectra scans.

5.4 Results and Discussion

5.4.1 Spectra as a Function of Cavity Length

Figure 5-10 depicts FT-IR measured peak emission spectra as wavenumber versus heatsink temperature ranging from 80 to 300 K for various cavity lengths.

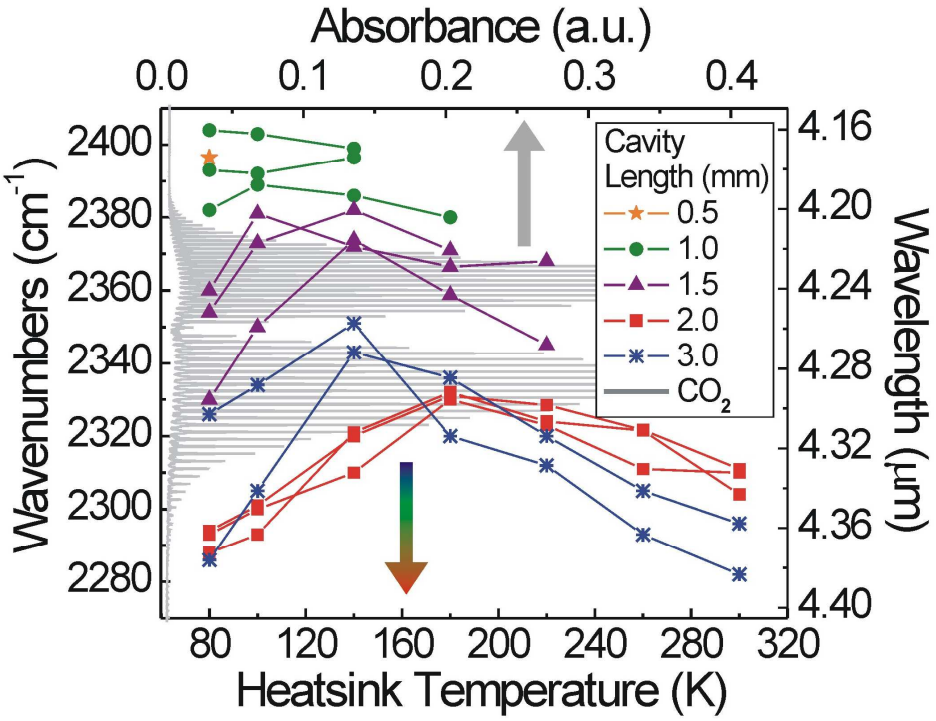

Figure 5-10: Measured emission wavenumber as a function of the heatsink temperature and QCL cavity length.

The emission frequency decreases from 2404 to 2286 cm^{-1}, i.e., by 118 cm^{-1}, with an increase in cavity length from 0.5 to 3 mm. For guidance, a carbon dioxide (CO_2) FT-IR absorbance spectrum is outlined in gray. Evidently, QCLs with cavity lengths of 1.5, 2, and 3 mm directly overlap with strong vibrational-rotational absorption bands CO_2 of at various temperatures.

Similarly, different cavity lengths may be used to deliberately overlap or to avoid overlapping with selected CO_2 features, as shown in Figure 5-11.

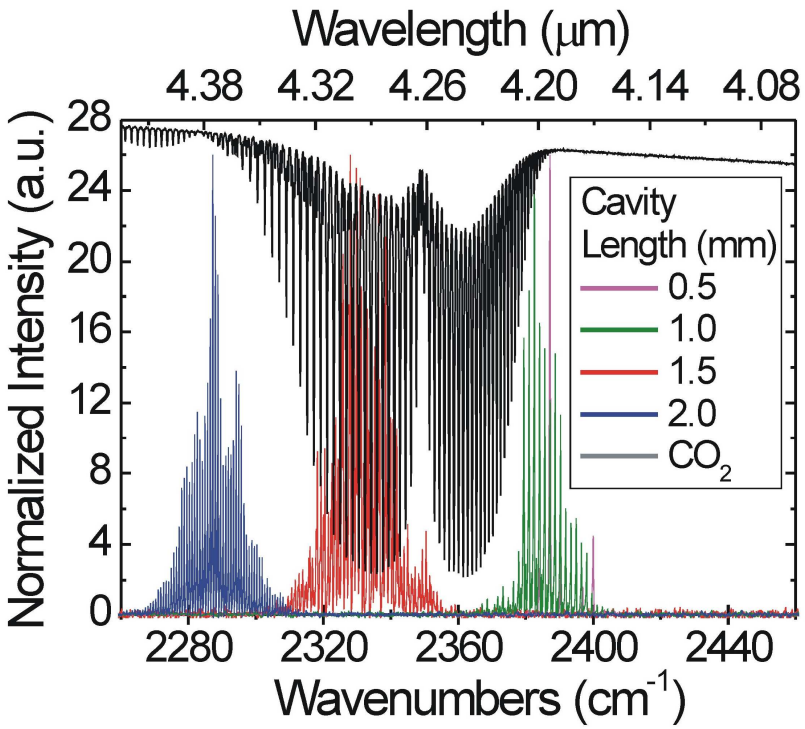

Figure 5-11: QCL emission spectra of four different cavity lengths on and off resonance with carbon dioxide.

It is shown that at constant heatsink temperature cavity lengths in the range of 1 – 2 mm, span across the entire absorption spectrum. Thus, a convenient post-processing strategy for tailoring on and off-resonance QCL emissions is provided, whereby a differential measurement directly yields a quantitative determination of the analyte concentration. All spectra presented in this figure were collected at a heatsink temperature of 80 K.

Figure 5-12 describes the relationship of the emission frequency with the cavity length across a range of heatsink temperatures.

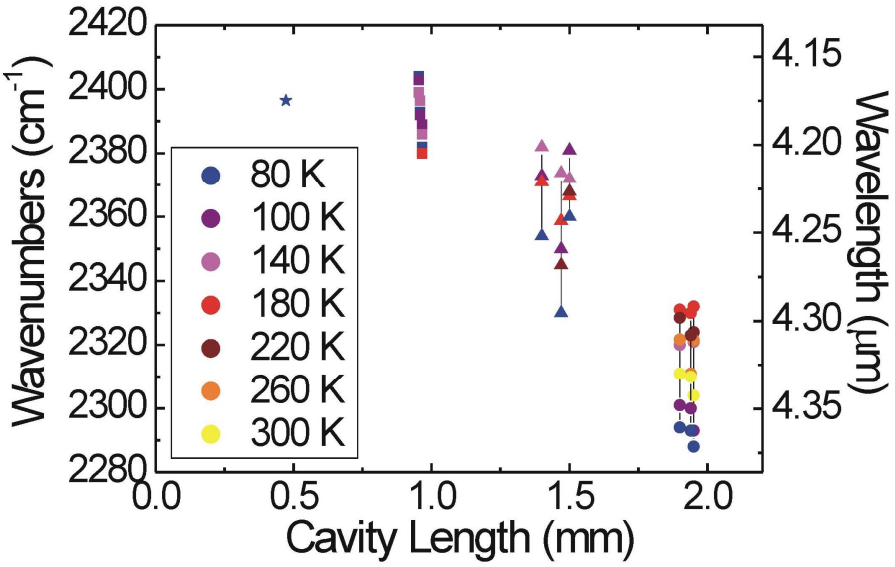

Figure 5-12: Emission wavenumber as a function of the QCL cavity length and heatsink temperature.

The data in this figure further clarifies the ability to systematically select emission frequencies using a range of different cavity lengths.

Lasers with a length of 0.5, 1, and 1.5 mm in Figures 5-10, 5-11, and 5-12 did not fully lase to room temperature due to the higher threshold current density (determined by mirror losses), thereby exceeding the maximum available current density (determined by the doping density). To overcome this limitation, and also to shift emission frequency to directly overlap CO_2 absorption features at higher operating temperatures, the 1 and 1.5 mm lasers described in Figure 5-13 were prepared with a high reflection (HR) coating. It should be noted that HR coating of lasers changes the mirror losses from those expected for a standard laser of that length, and thus result in a shift in wavelength. However, dependence of the cavity length on the threshold voltage is still clearly evident

in the results presented herein, which is in turn itself responsible for a corresponding shift in emission wavenumbers.

5.4.2 Cavity Length and Threshold Voltage

Temperature dependent light-current-voltage (L-I-V) measurements were performed using 100 ns current pulses at a repetition rate of 3 kHz to precisely determine the threshold voltage and the threshold current density. Figure 5-13 represents the relationship between threshold voltage and wavenumbers.

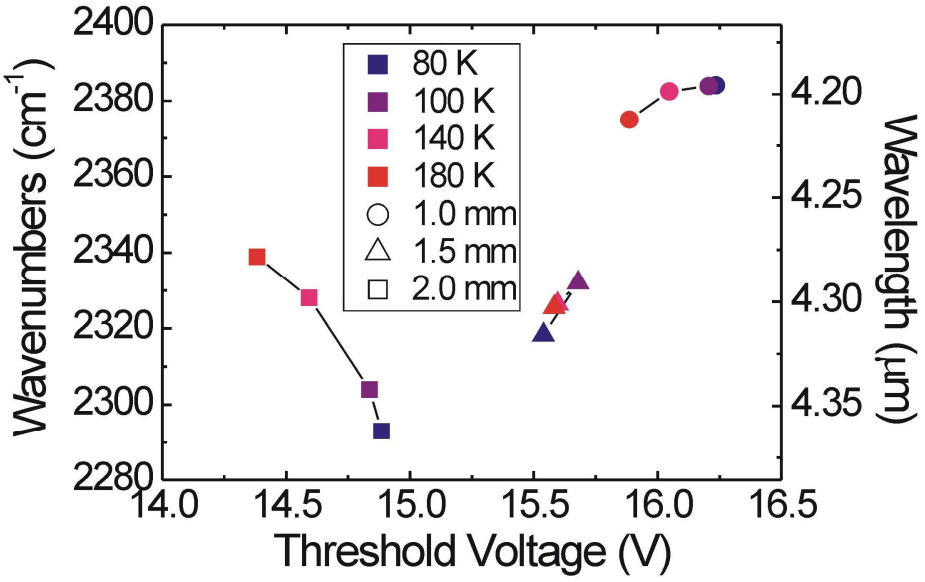

Figure 5-13: Measured emission frequency as a function of threshold voltage for cavity lengths of 1, 1.5, and 2 mm.

From this figure, it is confirmed that the threshold voltage and the spectral emission increase with decreasing cavity length. These experimental results substantiate the calculations provided in Figure 5-3, which suggest an increase in spectral emission

energy with an increasing applied electric field. It should be noted however that the calculations of the Stark effect in QCLs using the full states (see Figure 5-3) usually overestimate the Stark shift, as was also discussed by Yao and coworkers.[13]

Figure 5-14 demonstrates the dependence of the threshold voltage on 1, 1.5, and 2 mm cavity lengths on the heatsink temperatures ranging from 80 to 180 K.

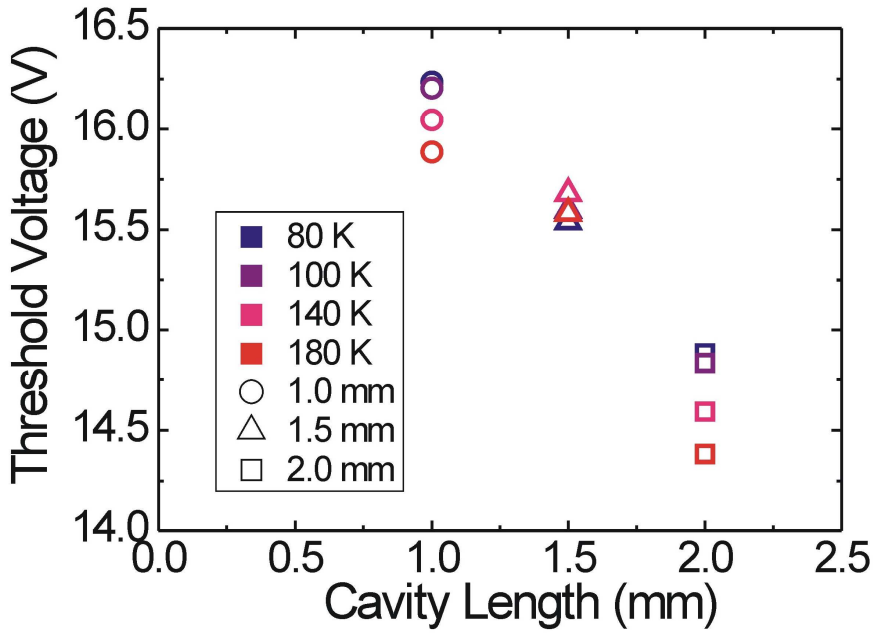

Figure 5-14: Threshold voltage as a function of cavity length and heatsink temperature.

In this graph, it is further shown that shorter cavity lengths have a higher threshold voltage than longer cavity lengths, due to their higher threshold current densities.

Figure 5-15 quantifies this trend with an (L-I-V) plot.

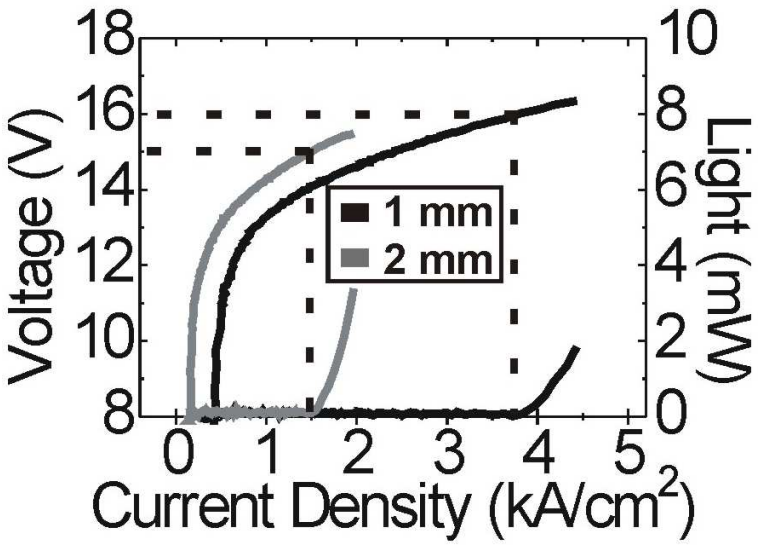

Figure 5-15: Light-current-voltage curves of QCLs with 1 mm (black) and 2 mm (gray) cavity lengths.

Threshold voltages were measured as 16.2 and 14.9 Volts, and threshold current densities as 4.17 and 1.39 kA / cm^2 for 1 and 2 mm cavity lengths, respectively. The difference in threshold voltages as a function of cavity length was calculated to be 1.35 V. Thus, threshold voltages increase with a decrease in cavity length, which consequently results in higher spectral emission frequency due to the increase in electric field.

5.5 Outlook

Future work should be focused on supplementing the accuracy of external cavity tunable quantum cascade lasers to reach the target emission wavelength. Currently, the emission wavelength of a laser chip is designed by adjusting the thickness of quantum heterostructure layers to provide a 3-2 transition energy difference, which would yield an emission wavelength capable of overlapping the absorption peak of a specific analyte. However, the difference between the theoretical emission and actual emission after fabrication of the laser chip may deviate by several hundreds of wavenumbers. This deviation has a direct impact on the ability of the EC-QCL to tune across the analyte absorption peak as the wavelength range is based on tuning across the original laser gain peak. Consequently, to select another wavelength, typically the laser would have to be redesigned, and grown again using MBE. This present cavity length modification technique could be used as a straight-forward post-processing method to deliberately select the laser wavelength prior to integration into an external cavity tuning system, thus enhancing the accuracy of the intended QCL emission wavelength for the target analyte(s).

An additional study should be concentrated on cleaving an array of different cavity lengths onto one chip, ideally with each cavity length being individually biased. Using this approach, wide range tunability in excess of 100 wavenumbers could be achieved on one chip.

5.6 Summary

In this study, deliberate selection of the QCL cavity length has been established as an inexpensive and straightforward QCL wavelength selection technique taking advantage of the electric field and spectral emission dependence on the cavity length, which may be considered a comparatively simple post-processing device parameter. Consequently, the same wafer and the same chip may simply be cleaved to produce a desired emission frequency with high specificity and reproducibility. Varying the cavity length from 0.5 to 3 mm provides a wide spectral emission range of 118 cm^{-1}, which is broad enough to tailor on and off resonances across the entire CO_2 vibrational-rotational absorption bands at 4.3 μm without temperature tuning. Therefore, the proposed strategy appears particularly useful for tailoring the laser emission frequency in chemical sensor applications.

References

[1]C. Young, S.-S. Kim, Y. Luzinova, M. Weida, D. Arnone, E. Takeuchi, T. Day, and B. Mizaikoff, External cavity widely tunable quantum cascade laser based hollow waveguide gas sensors for multianalyte detection. Sensors & Actuators: B. Chemical 140 (2009) 24-28.

[2]C. Young, S.-S. Kim, and B. Mizaikoff, Quantum Cascade Laser Based Gas and Liquid Chemical Sensors. in: M. Lackner, (Ed.), Lasers in Chemistry, Wiley-VCH, Weinhem, 2008.

[3]G.P. Luo, C. Peng, H.Q. Le, S.S. Pei, H. Lee, W.Y. Hwang, B. Ishaug, and J. Zheng, Broadly wavelength-tunable external cavity mid-infrared quantum cascade lasers. IEEE Journal of Quantum Electronics 38 (2002) 486-494.

[4]R. Maulini, M. Beck, J. Faist, and E. Gini, Broadband tuning of external cavity bound-to-continuum quantum-cascade lasers Applied Physics Letters 84 (2004) 1659-1661.

[5]R. Maulini, A. Mohan, M. Giovannini, J. Faist, and E. Gini, External cavity quantum-cascade laser tunable from 8.2 to 10.4 microns using a gain element with a heterogeneous cascade. Applied Physics Letters 88 (2006) 201113/1-201113/3.

[6]C. Peng, G. Luo, and H.Q. Le, Broadband, Continuous, and Fine-Tune Properties of External-Cavity Thermoelectric-Stabilized Mid-infrared Quantum-Cascade Lasers. Applied Optics 42 (2003) 4877-4882.

[7]G. Wysocki, R.F. Curl, F.K. Tittel, R. Maulini, J.M. Bulliard, and J. Faist, Widely tunable mode-hop free external cavity quantum cascade laser for high resolution

spectroscopic applications. Applied Physics B: Lasers and Optics 81 (2005) 769-777.

[8]H.L. Zhang, C. Peng, A. Seetharaman, G.P. Luo, H.Q. Le, C. Gmachl, D.L. Sivco, and A.Y. Cho, External-cavity tunable mid-infrared laser using off-band surface-emitting Bragg grating coupler. Applied Physics Letters 86 (2005) 111112.

[9]B.G. Lee, M.A. Belkin, R. Audet, J. MacArthur, L. Diehl, C. Pflügl, F. Capasso, D.C. Oakley, D. Chapman, A. Napoleone, D. Bour, S. Corzine, and G. Höfler, Widely tunable single-mode quantum cascade laser source for mid-infrared spectroscopy. Applied Physics Letters 91 (2007).

[10]J. Faist, C. Gmachl, F. Capasso, C. Sirtori, D.L. Sivco, J.N. Baillargeon, and A.Y. Cho, Distributed feedback quantum cascade lasers. Applied Physics Letters 70 (1997) 2670-2672.

[11]A. Muller, M. Beck, and J. Faist, Electrically tunable, room-temperature quantum-cascade lasers. Applied Physics Letters 75 (1999) 1509.

[12]C. Young, R. Cendejas, S.S. Howard, W. Sanchez-Vaynshteyn, A.J. Hoffman, K.J. Franz, Y. Yao, B. Mizaikoff, X. Wang, J. Fan, and C.F. Gmachl, Wavelength selection for quantum cascade lasers by cavity length. Applied Physics Letters 94 (2009) 091109-3.

[13]Y. Yao, Z. Liu, A.J. Hoffman, K.J. Franz, and C.F. Gmachl, Voltage Tunability of Quantum Cascade Lasers. IEEE Journal of Quantum Electronics 45 (2009) 730-736.

CHAPTER 6

EC-QCL HWG CHEMICAL SENSORS FOR MULTIANALYTE GAS SENSING

In this chapter, the quantitative detection of ethyl chloride, dichloromethane, and trichloro-methane individually and in mixture is demonstrated using an external cavity broadly tunable quantum cascade laser (EC-QCL) based hollow waveguide gas sensor. Background and spectral characterization of the EC-QCL for chemical sensing applications are also discussed.

6.1 Motivation

As previously mentioned in Chapter 4, FP-QCLs typically provide multimode lasing spectra. Although FP-QCLs are suitable for covering comparatively broad absorptions in condensed phases, they prove less practical for trace gas sensing applications. Usually, gas phase molecules are characterized by very sharp MIR absorption peaks resulting from additional rotational transitions, which are difficult to address individually given the emission characteristics of FP-QCLs. Consequently, decreased sensitivity and selectivity is expected in MIR gas phase absorption spectroscopy due to the multimode nature of the emitted radiation[1] and therefore a means to selectively tune QCL emission to precisely overlap the Q-branch of the analyte is essential. One method to accomplish this objective is through the use of an external cavity[2].

6.2 Background

6.2.1 Introduction and State-of-the-Art

Until recently, QCLs have been limited in their tuning range across molecular absorption features to approximately 3–4 cm^{-1} by adjusting the injection current, or up to approximately 20 cm^{-1} by controlling the temperature of the laser chip[3] (see Chapter 4). However, a wider laser tuning range is desirable for the simultaneous detection of multiple analytes, as encountered in many real-world gas sensing applications.

External cavity tunable quantum cascade lasers (EC-QCL)[4-8] offer a different approach to conventional QCL wavelength tuning yielding a significantly broader tuning range exceeding 100 cm^{-1} [9]. Here, wavelength tuning is provided by coupling radiation emitted from the QCL to an external grating. Consequently, adjusting the angle of the grating results in shifting the location of the resonant peak, thereby enabling to precisely overlap the QCL emission with the maximum of selective analyte absorption features in a broad spectral window for sensitive and selective molecular detection in the gas phase.

While maintaining the merits of fixed wavelength single-mode QCLs, EC-QCLs provide flexible tunability over a considerably broad wavelength window. Luo et al. demonstrated external grating tuning of single-mode QCLs with a tuning range of approximately 54 cm^{-1} (185.2 μm) at a center wavelength of 1961 cm^{-1} (5.1 μm) and at a temperature of 80 K[10]. The tuning range of EC-QCL based on a vertical three-quantum well active region is limited by the relatively narrow gain spectrum. Faist et al. have improved the tuning range of EC-QCLs emitting at approximately 1000 cm^{-1} (10 μm) to

a range of 150 cm^{-1} (66.7 μm) by utilizing a bound-to-continuum active region QCL providing a significantly broadened gain curve compared to vertical three-quantum well active region QCLs[11]. The gain curve of the QCL has been further improved by an active layer structure with inhomogeneous optical transition, whereby each stage of the QCL is designed to emit a photon with a slightly different wavelength. Gmachl and coworkers illustrated this concept by demonstrating an ultrabroadband FP-QCLs with lasing emission covering a range of 1667–1250 cm^{-1} (6–8 μm) resulting from an active layer structure with inhomogeneous optical transition, which opens up the opportunity to establish EC-QCLs with exceptionally wide tuning ranges[12].

To date, EC-QCLs have been tested in a variety of sensing systems providing in part detection limits at the sub-ppb concentration level[13]. Pushkarsky et al. have used EC-QCLs and photoacoustic spectroscopy (PAS) to demonstrate the detection of 2,4,6-trinitrotoluene (TNT) at approximately 0.1 ppb, and acetylene at approximately 2.5 ppb (1σ)[14]. Phillip et al. have used an EC-QCL quartz-enhanced PAS (QEPAS) system utilizing a quartz tuning fork as the transducer to determine the absorption spectra of two gases, pentafluoroethane and 1,1,1,2-tetrafluoroethane, which were in excellent agreement with reference spectra[15]. Likewise, Lewicki et al. have shown trace-gas detection of pentafluoroethane at 3 ppb (1σ), and acetone at approximately 520 ppb (1σ) using EC-QCL QEPAS. Both analytes were also quantitatively determined within a custom gas mixture at concentrations of 47.2 ppm for acetone and 4.4 ppm for pentafluoroethane[9].

The work reported in this chapter discusses a multianalyte sensing capability with a possibly smaller form factor and minute quantity of analyte used. To achieve this, a mid-infrared (MIR) absorption spectroscopy gas phase chemical sensing system with a state-of-the-arts broadly tunable external cavity quantum cascade laser (EC-QCL) and hollow core waveguide (HWG)[16] was used. The HWG simultaneously serves as a waveguide for MIR radiation as well as a miniaturized gas cell[17] with an internal volume on the order of a few milliliters[18]. Additionally, HWGs permit fast response times on the order of a few seconds and yield detection limits in the low ppm to low ppb concentration range[18-22] making these trace gas sensors ideal candidates for applications such as human breath diagnostics.

In the study presented in this thesis, the first EC-QCL based HWG gas sensor was demonstrated for the quantitative detection of individual molecules at trace levels, as well as for the discrimination of structurally related constituents within gas mixtures. A tuning range of ~80 wavenumbers was achieved, effectively providing functionality of a "miniaturized spectrometer" with wide tunability on a compact platform.

6.2.2 EC-QCL Fundamentals

EC-QCLs rely on a wavelength tuning mechanism located outside the cavity where, typically, a grating with first-order direct feedback configuration or Littman–Metcalf configuration is applied. Figure 6-1 describes the difference in lasing characteristics between a typical QCL (top) and that of an EC-QCL (bottom) in greater detail. Here, output is based on a combination of the electroluminescent (EL) characteristics and the

cavity response. In the case of typical FP-QCLs, the cavity response is multimode with no specific frequency selected; therefore, a broad spectral range of different wavelengths across the gain peak is observed in the output characteristics. EC-QCLs, on the other hand, exhibit a cavity response where one wavelength is selected. Changing the angle of an external grating results in a predictable and measurable shift in the location of the resonant peak thereby producing single-mode emission across a range of wavelengths.

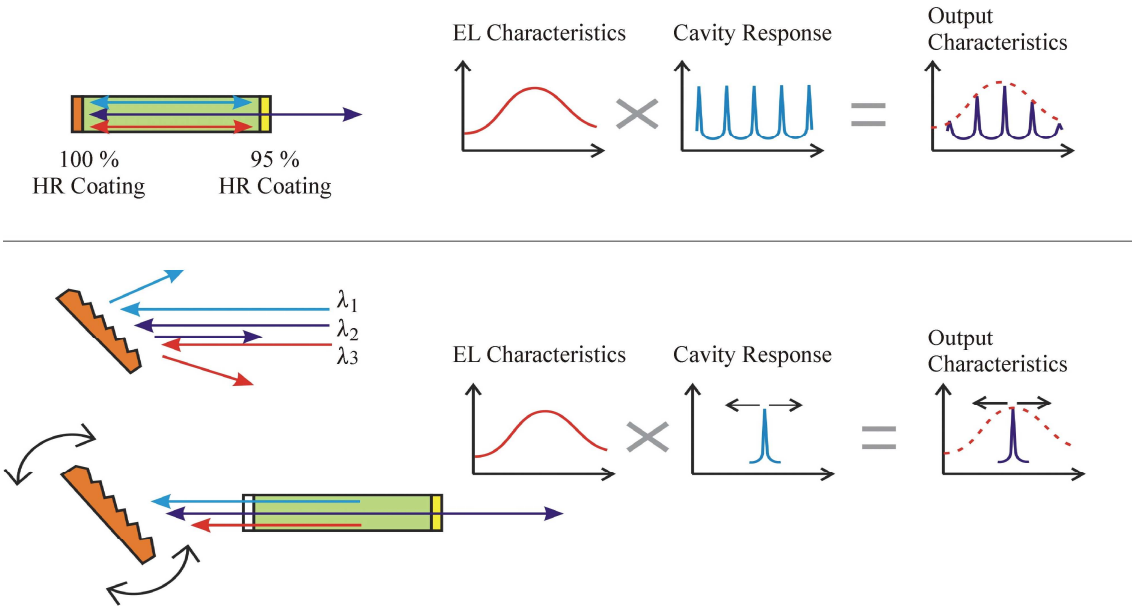

Figure 6-1: Diagram of conventional FP-QCL (top) versus EC-QCL (bottom) lasing characteristics.

6.3 EC-QCL Spectral Characterization

6.3.1 Experimental

Prior to sensing experiments, the spectral emission of the EC-QCL was first characterized using a FT-IR spectrometer. The pulsed EC-QCL (Daylight Solutions, Inc., Poway, CA) described here maintained a relative temperature of 0 degrees Celsius, a pulse width of 0.50 μs, a frequency of 100.0 kHz, a duty cycle of 5 %, and current was set to 1500 mA. Figure 6-2 presents a schematic of the experimental setup used to characterize EC-QCL emission. A gold coated off-axis parabolic mirror (OAPM) was used to focus the emitted radiation into the external port of a Bruker IFS 66 (Bruker Optics, Inc., Billerica, MA) Fourier transform infrared (FT-IR) spectrometer utilizing a liquid-nitrogen–cooled mercury–cadmium-telluride (MCT) detector (detector element: 1 mm × 1 mm, detectivity: $D^*=3\times10^{10}$ $cmHz^{1/2}W^{-1}$, model: FTIR-16-1.0, InfraRed Associates, Inc., Stuart, FL). The laser was external cavity tuned across a range of 1297–1219 cm^{-1} at a spectral resolution of 1 cm^{-1}, and spectra were collected averaging 10 scans per measurement at a spectral resolution of 0.25 cm^{-1} across a spectral range of 4000–400 cm^{-1} using the Blackman–Harris 3-term apodization function. In a separate measurement, the laser was refocused directly onto the same MCT detector to determine the output voltage evaluated with an oscilloscope (TDS3032, Tektronix, Beverton, OR).

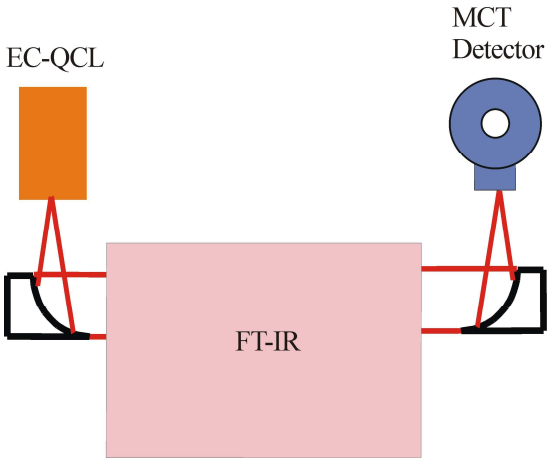

Figure 6-2: Schematic of experimental setup for FT-IR spectral characterization of EC-QCL emission.

6.3.2 Results and Discussion

Figure 6-3a shows the characterization of the EC-QCL emission with optical output power as a function of the emission frequency.

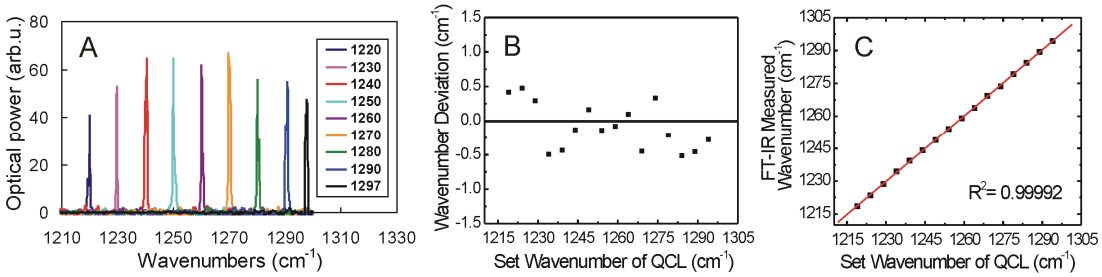

Figure 6-3: FT-IR characterization of EC-QCL emission: (A) Raw data FT-IR spectra over a range of wavenumbers. (B) Calculated deviation of set wavenumber from measured wavenumber. (C) Correlation between measured emission versus expected emission.

As expected, the optical power decreases with increasing deviation from the native central emission frequency of the laser (1258cm^{-1}). The deviation between the selected laser emission frequency and the measured emission frequency was determined to be below ± 0.5 cm^{-1} of the selected EC-QCL emission frequency, as described in Figure 6-3b. Figure 6-3c depicts the correlation between expected and actual EC-QCL emission frequency. These performance parameters are essential for trace-gas sensing applications, as absorption lines may exhibit comparatively narrow bandwidths, thereby demanding precise overlap of the QCL emission frequency for ensuring maximized sensitivity and selectivity[2].

6.4 EC-QCL Univariate Calibration

6.4.1 Experimental

After EC-QCL spectral characterization, experiments were focused on univariate calibration of the EC-QCL HWG trace gas sensor using exponential dilution. A picture of the experimental sensing setup including exponential dilution is presented in Figure 6-4.

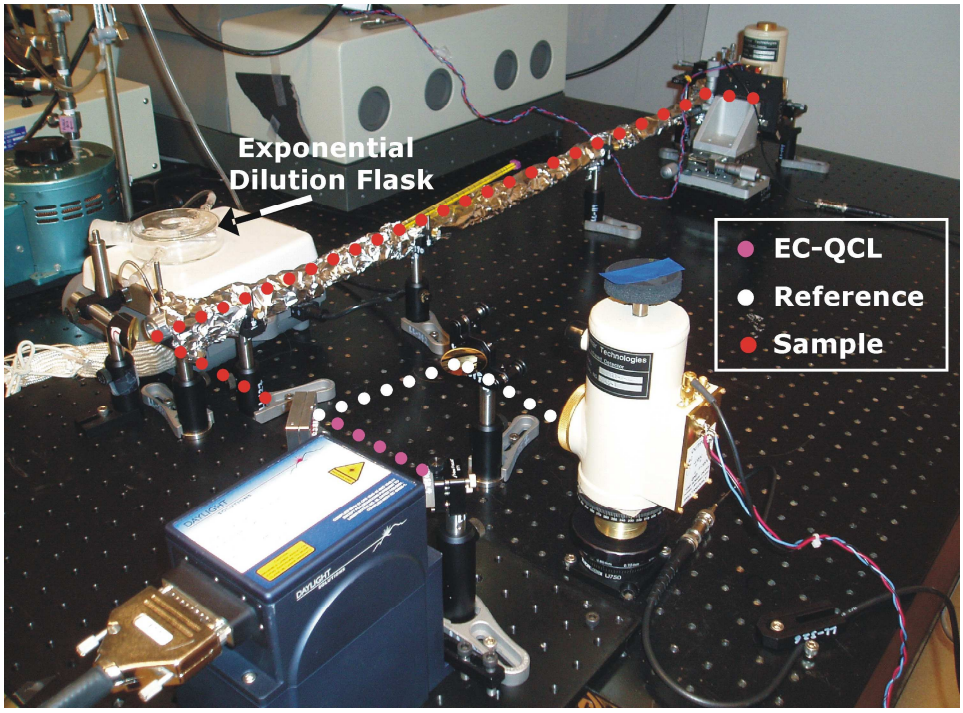

Figure 6-4: EC-QCL HWG trace gas sensor experimental setup.

Radiation from the EC-QCL was focused into a custom-made hollow waveguide gas cell using two OAPMs. The hollow waveguide is a structural silica tube internally coated with an IR-reflective Ag/AgI layer. After absorption, radiation was then focused onto a liquid-nitrogen cooled MCT detector. A reference beam was generated by using a beamsplitter prior to focusing radiation into the hollow waveguide, and via an additional MCT detector, thereby allowing for signal normalization compensating for e.g., fluctuations in optical power as a function of frequency.

Gas samples were prepared by exponential dilution, and directly introduced into the EC-QCL HWG gas sensor, as previously demonstrated[18]. Nitrogen was used as inert carrier

gas at flow rates in the range of 8–42 mL/min depending on the tested analyte, however, remained constant throughout an individual measurement.

6.4.2 Results and Discussion

Univariate calibration of the gas sensing system was performed using exponential dilution, which is a commonly accepted method for preparing trace-level sample dilutions e.g., for calibrating gas chromatographs[23]. Using this procedure, the limit of detection for three individual analytes was determined at 1287.25 cm^{-1} for ethyl chloride, 1262 cm^{-1} for dichloromethane, and 1220 cm^{-1} for trichloromethane, respectively.

Exponential dilution theory enables that at any given point of time the instantaneous concentration of analyte can be calculated if the initial concentration, the volume of the dilution flask, and flow rate of carrier gas are known as follows:

$$C = C_0 e^{-\alpha t} \qquad \text{(Eqn 6.1)}$$

where C is the calculated instantaneous concentration of the analyte, C_0 is the initial concentration of the analyte, α is flow rate of the carrier gas divided by the volume of the dilution flask, and t is the time at which the concentration is calculated during exponential dilution[23]. Practically, a known amount of analyte is injected into the exponential dilution flask[24], while a stir bar constantly and continuously mixes and dilutes the analyte gas with the carrier gas at a constant flow rate as described in Figure 6-5 below.

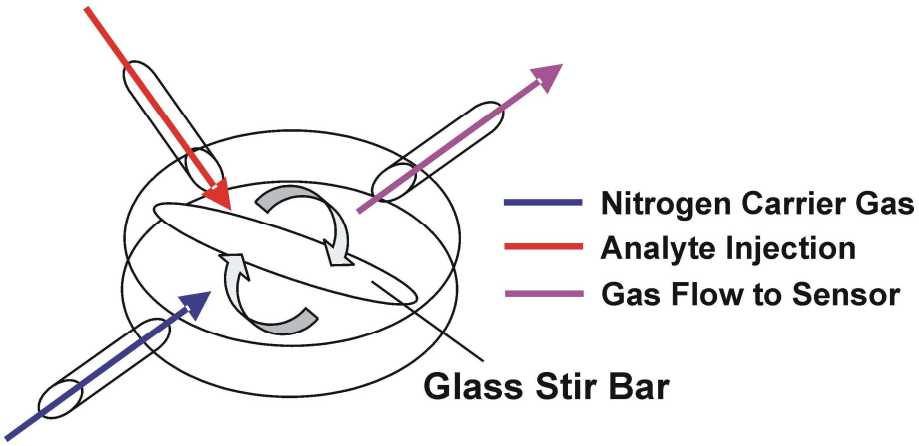

Figure 6-5: Exponential dilution flask diagram.

The limit of detection for this sensing system was derived from the smallest detectable analyte concentration using exponential dilution theory, which could be discriminated against the background noise level. Typical results for such exponential dilution experiments indicating the recovery of the background signal, as the analyte is increasingly diluted within the HWG gas cell are given in Figure 6-6.

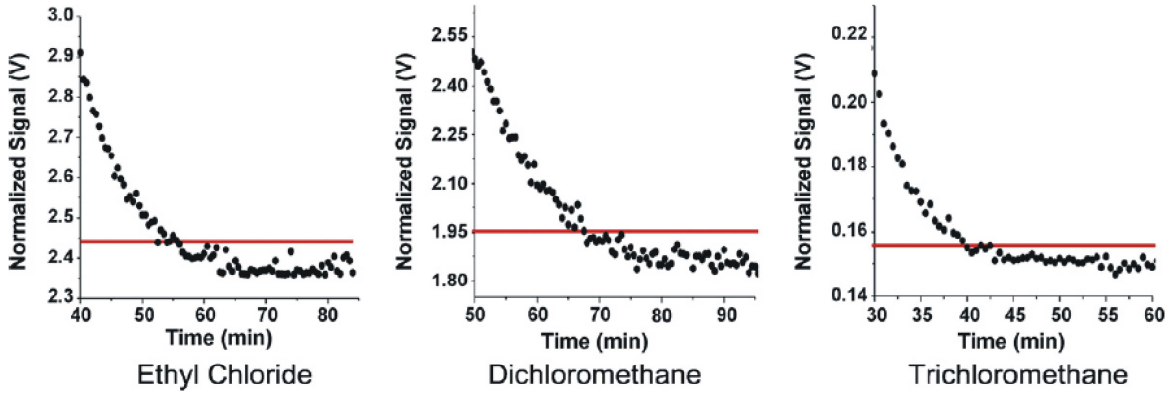

Figure 6-6: Exponential dilution of ethyl chloride, dichloromethane, and trichloromethane. The red line indicates the noise level derived as noise average + 3σ.

For experiments of individual gases, the EC-QCL was tuned to the center Q-branch of the CH_2 wagging mode for each analyte. Efficient overlap of the laser emission with the appropriate analyte absorption yielded limits of detection (according to the 3σ criteria) at 4 ± 3 ppb for ethyl chloride, 7 ± 6 ppm for dichloromethane, and 11 ± 15 ppb for trichloromethane, respectively[2].

6.5 EC-QCL Multivariate Calibration

6.5.1 Experimental

For the determination of multivariate calibration samples, gas mixtures were prepared in sealed volumetric flasks, and injected into the hollow waveguide via needle valves available at the custom gas cells sealing off the HWG at both ends. While tuning the EC-QCL across its frequency range, molecularly selective damping of the laser radiation was determined as a function of decrease in voltage using an oscilloscope at a spectral resolution of 1 cm^{-1}.

6.5.2 Results and Discussion

Figure 6-7 shows an exemplary spectrum of a mixture containing the three analytes, as recorded with the EC-QCL HWG gas sensor.

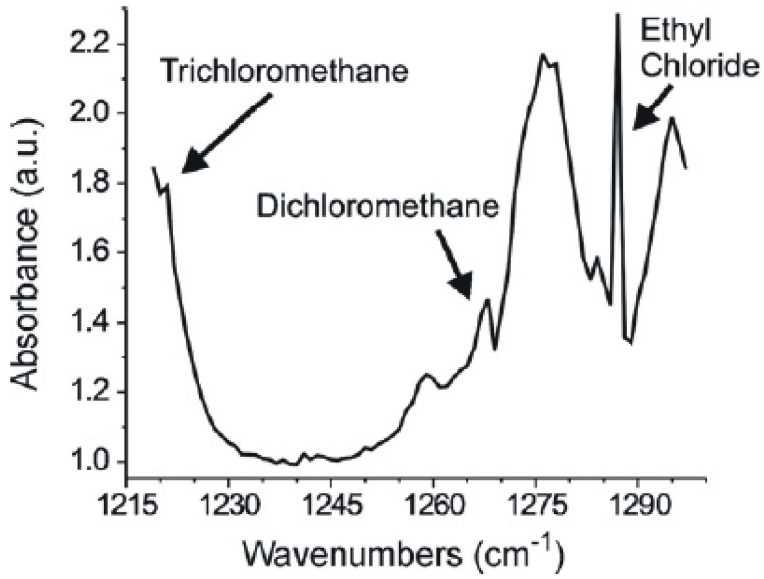

Figure 6-7: Spectrum of all three analytes within a gas mixture recorded with EC-QCL HWG gas sensor.

As any changes of the hollow waveguide response function and fluctuations in optical power are taken into account during absorption experiments, distinct and selective vibrational features of all three analyte are discriminated within the wavelength tuning range of a single EC-QCL.

Quantitative multivariate data analysis of gas mixtures was demonstrated by using a partial least squares (PLS) model, which was built on a limited data set of manually prepared gas standards prepared by an experimental design approach for deliberately varying the concentrations per calibration sample while avoiding collinearity. The training set consisted of 11 calibration samples, each comprising all three analytes present within concentrations ranges: ethyl chloride 2000–9000 ppm, dichloromethane 30–70 ppm, and trichloromethane 40–100 ppm. The multivariate calibration model was built using PLS toolbox (Eigenvector Research, Inc.,Wenatchee, WA). The prediction capability of the model was tested using cross validation with each calibration sample randomly left out once and treated as quasi-unknown, after the model was generated using autoscaling for data preprocessing and selecting seven latent variables. The results are shown in Figure 6-8. Validation of the model resulted in a coefficient of determination of 0.977, and a root mean square error of calibration of 1.294 for predicting the dichloromethane concentration within such gas mixtures characterized by considerable peak overlap between the constituents.

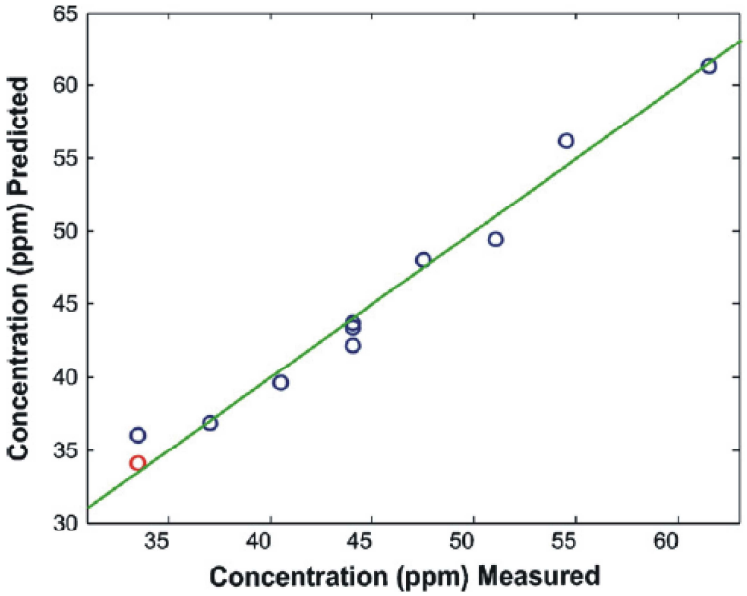

Figure 6-8: PLS model validation for predicting the concentration of dichloromethane in mixture. The blue circles denote standards used to build the model. The red circle represents the standard left out as quasi unknown and the predicted value based on the established model.

It is expected that the robustness of the PLS model will further improve by substantially expanding the calibration data set using automated gas mixing routines[2].

6.6 Summary and Outlook

Sensitive and selective trace gas detection of ethyl chloride, dichloromethane, and trichloromethane were demonstrated using an external cavity tunable quantum cascade laser hollow waveguide gas sensor tuned to the maximum absorption feature of each analyte. Gas mixtures were analyzed via a partial least squares model using the hollow waveguide as a miniaturized gas cell and tuning the EC-QCL across the frequency range

from 1297 cm^{-1} to 1219 cm^{-1} at a spectral resolution of 1 cm^{-1}. As the development of QCL chips toward longer wavelengths progresses, it is anticipated that a wide range of relevant gaseous analytes could be determined with such compact gas sensing systems[2].

References

[1]C. Young, S.-S. Kim, and B. Mizaikoff, Quantum Cascade Laser Based Gas and Liquid Chemical Sensors. in: M. Lackner, (Ed.), Lasers in Chemistry, Wiley-VCH, Weinhem, 2008.

[2]C. Young, S.-S. Kim, Y. Luzinova, M. Weida, D. Arnone, E. Takeuchi, T. Day, and B. Mizaikoff, External cavity widely tunable quantum cascade laser based hollow waveguide gas sensors for multianalyte detection. Sensors & Actuators: B. Chemical 140 (2009) 24-28.

[3]A. Kosterev, G. Wysocki, Y. Bakhirkin, S. So, R. Lewicki, M. Fraser, F. Tittel, and R.F. Curl, Application of quantum cascade lasers to trace gas analysis. Applied Physics B: Lasers and Optics 90 (2008) 165-176.

[4]R. Maulini, A. Mohan, M. Giovannini, J. Faist, and E. Gini, External cavity quantum-cascade laser tunable from 8.2 to 10.4 microns using a gain element with a heterogeneous cascade. Applied Physics Letters 88 (2006) 201113/1-201113/3.

[5]R. Maulini, A. Yarekha Dmitri, J.-M. Bulliard, M. Giovannini, J. Faist, and E. Gini, Continuous-wave operation of a broadly tunable thermoelectrically cooled external cavity quantum-cascade laser. Optics letters 30 (2005) 2584-6.

[6]M. Pushkarsky, M. Weida, T. Day, D. Arnone, R. Pritchett, D. Caffey, and S. Crivello, High-power tunable external cavity quantum cascade laser in the 5-11 micron regime. Proceedings of SPIE 6871 (2008) 68711X/1-68711X/8.

[7]M.J. Weida, D. Arnone, and T. Day, Tunable QC laser opens up mid-IR sensing applications. Laser Focus World 42 (2006) S13-S14.

[8]G. Wysocki, R.F. Curl, F.K. Tittel, R. Maulini, J.M. Bulliard, and J. Faist, Widely tunable mode-hop free external cavity quantum cascade laser for high resolution spectroscopic applications. Applied Physics B: Lasers and Optics 81 (2005) 769-777.

[9]R. Lewicki, G. Wysocki, A.A. Kosterev, and F.K. Tittel, QEPAS based detection of broadband absorbing molecules using a widely tunable, cw quantum cascade laser at 8.4 μm. Optics Express 15 (2007) 7357-7366.

[10]G.P. Luo, C. Peng, H.Q. Le, S.S. Pei, H. Lee, W.Y. Hwang, B. Ishaug, and J. Zheng, Broadly wavelength-tunable external cavity mid-infrared quantum cascade lasers. IEEE Journal of Quantum Electronics 38 (2002) 486-494.

[11]R. Maulini, M. Beck, J. Faist, and E. Gini, Broadband tuning of external cavity bound-to-continuum quantum-cascade lasers Applied Physics Letters 84 (2004) 1659-1661.

[12]C. Gmachl, D.L. Sivco, R. Colombelli, F. Capasso, and A.Y. Cho, Ultra-broadband semiconductor laser. Nature 415 (2002) 883-887.

[13]M. Pushkarsky, A. Tsekoun, I.G. Unayevskiy, R. Go, and C.K.N. Patel, Sub-parts-per-billion level detection of NO_2 using room-temperature quantum cascade lasers. Proceedings of the National Academy of Sciences of the United States of America 103 (2006) 10846-10849.

[14]M.B. Pushkarsky, I.G. Dunayevskiy, M. Prasanna, A.G. Tsekoun, R. Go, and C.K.N. Patel, High-sensitivity detection of TNT. Proceedings of the National Academy of Sciences of the United States of America 103 (2006) 19630-19634.

[15]M.C. Phillips, T.L. Myers, M.D. Wojcik, and B.D. Cannon, External cavity quantum cascade laser for quartz tuning fork photoacoustic spectroscopy of broad absorption features. Optics Letters 32 (2007) 1177-1179.

[16]J.A. Harrington, A review of IR transmitting, hollow waveguides. Fiber and Integrated Optic 19 (2000) 211-227.

[17]F. de Melas, V.V. Pustogov, N. Croitoru, and B. Mizaikoff, Development and optimization of a mid-infrared hollow waveguide gas sensor combined with a supported capillary membrane sampler. Applied Spectroscopy 57 (2003) 600-606.

[18]C. Charlton, B. Temelkuran, G. Dellemann, and B. Mizaikoff, Midinfrared sensors meet nanotechnology: Trace gas sensing with quantum cascade lasers inside photonic band-gap hollow waveguides. Applied Physics Letters 86 (2005) 194102/1-194102/3.

[19]C. Charlton, F. de Melas, A. Inberg, N. Croitoru, and B. Mizaikoff, Hollow-waveguide gas sensing with room-temperature quantum cascade lasers. IEE Proceedings: Optoelectronics 150 (2003) 306-309.

[20]C. Charlton, A. Inberg, N.I. Croitoru, and B. Mizaikoff, Hollow waveguide infrared gas sensing for biomedical applications. Proceedings of SPIE-The International Society for Optical Engineering 4957 (2003) 116-123.

[21]C. Charlton, B.T. Thompson, and B. Mizaikoff, Hollow waveguide infrared spectroscopy and sensing. in: G. Orellana, and M.C. Moreno-Bondi, (Eds.), Springer Series on Chemical Sensors and Biosensors, Springer-Verlag, Heidelberg, 2005, pp. 133-167.

[22]L. Hvozdara, S. Gianordoli, G. Strasser, W. Schrenk, K. Unterrainer, E. Gornik, C.S.S.S. Murthy, M. Kraft, V. Pustogow, B. Mizaikoff, A. Inberg, and N. Croitoru, Spectroscopy in the gas phase with GaAs/AlGaAs quantum-cascade lasers. Applied Optics 39 (2000) 6926-6930.

[23]J.E. Lovelock, Ionization methods for the analysis of gases and vapors. Analytical Chemistry 33 (1961) 162-78.

[24]H. Nozoye, Exponential Dilution Flask. Analytical Chemistry 50 (1978) 1727.

CHAPTER 7

CONCLUSIONS AND OUTLOOK

The objective of this thesis was to develop possibly compact trace gas sensors for BTX analysis using mid-infrared spectroscopic and sensing techniques. Studies with FT-IR spectroscopy established direct sensing of ppm BTX with a 39 second response time, and ppb detection limits by combination with a preconcentration / thermal desorption step. Furthermore, first steps in transitioning such sensing systems from portable yet benchtop sized sensor platforms to hand-held QCL-based devices taking advantage of such miniaturized light sources in trace gas sensing were investigated. Variation of the QCL cavity length resulted in a novel wavelength selection technique offering a tailoring range for the emission wavelength across one hundred wavenumbers, which was demonstrated to be wide enough to cover an entire IR absorption feature of CO_2. Furthermore, EC-QCL based HWG sensors have been applied demonstrating multianalyte trace gas sensing both for individual components and within ternary mixtures.

In an effort outlining potential next-generation hand-held IR trace gas sensors for BTX, this chapter discusses further reduction of the sensor form factor, as well as the current limitations in developing QCLs lasing at longer wavelengths, i.e. the fingerprint region, which is essential for more compact BTX sensing devices.

7.1 Reducing the Sensor Footprint: Bending Losses in Coiled HWGs

7.1.1 Motivation

The hollow waveguides utilized in the experiments presented in this thesis ranged in length from 50 – 100 cm. It is anticipated that the achievable limits of detection could be further improved by one order of magnitude by increasing the length of the waveguide to 10 or more meters; however, for practical applications as a portable sensing device and for attaining acceptable dimensions, it is required that the waveguide is coiled.[1]

To date, there are two types of hollow waveguides that can be used for trace gas sensing, both of which are discussed here: conventional (Ag/AgI)[2] HWGs, and photonic bandgap (PBG) HWGs.[3] Bending losses in conventional hollow waveguides[4-8] and in photonic bandgap waveguides[3] have previously been extensively studied during separate investigations; however, a direct comparison study between these two different types of HWGs has not been reported to date for the purpose of optimizing gas sensors based on these waveguiding structures. The purpose of this section is to present first systematic studies on bending losses for conventional and PBG HWGs leading to optimized configurations for next-generation QCL–based HWG gas sensors.

7.1.1.2 Conventional and Photonic Bandgap Hollow Waveguides

As discussed in Chapter 1, conventional hollow waveguides are internally coated with an Ag layer, and a thin protective layer of AgI to propagate radiation via metallic reflection inside the hollow core from the light source to the detector. PBG HWGs guide radiation via different propagation mechanisms, i.e. radiation is confined and transported only

within the optical bandgaps resulting from periodic structures along the radial direction of the PBG HWG. The photonic bandgap material consists of alternating thin layers of glass and a polymer, thus generating an appropriate refractive index contrast. The outer cladding layer of PBG HWGs is made of polymer material, thus offering superior flexibility and robustness; in contrast, conventional HWGs are mainly fabricated from silica structural tubings. In contrast to PBG HWGS, conventional hollow waveguides fracture and break easily upon bending to small radii of curvature (< 30 cm). Furthermore, PBG HWGs support radiation propagation by omnidirectional reflection in a frequency-selective fashion, thereby facilitating sensing with high signal-to-noise ratio within confined spectral regimes.

7.1.1.3 Reducing the Dimension of IR Sensor Platforms

Figure 7-1 illustrates the difference between the sensor platform presented in the chemical sensing studies of this thesis versus a platform at reduced dimensions using coiled HWGs.

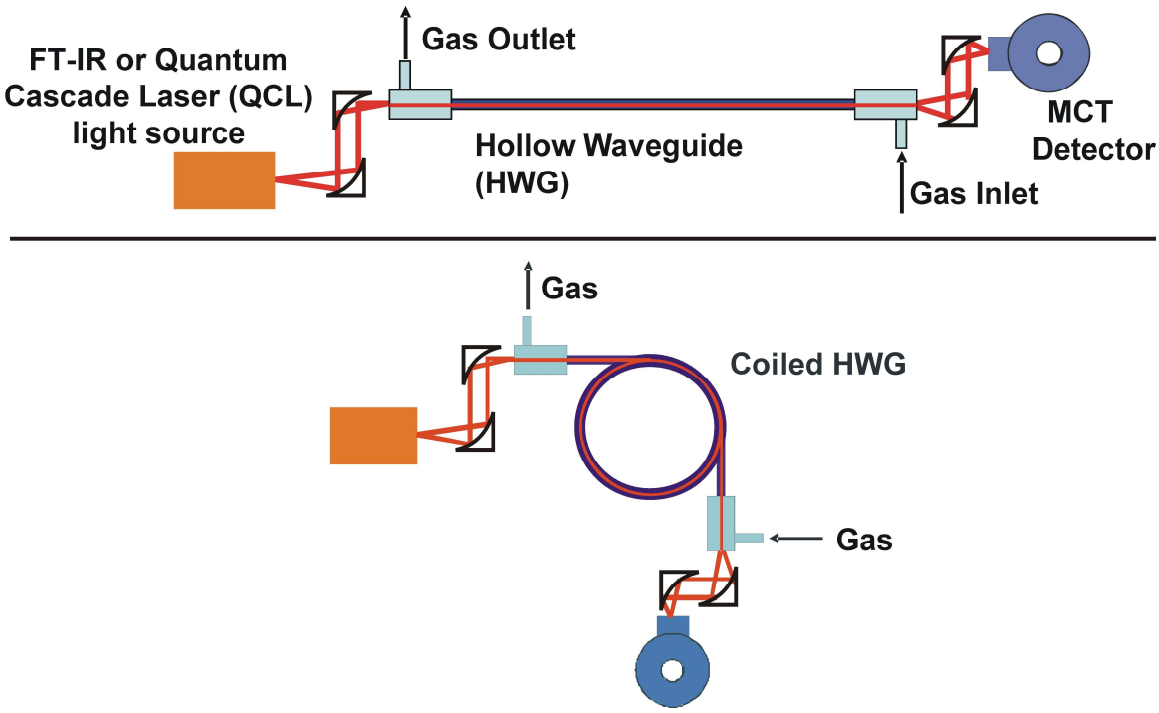

Figure 7-1: Illustration of sensor platforms based on straight HWGs (top) and coiled HWGs (bottom).

As evident in Figure 7-1, the sensor footprint and form factor may be greatly reduced depending on the HWG radius of curvature. HWG bending loss measurements in the following sections will focus on the experimental setup presented in Figure 7-1 (bottom).

7.1.2 Experimental

7.1.2.1 Quantum Cascade Laser Equipment

The laser used in these experiments was a pulsed distributed feedback quantum cascade laser operating at 971 cm^{-1} (SPECDILAS® Q-970-GMP-MTE, Laser Components GmbH). The QCL was operated at a pulse width of 300 ns, a repetition rate of 1 kHz, and at a temperature of 5 °C. The detector used to evaluate radiation emanating from the

distal end of the waveguide was a liquid nitrogen- cooled mercury-cadmium-telluride (MCT) detector (detector element: 1x1 mm, detectivity D* = 3 x 10^{10} cm $Hz^{1/2}W^{-1}$, model KMPV 11-1-LJ2, Kolmar Technologies, Newburyport, MA). An oscilloscope was used for resolving the signal and for data acquisition (TDS 3032, Tektronix, Beverton, OR). A total of 512 curves were averaged for each recorded signal.

7.1.2.2 FT-IR Equipment

A Bruker Equinox 55 Fourier-transform infrared spectrometer (Bruker Optics, Inc., Billerica, MA) was used. Spectra were recorded at 2 cm^{-1} spectral resolution averaging 100 spectra scans per measurement in a spectral range of 400 - 4000 cm^{-1} using the Blackman-Harris 3-term apodization function. The detector applied to collect transmitted broadband radiation was a liquid-nitrogen-cooled mercury-cadmium-telluride (MCT) detector (detector element: 1x1 mm, detectivity D* = 3 x 10^{10} cm $Hz^{1/2}W^{-1}$, model FTIR-16-1.0, InfraRed Associates, Inc. Stuart, FL).

7.1.2.3 Hollow Waveguide

A conventional hollow waveguide (Ag/AgI internally coated) was cut to a length of 213 cm using a ceramic cutting blade. The HWG had an internal diameter of 750 μm (Polymicro Technologies, LLC, Phoenix, Arizona). The photonic bandgap hollow waveguide (Omniguide Communications Inc.) with an internal diameter of 700 μm was cut to the same length as the conventional HWG. During loss studies, the waveguides were fixed at both ends with male FC termination connectors, which were coupled to mechanical mounting fixtures.

7.1.3 Measurement Procedure

The overall experimental setup is presented in Figure 7-2.

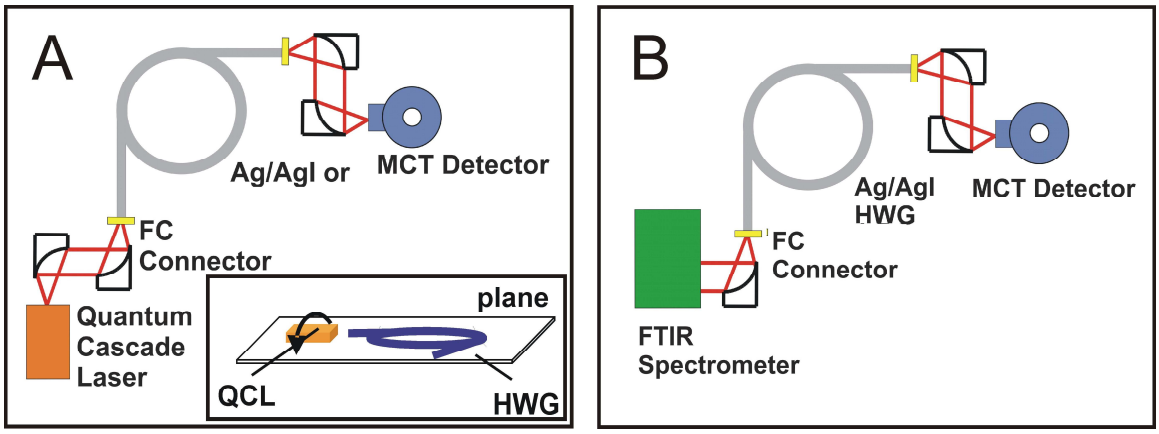

Figure 7-2: Experimental setup for bending losses using QCL (A), QCL polarization, (inset), and using FT-IR (B).

Hollow waveguides were first aligned in a straight configuration for providing maximum signal throughput without saturating the detector. Off-axis parabolic mirrors (OAPMs) with a focal length of 2.54 cm were applied to focus the laser radiation into the hollow waveguide (conventional HWG or PBG HWG). One off-axis parabolic mirror with a focal length of 12.5 cm was used to focus collimated broadband radiation from the external port of the FT-IR spectrometer into the input side of the conventional HWG.

Radiation was focused onto the detector after transmission through the waveguide using two OAPMs. The optical alignment was not changed throughout the entire experiment to ensure that the only variable parameter was the bending radius of curvature of the waveguide. The detector signal was recorded first in the bent waveguide configuration

followed by the straight waveguide position. This procedure was performed for both the conventional and the photonic bandgap waveguides with the quantum cascade laser light source, and with the conventional HWG in addition using the FT-IR spectrometer. Waveguides were coiled around diameters of 13.5, 16, 21, 26.8, and 36.7 cm; the experiments were repeated three times each keeping the bent section of the waveguide constant at a length of 152 cm, and the straight section of the waveguide constant at 30 cm before and after the bended section. In the case of QCL measurements, the laser was rotated by 90 degrees clockwise to change the polarization status of the emitted radiation as visualized in the inset of Figure 7-2A. The nomenclatures "parallel" and "perpendicular" in the following section indicate the relative relationship between the polarization direction of the laser radiation and the plane of bending. The plane of bending is defined as the plane where the coiled waveguide exists.

7.1.4 Results and Discussion

7.1.4.1 Bending Losses in HWGs using a QCL

The total relative waveguide loss is considered as the logarithmic ratio of optical throughput signal in the straight waveguide position versus the bent waveguide position. Figure 7-3 depicts this relationship as a function of coil diameter.

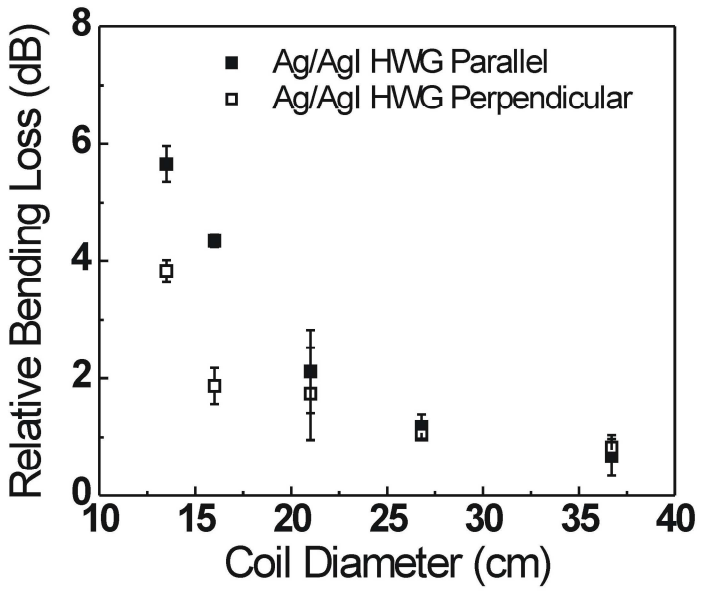

Figure 7-3: Experimentally determined total loss in conventional and photonic bandgap waveguides using a quantum cascade laser.

Total bending losses increase as the coiling radii get smaller for both types of HWGs. It was also found that coiling waveguides parallel to the polarization direction of the radiation results in more losses for both types of HWGs. Radiation emitted from the QCL is polarized, and the direction of polarization can be selected depending on the mounting position of the laser chip inside the housing; accordingly, the high and low loss plane may be interrogated by rotating the laser chip by 90 degrees. In case of the low loss plane, the PBG HWG loss value of 1.27 dB for a 21 cm coil diameter compares well with the previously reported literature value of approximately 1.05 dB[3] at the same radius of curvature for a 90 degree bend. This comparison results from dividing the total relative bending loss in the coil diameter by the number of coils for deriving the loss per 90 degree bend.

7.1.4.2 Bending Losses in HWGs using FT-IR

The same procedure was performed for conventional hollow waveguides coupling broadband radiation from a Fourier-transform infrared spectrometer into the waveguide, however, without particular polarization of the emitted radiation. Figure 7-4 displays transmission spectra through straight and coiled Ag/AgI internally coated hollow waveguides.

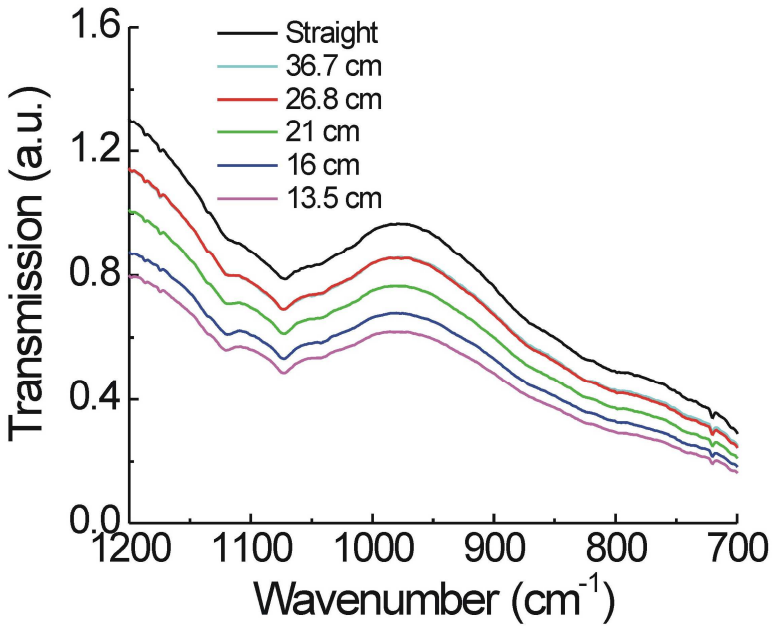

Figure 7-4: FT-IR-based transmission measurements of Ag/AgI coiled hollow waveguides.

The evaluation of curved versus straight waveguide transmission spectra after calculating the bending loss is plotted in Figure 7-5.

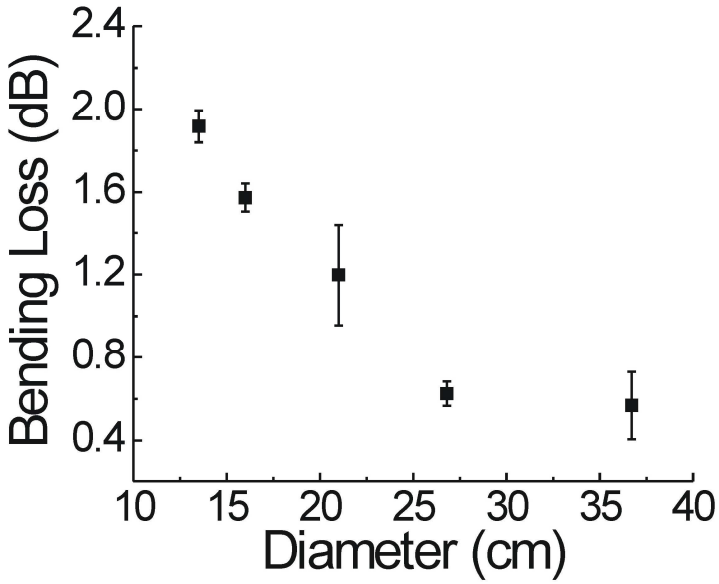

Figure 7-5: FT-IR-based measurements of bending losses inside conventional hollow waveguides versus the coil diameter.

It was found that propagation losses in coiled conventional hollow waveguides are similar to - but somewhat less - using broadband radiation as opposed to QCL radiation, where the range of QCL bending losses in parallel polarization amounts approximately 0.68-5.65 dB, and the range of FT-IR-determined bending losses approximately 0.56 dB – 1.91 dB. The discrepancy between these two ranges may result from different coupling conditions into the hollow waveguide structure, and should be investigated during future studies.

The transmission window at a specific wavelength is particularly important for FT-IR-based HWG gas sensing. Conventional hollow waveguides propagate broadband infrared radiation; however, optical transparency is not uniform throughout the mid-infrared spectral regime (typically 4000-400 cm^{-1}). The internal dielectric coating thickness may

be altered to optimize transmission for a particular wavelength[2]. The achievable limit of detection for a HWG-based gas sensing device relies on the frequency position of the absorption wavelength of a particular analyte weighed against the achievable signal-to-noise ratio, and given the attenuation of the waveguide within the relevant wavelength band.

7.1.5 Outlook and Conclusions

In this study, bending losses for different radii of curvature for conventional HWGs and PBG HWGs were determined with two different types of radiation sources, i.e. QCLs lasing at 10.3 μm, and broadband mid-infrared radiation provided by a FT-IR spectrometer. Relative bending losses for both waveguides were studied with polarized QCL radiation and broadband FT-IR radiation. The research goal of these studies is taking advantage of an increased interaction path length utilizing coiled HWG configurations without trading-off the compact form factor of HWG-based sensing systems. Studies on the bending losses for a variety of HWG materials will provide the fundamental information for optimizing the bending radius and the ratio between straight sections versus bent sections for future miniaturized gas sensor design.

Additionally, future research in this area should be focused on FT-IR-based studies with PBG HWGs; however, photonic bandgap waveguides are designed to only propagate radiation within the optical bandgap, similar to an optical bandpass filter. Also, these waveguides are currently engineered for applications using monochromatic radiation sources such as e.g. CO_2 lasers or quantum cascade lasers with the laser emission

wavelengths matched to the photonic bandgap provided by the waveguide for establishing efficient radiation delivery systems in laser surgical applications, or for sensitive and selective platforms applicable in gas sensing of complex matrices with low limits of detection.[3]

7.2 Limitations for QCLs Lasing at Long Wavelengths

While the studies presented in this thesis focus on both FT-IR and QCLS for trace gas sensing, one essential component is missing: a QCL capable of lasing at longer wavelengths as required for BTX chemical sensing at room-temperature operation.

Chapters 4 and 5 discussed how and why LO phonon scattering is essential to depopulating E2, by means of E1 via a phonon transition. Usually, this results in population inversion; however, at longer wavelengths the transition energy (meV) decreases with increasing wavelength (decreasing wavenumbers), and - as a result - the transition time (ps) is short not allowing for LO phonon scattering. In other words, for population inversion to occur, the LO phonon scattering rate from E2 – E1 must be much faster than the lifetime due to phonon scattering at the E3 – E2 transition. At longer wavelengths, these lifetimes become increasingly equal to each other. Additionally, another factor to date preventing QCLs from lasing in the fingerprint region, is that waveguide losses increases with increasing wavelength due to the effects of free carriers on the complex refractive index.[9]

With ongoing advances in bandstructure engineering, it is anticipated that QCL emission at long wavelengths will be attained at non-cryogenic temperatures, thus enabling their integration into chemical sensors. The studies presented in this thesis are intended to aid in the advancement of QCL based trace gas sensing upon the practical realization of these wavelengths; particularly within the fingerprint region of the IR spectrum where BTX exhibit strong and well-defined absorbance features.

References

[1]C. Young, S. Hartwig, A. Lambrecht, S.-S. Kim, and B. Mizaikoff, Optimizing Gas Sensors Based on Quantum Cascade Lasers and Photonic Bandgap Hollow Waveguides, IEEE Sensors, Atlanta, GA, 2007, pp. 1345-1348

[2]J.A. Harrington, A review of IR transmitting, hollow waveguides. Fiber and Integrated Optics 19 (2000) 211-227.

[3]B. Temelkuran, S.D. Hart, G. Benoit, J.D. Joannopoulos, and Y. Fink, Wavelength-scalable hollow optical fibers with large photonic bandgaps for CO2 laser transmission. Nature 420 (2002) 650-653.

[4]D.J. Haan, D.J. Gibson, C.D. Rabii, and J.A. Harrington, Coiled hollow waveguides for gas sensing. Proceedings of the SPIE (1998) 125.

[5]D.J. Haan, and J.A. Harrington, Hollow waveguides for gas sensing and near-IR applications. Specialty Fiber Optics for Medical Applications (1999).

[6]M. Miyagi, Bending losses in hollow and dielectric tube leaky waveguides. Applied Optics 20 (1981) 1221-1229.

[7]M. Miyagi, and S. Kawakami, Design theory of dielectric-coated circular metallic waveguides for infrared transmission. Journal of Lightwave Technology (1984) 116-126.

[8]M. Saito, Y. Matsuura, M. Kawamura, and M. Miyagi, Bending losses of incoherent light in circular hollow waveguides. Journal of the Optical Society of America A 7 (1990) 2063-2068.

[9]K.J. Franz, New Quantum Cascade Laser Architectures: II–VI Quantum Cascade Emitters, High k-Space Lasing, and Short Injectors. Department of Electrical Engineering, Princeton University, Princeton, NJ (2009) 89-92.

APPENDICES

Appendix A: Training set analyte concentration values. Standards were prepared and measured via a randomized run order (a random number generator was used).

Standard	Benzene (ppm)	Toluene (ppm)	Xylenes (ppm)	Run Order
1	5	16	32	54
2	5	48	44	9
3	5	28	25	78
4	5	37	15	73
5	5	47	29	57
6	5	21	19	36
7	6	53	29	69
8	6	43	42	106
9	6	22	41	95
10	6	24	45	3
11	6	30	60	85
12	6	23	37	64
13	6	42	41	18
14	6	38	41	75
15	6	46	42	51
16	6	55	34	24
17	6	27	31	30
18	7	29	51	1
19	7	34	35	87
20	7	42	31	63
21	7	54	26	79
22	7	30	43	13
23	7	15	55	21

24	7	50	18	92
25	7	19	60	103
26	7	34	25	71
27	7	25	57	45
28	7	39	42	55
29	8	51	41	20
30	8	20	41	68
31	8	48	36	28
32	8	23	34	102
33	8	42	24	8
34	8	34	22	39
35	8	23	45	108
36	8	39	35	34
37	8	25	24	72
38	8	47	34	42
39	8	29	17	11
40	9	53	25	62
41	9	24	51	31
42	9	27	39	41
43	9	31	50	49
44	9	20	45	33
45	9	20	50	100
46	9	22	47	89
47	9	45	16	88
48	9	29	30	27
49	9	24	35	2
50	9	48	26	37
51	10	33	40	109
52	10	38	50	80
53	10	32	48	104
54	10	39	27	93

55	10	27	38	105
56	10	22	21	19
57	10	22	46	84
58	10	59	20	60
59	10	36	47	66
60	10	18	46	59
61	11	15	49	99
62	11	27	48	16
63	11	43	10	6
64	11	21	43	94
65	11	48	20	74
66	11	40	31	15
67	11	35	26	32
68	11	46	29	43
69	11	50	34	98
70	11	41	31	47
71	11	41	46	61
72	12	36	51	58
73	12	27	47	4
74	12	18	57	83
75	12	23	32	81
76	12	23	39	90
77	12	34	20	110
78	12	29	45	67
79	12	48	23	56
80	12	36	49	82
81	12	30	24	77
82	12	36	37	52
83	13	35	34	91
84	13	35	45	14
85	13	16	37	86

86	13	34	45	23
87	13	17	29	72
88	13	31	35	50
89	13	56	18	76
90	13	30	30	65
91	13	28	48	35
92	13	17	43	96
93	13	33	37	12
94	14	29	32	40
95	14	36	36	26
96	14	43	20	10
97	14	20	48	34
98	14	24	27	48
99	14	18	24	7
100	14	40	46	44
101	14	48	38	69
102	14	15	15	38
103	14	25	48	25
104	14	17	20	53
105	15	24	16	29
106	15	46	30	22
107	15	26	39	46
108	15	32	18	5
109	15	45	40	70
110	15	37	45	18

Appendix B: Quantum cascade laser heterostructure design with layer thicknesses in Angstroms.

Layer Thickness (Angstroms)	Barrier (B)	Active region (A)
26		
17	B	
22		
18	B	
19		
19	B	
18		
21	B	
17		
21	B	
15		
27	B	
15		
38	B	
11		A
13	B	A
36		A
14	B	A
34		A
14	B	A
30		A
22	B	A

Appendix C: All possible optical transitions with calculated optical dipole matrix elements and non-radiative (LO phonon) scattering times.

theoretical bias (V)	LO phonon	dipole matrix element	transition	electric field (kV/cm)	energy difference (meV)	calculated theoretical emission (cm^{-1})
14.398	336	2.43	1713	87	275	2212.166918
14.398	680	1.34	1712	87	282.2	2270.08547
14.552	231	2.9	1915	88	277	2228.255405
14.552	727	1.21	1914	88	285.9	2299.84917
14.706	167	3.37	1915	89	279.1	2245.148316
14.706	736	1.11	1914	89	289.6	2329.612871
14.86	125	3.88	1814	90	281	2260.432378
14.86	702	1.03	1813	90	293.3	2359.376571
15.014	94	4.44	1814	91	282.9	2275.71644
15.014	632	0.979	1813	91	297	2389.140271
15.168	71.4	5.06	2117	92	284.6	2289.391654
15.168	540	0.941	2116	92	300.7	2418.903972
15.322	54.4	5.77	1814	93	286.2	2302.262443
15.322	5300	1.08	1816	93	265.7	2137.355455
15.322	441	0.911	1813	93	304.3	2447.863248
15.476	41.6	6.56	2016	94	287.3	2311.111111
15.476	3240	1.34	2018	94	269	2163.901458
15.63	32.5	7.37	2117	95	289.2	2326.395173
15.63	1950	1.68	2118	95	272.2	2189.643037
15.784	24.7	8.39	1915	96	290.5	2336.85269
15.784	1160	2.1	1916	96	275.4	2215.384615
15.938	19.5	9.37	1915	97	291.8	2347.310206
15.938	681	2.64	1916	97	278.3	2238.712921
16.092	15.7	10.3	2117	98	292.9	2356.158874
16.092	395	3.31	2118	98	281.2	2262.041227
16.246	13.2	11.1	2016	99	294	2365.007541
16.246	227	4.15	2017	99	283.8	2282.956259
16.4	11.5	11.7	1915	100	294.9	2372.24736
16.4	129	5.21	1916	100	286.3	2303.066868
16.554	10.6	11.9	1915	101	295.9	2380.291604
16.554	71.4	6.58	1916	101	288.7	2322.373052
16.708	10.4	11.6	1915	102	296.8	2387.531423
16.708	39.3	8.33	1916	102	290.7	2338.461538
16.862	11.4	10.6	2218	103	297.9	2396.38009
16.862	22.3	10.4	2219	103	292.5	2352.941176
17.016	14	12.5	2118	104	293.9	2364.203117
17.016	14.2	8.76	2117	104	299.2	2406.837607

17.17	14.2	10.3	1916	105	295	2373.051785
17.17	19.4	6.69	1915	105	300.8	2419.708396
17.324	8.52	15.2	2016	106	295.7	2378.682755
17.324	26.9	4.95	2015	106	302.5	2433.38361
17.478	7.6	15.8	2117	107	296.2	2382.704877
17.478	36	3.52	2115	107	304.4	2448.667672
17.6628	47.7	2.26	2217	108.2	306.6	2466.365008
17.6628	7.02	16.3	2219	108.2	296.7	2386.726998
17.786	6.73	16.5	2118	109	296.3	2383.509301
17.786	55.3	1.6	2116	109	308.2	2479.235797
17.94	6.49	16.7	2320	110	297.2	2390.74912
17.94	63.9	0.926	2318	110	310.1	2494.519859
18.094	6.33	16.9	2219	111	297.4	2392.357969
18.094	74	0.324	2217	111	312	2509.803922
18.248	6.21	17	2118	112	298	2397.184515
18.248	8.28	2.52	2115	112	344.9	2774.459527
18.248	939	1.17	2317	112	333	2678.733032
18.402	6.12	17	2522	113	297.7	2394.771242
18.402	895	1.46	2721	113	336	2702.865762
18.402	7.88	2.73	2518	113	345.7	2780.894922
18.556	6.05	17.1	2421	114	297.8	2395.575666
18.556	80.3	0.99	2420	114	317.5	2554.04726
18.556	7.57	2.91	2418	114	346.4	2786.525892
18.556	22.3	0.353	2417	114	364.8	2934.53997
18.71	24.7	7.8	2622	115	298.1	2397.988939
18.71	7.32	15.4	2522	115	297.8	2395.575666
18.71	94.8	2.27	2521	115	319.2	2567.722474
18.71	29.3	2.81	2619	115	347.3	2793.765711
18.71	8.85	2.13	2519	115	347	2791.352438
18.71	27	1.85	2518	115	366.5	2948.215184
18.864	5.97	17.2	2420	116	297.9	2396.38009
18.864	78.3	1.58	2418	116	321.1	2583.006536
18.864	7.12	3.35	2416	116	347.7	2796.983409

VITA

1. S.S. Kim, C. Young, B. Vidakovic, S. Gabram-Mendola, C. Bayer, B. Mizaikoff. "Potential and Challenges for Mid-Infrared Sensors in Breath Diagnostics". IEEE Sensors Journal (2009), In Press.

2. C. Young, R. Cendejas, S. S. Howard, B. Mizaikoff, C. F. Gmachl. "Spectral Emission Tuning of InGaAs/AlInAs Buried-Heterostructure Quantum Cascade Lasers by Modifying Cavity Length". Applied Physics Letters (2009), 94, 091109.

3. C. Young, Y. Luzinova, S.-S. Kim, M. Weida, D. Arnone, E. Takeuchi, T. Day, B. Mizaikoff. "External Cavity Widely Tunable Quantum Cascade Laser Based Hollow Waveguide Gas Sensors for Multianalyte Detection". Sensors and Actuators, B: Chemical, (2009), 140(1), 24-28.

4. S.-S. Kim, N. Menegazzo, C. Young, J. Chan, C. Carter, B. Mizaikoff. "Mid-Infrared Trace Gas Analysis with Single-Pass FT-IR Hollow Waveguide Gas Sensors". Applied Spectroscopy (2008), 63(3), 331-337.

5. S.-S. Kim, C. Young, B. Mizaikoff. "Minaturized Mid-Infrared Sensor Technologies". Analytical and Bioanalytical Chemistry (2008), 390(1), 231-237.

6. C. Young, S.-S. Kim, B. Mizaikoff. “Quantum Cascade Laser Based Gas and Liquid Chemical Sensors”, in Lasers in Chemistry, Maximillian Lackner, ed. Weinheim, Germany: Wiley VCH GmbH, 2008.

7. G. Dobbs, B. Balamurali, C. Young, C. Kranz, D. Hess, B., Mizaikoff. “Mid-Infrared Chemical Sensors Utilizing Plasma-Deposited Fluorocarbon Membranes”. Analytical Chemistry (2007), 79(24), 9566-957.

8. S.-S. Kim, C. Young, J. Chan, C. Carter, B. Mizaikoff. “Hollow Waveguide Gas Sensor for Mid-Infrared Trace Gas Analysis”. Proceedings of the IEEE Sensors (2007).

9. C. Young, S. Hartwig, A. Lambrecht, S.-S. Kim, B. Mizaikoff. “Optimizing Gas Sensors Based on Quantum Cascade Lasers and Photonic Bandgap Hollow Waveguides”. Proceedings of the IEEE Sensors (2007).